

Magnetism of Nano- to Micrometer-Sized Anisotropic Materials

Inauguraldissertation

zur Erlangung der Würde eines Doktors der Philosophie

vorgelegt der
Philosophisch-Naturwissenschaftlichen Fakultät
der Universität Basel

von

Simon Philipp

Basel, 2022

Genehmigt von der Philosophisch-Naturwissenschaftlichen Fakultät auf Antrag von

Prof. Dr. Martino Poggio
Erstbetreuer

Prof. Dr. Ernst Meyer
Zweitbetreuer

Prof. Dr. Mark Freeman
externer Experte

Basel, den 26.04.2022

Prof. Dr. Marcel Mayor
Dekan

Contents

1	Introduction	1
2	Theoretical Background	3
2.1	Dynamic Cantilever Magnetometry	3
2.1.1	Introduction	3
2.1.2	Setup	4
2.1.3	Measurement Principle	5
2.2	Micromagnetic methods - Basic concepts	6
2.2.1	Introduction	6
2.2.2	DCM in a Stoner-Wohlfarth framework	8
2.2.3	DCM in numerical micromagnetics	14
2.3	Micromagnetic methods - Applications	16
2.3.1	Thermal activation: Superparamagnetic particles	16
2.3.2	DCM and susceptibility	19
2.4	Detecting Phase transitions	23
2.4.1	Introduction	23
2.4.2	DCM properties in a thermodynamic framework	24
3	Magnetic Hysteresis of Individual Janus Particles with Hemispherical Exchange Biased Caps	29
3.1	Introduction	29
3.2	Exchange bias as unidirectional anisotropy	30
3.3	Samples and Cantilevers	33
3.4	Results and Discussion	34
3.4.1	Measurements	34
3.4.2	Micromagnetic simulations	35
3.4.3	Ferromagnetic Janus particles	37
3.4.4	Exchange biased Janus particles	39
3.5	Summary and Conclusion	41
4	Magnetic Anisotropy of Individual Maghemite Mesocrystals	43
4.1	Introduction	43
4.2	Samples and Cantilevers	44
4.3	Results and Discussion	45
4.3.1	Measurements	45
4.3.2	High-field Limit	45
4.3.3	Full Field Dependence	49
4.3.4	Behavior at low temperature	51
4.4	Summary and Conclusion	54

5	Stability of Néel-Type Skyrmion Lattice Against Oblique Magnetic Fields in GaV₄Se₈	55
5.1	Introduction	55
5.2	Non-collinear magnetic structures	56
5.3	Sample and Cantilever	57
5.4	Results and Discussion	58
	5.4.1 Magnetic phase diagram: In-domain transitions	58
	5.4.2 Magnetic phase diagram: Domain Wall states	60
5.5	Summary and Conclusion	63
6	Conclusion and Outlook	65
7	Appendix	69
7.1	Mumax ³ code used for simulations in chapter 2.3.2	69
8	Acknowledgements	73
	References	77
	References	89

1 Introduction

Magnetic materials have a large variety of everyday uses. From audio speakers to magnetic memory or logic devices, many branches of modern technology at least partially rely on magnets. In biology and medicine, magnetic nanoparticles serve for example as contrast agents in biological and MRI imaging. In hyperthermia cancer treatment, nanoparticles are located at tumor cells and actuated using an oscillating magnetic field, causing them to rotate and overheat the malignant tissue [1]. Micron and sub-micron sized magnetic particles are further discussed in modern scientific settings as a multi-functional component in lab-on-chip or micro-total analysis systems [2, 3]. Magnetic Janus-Particles, consisting of a hemispherical cap of magnetic material on a non-magnetic spherical template, allow not only a controlled transversal motion, but also a controlled rotation by rotating external magnetic fields [4, 5]. The transversal and rotary motion of these particles can be controlled via external magnetic fields, which exert magnetic forces and torques [6]. This ability has led to applications in microfluidics, e.g. as stirring devices [7], as microprobes for viscosity changes [8], or as cargo transporters in lab-on-chip devices [9–11]. Magnetic JPs have also been proposed as an in vivo drug delivery system [12]. Recent interest has been building for new technical and biomedical applications [13, 14] of maghemite ($\gamma\text{-Fe}_2\text{O}_3$) nanoparticles, which also have a long history in magnetic recording applications [15].

A different approach is to facilitate magnetic states of nano- and micro-structured bulk materials. In magnetic recording devices, distinct regions of a magnetic recording medium are magnetized, forming structures of magnetic domains that can be read out and interpreted [16]. The increasing demand of energy efficient manipulation of magnetic states has motivated the design of a magnetic racetrack-memory [17], a device that allows for high-density data storage by arranging stripes of magnetic material vertically to the read/write head. Data is stored by use of magnetic domain walls that can be moved using electrical currents. The discovery of the nanometer-scale magnetization configurations known as magnetic skyrmions [18], has sparked new interest in the research of non-collinear magnetic structures. Both skyrmion lattices (SkLs) [19, 20] and isolated skyrmions [21] have now been observed in either bulk or nanostructured noncentrosymmetric crystals. Their topologically protected spin-texture, which is stable even at room temperature [22], their nanometer-scale size, and their easy manipulation via electric currents and fields [23–27] make skyrmions a promising platform for information storage and processing applications [28]. A magnetic racetrack memory that uses skyrmions instead of domain walls have been proposed as a ultra-dense, low-cost and low-power storage technology [29].

Magnetometry of individual nano- to micron-sized magnetic particles using conventional, commercially available measurement techniques is complicated due to the inherently small generated signals and hence the necessity to investigate large ensembles of particles. This typically leads to random orientation of, and considerable interactions between the particles. Consequently, information on magnetic states or anisotropies is averaged out. Dynamic Can-

tilt Magnetometry (DCM) has been established as a sensitive method to investigate very small, individual magnets without the need for electrical contacts or large sample volumes. DCM has been used to investigate effects such as persistent currents in normal metal rings [30], vortex entries in magnetic tubes [31], quantum oscillations in Weyl semimetals [32] or magnetic phase diagrams in skyrmion hosting nanowires [33]. Another advantage of DCM lies in the ability to retrieve information such as direction, type and strength of the magnetic anisotropy of individual magnets.

This thesis offers a contribution to the research on the magnetism of nano- to micrometer-sized magnetic particles using Dynamic Cantilever Magnetometry. We analyze the data using analytical models and micromagnetic simulations. We demonstrate the manipulation of the remanent state of spherical Janus Particles with a magnetic cap, using exchange bias as a means to provide an artificial, unidirectional anisotropy. We further analyze the anisotropy and blocking temperature of superparamagnetic maghemite mesocrystals. Both types of magnetic systems have previously not been investigated on the individual level. We also highlight the contribution to the investigation of phase transitions and domain wall magnetism in the multiferroic polar magnet GaV_4Se_8 .

The document is structured as follows: Chapter 2 describes the theoretical background necessary to understand the measurements and data analysis. It introduces the setup and the basic concept of DCM. Afterwards, it guides the reader through the concepts of micromagnetics and establishes analytical as well as numerical methods in order to reconstruct the signals obtained from the DCM measurements for different magnetic systems. Subsequently, DCM is analyzed in a thermodynamic framework, correlating features in DCM measurements with the behavior of thermodynamic properties included in the Gibb's free energy of the magnetic particle.

Chapter 3 shows measurements of magnetic Janus Particles. Exchange bias is introduced as a unidirectional anisotropy in order to manipulate the magnetic states at remanence. The magnetic anisotropy of a spherical cap is analyzed using the Stoner-Wohlfarth model, as well as micromagnetic simulations to match the data and gain insights into the magnetic state of the cap.

In Chapter 4, we present the results of the anisotropic behavior of maghemite mesocrystals. Mesocrystals are composed of large number of perfectly arranged and equally-sized magnetic nanoparticles, which allows for the measurement of the cubic crystal symmetry of the maghemite nanoparticles while simultaneously distinguish the signal from the contribution of the overall shape of the mesocrystal.

Chapter 5 summarizes the contribution of DCM measurements to the description of domain wall magnetism in GaV_4Se_8 . Being part of a collaborative effort, we add to the description of the material by mapping out the magnetic phase diagram, demonstrating the stability of a Néel-type skyrmion lattice against oblique magnetic fields.

Finally, Chapter 6 summarizes the findings presented in the thesis and provides an outlook to further projects and the perspective of torque magnetometry in the recent research trends on magnetism.

2 Theoretical Background

2.1 Dynamic Cantilever Magnetometry

2.1.1 Introduction

The first famous experimental observation of the magnetic torque was reported by Albert Einstein and Wander Johannes de Haas in 1915 [34], after carrying out an experiment suggested by O.W. Richardson in 1908 [35]. Richardson calculated the torque that electrons experience due to their orbital motion in an external magnetic field and predicted that the collective effect of all electrons in a macroscopic suspended sample in a homogeneous magnetic field would easily generate a measurable torsion. In 1918, Karl Beck provided a thorough investigation of the torque for various orientations of the crystallographic directions of iron disks [36]. The samples were mounted on a sample holder in the air gap between the pole shoes of a bore magnet, suspended vertically on a phosphor bronze wire. The wire has a pointer attached to it at the top end and the torsion was measured by the relative displacement to a reference pointer. In general, this design was used in slightly modified versions until D.S. Miller introduced an electrical readout method in 1950 [37] using a resistance strain gauge to convert the torque to a small direct-current voltage. This voltage was applied to the measuring circuit of a "strip-chart" voltage recorder. Synchronizing the rotational movement of the disk sample in an applied field and the movement of the paper in the recorder using two motors, the output of the voltage recorder becomes a plot of torque versus the angle of rotation.

After this, the read out and sensing methods have been improved and adapted for both particularly large and small magnetic fields and for very high and also cryogenic temperatures. The basic design, however, remained more or less the same for several decades. Over the years, torque magnetometry has been established as a powerful method to investigate effects in solid state physics such as two dimensional electron systems, quantum oscillations or superconductivity. [38–40]. The technological possibility to investigate even smaller magnetic or superconducting samples at the submicron scale lead to the increasing demand for high-sensitivity magnetometers in the 1990s. Even though the SQUID magnetometers at the time already provided a very high sensitivity, their read-out was slow compared to torque magnetometers. The most sensitive torque magnetometers at the time were using a capacitive read-out method where a metallic beam was placed between two capacitor plates, or using the torsion of a tungsten support wire. In 1996, Roessl *et al.* proposed the use of an active piezo resistive micro cantilever as a new type of torque sensor. [41].

This sensitive method has evolved into what is now known as dynamic cantilever magnetometry (DCM) and allows to measure torque originating from such small magnetic moments, that the size of the investigated samples can have dimensions in the range of a few tens to a few hundreds of nanometers. In DCM, the sample under investigation is fixed at the apex of a cantilever and driven at its resonant frequency in a homogeneous, external magnetic field \mathbf{H} . The exerted torque $\boldsymbol{\tau} = \boldsymbol{\mu}(\mathbf{H}) \times \mathbf{H}$ causes a static bending of the cantilever as well as a shift in the resonance frequency.

Being linked to its free energy, measuring the frequency shift of the cantilever as a function of temperature as well as magnitude and orientation of the external magnetic field allows for retrieval of information about the magnetic sample, most notably type and orientation of the effective magnetic anisotropy, switching processes and phase transitions. The basic principle of DCM has been described in quite some detail for example in [42–44]. In the following chapter, we provide the theoretical background to understand the measurements and data analysis throughout the thesis. We introduce the Stoner-Wohlfarth model as well as micromagnetic models as a means to calculate the frequency shift for different types of anisotropic magnetic systems and give a model for a thermodynamic approach to measure phase transitions.

2.1.2 Setup

A schematic of the setup is depicted in Fig.(2.1). The cantilever with the magnetic sample attached is mounted in a vibration-isolated closed-cycle helium cryostat (Montana Instruments). The pressure in the sample chamber is less than 10^{-6} mbar and the temperature can be stabilized between 4 and 300 K. As indicated in Fig.(2.1), the long axis of the cantilever is aligned with the x -axis of its corresponding coordinate system and hence oscillates in the xz -plane around its y -axis. This configuration will be used throughout the thesis. Using an external rotatable superconducting room temperature bore magnet, magnetic fields with amplitudes of up to 4.5 T can be applied along any direction spanning 225° in the plane of the cantilever. This direction is specified by θ_h , which is the angle between \mathbf{H} and \mathbf{z} . The cantilever’s flexural motion is read out using an optical fiber interferometer employing 100 nW of laser light at 1550 nm [45]. A piezoelectric actuator mechanically drives the cantilever at the resonance

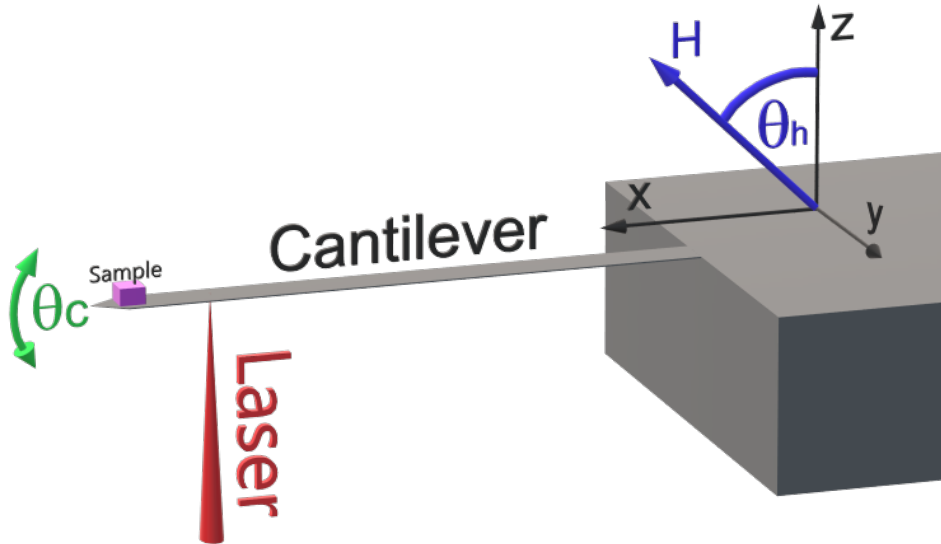


Figure 2.1 | Schematic of the Setup. The long axis of the cantilever is aligned with the x -axis of the coordinate system and oscillates around the y -axis. The magnet-on-cantilever system is mounted inside a closed-cycle helium cryostat. The flexural motion of the cantilever is read-out via a laser interferometer. An external magnetic field with an amplitude of up to 4.5 T is applied using a rotatable, superconducting room temperature bore magnet. The field \mathbf{H} can be rotated by an angle of 225° in the xz plane.

frequency f_0 of its first flexural mode with a constant oscillation amplitude of a few tens of nanometers using a feedback loop implemented by a field-programmable gate array. This process enables the fast and accurate extraction of f_0 from the cantilever deflection signal. The choice of cantilevers depends on the sample of interest. In general, the sensitivity and spring constant of the cantilever need to be approximately compatible with the anticipated (dynamic) torque. Also, the additional mass of the sample should not push the resonance frequency of the cantilever too much towards lower frequencies, e.g. below 1 kHz, since the sensor becomes susceptible to low-frequency mechanical noise in this regime.

2.1.3 Measurement Principle

The combined magnet-on-cantilever system can be treated as a damped harmonic oscillator. In order to cause a deflection of the cantilever, the torque has to be exerted along \mathbf{y} and we refer to τ_y as τ . The equation of motion of the system is now given as

$$m_e \ddot{x} + \Gamma \dot{x} = \frac{\tau}{l_e} \quad (2.1)$$

where m_e and l_e are the effective mass and the effective length, respectively, Γ is the mechanical dissipation. We use the term "effective" here, since the model assumes the cantilever to be massless, assigning all the mass to the attached particle. We operate the system in the small angle regime where the oscillation angle of the cantilever $\theta_c \ll 1$ and we can substitute $x \approx l_e \theta_c$ in Eq. (2.1). The total energy of the system can be expressed in two terms, the mechanical energy of the cantilever and the magnetic energy E_m of the attached magnet:

$$E_{tot} = \frac{k_0 l_e^2}{2} \theta_c^2 + E_m \quad (2.2)$$

where k_0 is the unaltered spring constant of the cantilever. E_m depends on the exact shape, material and magnetic anisotropy of the sample and has to be considered individually. The deflection of the cantilever is proportional to the exerted torque and can be expressed as $\tau = -\left(\frac{\partial E_{tot}}{\partial \theta_c}\right)$, which we can expand to the first order around $\theta_c = 0$. Doing this and substituting the resulting expression for τ in Eq. (2.1) yields

$$m_e \ddot{\theta}_c + \Gamma \dot{\theta}_c + \left[k_0 + \frac{1}{l_e^2} \left(\frac{\partial^2 E_m}{\partial \theta_c^2} \Big|_{\theta_c=0} \right) \right] \theta_c = -\frac{1}{l_e^2} \left(\frac{\partial E_m}{\partial \theta_c} \Big|_{\theta_c=0} \right) \quad (2.3)$$

The solutions for this are well known from the theory for the harmonic oscillator. We apply $\omega_0 = \sqrt{\frac{k_0}{m_e}}$ to obtain the frequency shift $\Delta\omega = \omega - \omega_0$ and after substituting $\omega = 2\pi f$, the expression for the frequency shift reads as follows:

$$\Delta f = \frac{f_0}{2k_0 l_e^2} \left(\frac{\partial^2 E_m}{\partial \theta_c^2} \Big|_{\theta_c=0} \right) \quad (2.4)$$

From Eqs. (2.3) and (2.4), it can be seen that the frequency shift in a DCM measurement is generated by a modification of the spring constant k_0 , proportional to the curvature of the magnetic energy E_m . There are two main experiments that we carry out in DCM. In the first one we fix the external field at a high enough value to reach the high-field limit, where the frequency shift is at an asymptotic value Δf_{hf} , which is then measured as a function of

θ_h . This probes the type and direction of the effective anisotropy of the magnet. We refer to this as angle dependent measurements. For the other one we choose a fixed value for θ_h and measure Δf as a function of the magnitude of the applied field, which is equivalent to a typical hysteresis measurement. Both experiments shall be described in more detail below. Besides the frequency shift, there are two other quantities that can be measured, see Table (2.1)

Δf	$\frac{f_0}{2k_0 l_e^2} \left(\frac{\partial^2 E_m}{\partial \theta_c^2} \Big _{\theta_c=0} \right)$	Frequency shift
Γ	Voltage applied to Piezo	Dissipation
τ	$-\frac{1}{l_e} \left(\frac{\partial E_m}{\partial \theta_c} \Big _{\theta_c=0} \right)$	Torque, static bending

Table 2.1 | Measurable quantities in a DCM measurement

The first one is the dissipation Γ , which describes the system's rate of energy loss: $dE/dt = -\Gamma l_e^2 \dot{\theta}_c^2$ [46]. In order to maintain a constant oscillation amplitude, the cantilever must be driven with a force $F = \Gamma l_e \dot{\theta}_c$, such that any losses due to dissipation are compensated. The voltage amplitude used to drive the piezoelectric actuator is therefore proportional to $\Gamma = \Gamma_0 + \Gamma_m$ where Γ_0 is the cantilever's intrinsic mechanical dissipation at $H = 0$ and Γ_m represents magnetic losses. Given that Γ_m reflects the sample's magnetic relaxation, Γ should undergo abrupt changes at magnetic phase transitions. This can be compared to the imaginary part of a traditional magnetic susceptibility measurement. The signature of a magnetic phase transition in the Δf signal is often a dip or a jump, which can look the same as the signature of a ferromagnetic switching or similar processes. Therefore, in many situations, it is necessary to compare and correlate features in the frequency shift and the dissipation signal of a measurement in order to obtain a correct phase diagram.

The other one is a static torque τ which causes a static bending of the cantilever. We have access to this quantity by monitoring the displacement of the cantilever from its equilibrium position at zero field. This set of quantities contains all the information we can directly get from the magnetic sample using this type of measurement. Note, however, that since magnetization dynamics typically take place in the GHz range, while cantilevers usually operate in the kHz-MHz range, it is not possible to obtain information about the time-resolved magnetic state present in the sample, but rather about the quasi-static magnetic state, which is a temporal average of the former over the time period of the cantilever oscillation.

2.2 Micromagnetic methods - Basic concepts

2.2.1 Introduction

We use DCM to investigate samples with dimensions on the order of a few hundred nanometers to a few tens of microns. On this particular length scale, the lateral dimensions are much bigger than the lattice constant a of the material but small enough for quantum mechanical effects, essential for the description of a ferromagnet, to be still comparably strong. [47]. As a consequence, neither a fully classical nor a purely quantum mechanical theory such as Maxwell's theory or density functional theory, respectively, are suitable to describe such magnets [48]. This gap in theoretical descriptions emerged after the discovery of Weiss domains in 1907 [49] and subsequent experiments on domain patterns and their respective domain walls by

Barkhausen 1919 [50], Bitter [51], as well as Sixtus and Tonks [52], all in 1931. The theory that was developed to close that gap during the 1930s and 1940s is now known as micromagnetics and was established by Brown 1940 and 1941 [53, 54].

The main assumption in the micromagnetic model is, that the interactions in the magnet are strong enough to keep the magnetization parallel over a characteristic length scale $\lambda \gg a$, such that [47]

$$\mathbf{S}_i \approx \mathbf{S}_j \quad \text{for} \quad |\mathbf{x}_i - \mathbf{x}_j| < \lambda \gg a \quad (2.5)$$

where $\mathbf{S}_{i,j}$ are individual spins at positions $\mathbf{x}_{i,j}$. Considering that λ is smaller or on the order of the lateral dimensions of the sample (e.g. true for nano particles below the single domain limit), it is reasonable to assume, that the density of discrete spins is homogeneous for a given material. Hence, the sum over individual spins can be well approximated by an integral over a continuous magnetization $\mathbf{M}(\mathbf{x})$, which, in turn, is treated in terms of a unit-vector field $\mathbf{m}(\mathbf{x})$

$$\mathbf{M}(\mathbf{x}) = M_s \mathbf{m}(\mathbf{x}) \quad \text{with} \quad |\mathbf{m}(\mathbf{x})| = 1 \quad (2.6)$$

where M_s is the saturation magnetization. [47].

Aiming for a full description of the magnet, terms that contribute to the magnet's energy E_m will be either of classical or quantum mechanical nature. Using the above approach, all those terms can be described by incorporating (differential) vector operations on $\mathbf{m}(\mathbf{x})$ and a magnetic field \mathbf{H} . There is a multitude of relevant terms that potentially add to E_m . Depending on the properties of the sample that needs to be described, some terms need to be included, while others can be left out. A summary of the magnetic terms can be found for example in [42–44] or in common textbooks on magnetism.

In order to calculate static micromagnetic properties, as for example for the determination of the hysteresis loop of a given magnetic system, it is necessary to find a stable magnetization configuration for the applied magnetic field. This can be obtained by finding a minimum of the total free energy while fulfilling the condition given by eq. (2.6), known as the micromagnetic unit-sphere constraint [47]. Using variational calculus, the expressions and boundary conditions that minimize the magnetic energy can be found in [47] for typical contributing terms of E_m .

An analytical solution for the problem was introduced by Stoner and Wohlfarth (SW) in 1947. In order to solve the equations, their model makes the simplified assumption that the magnetization of the sample behaves as one macroscopic magnetic moment. The SW model can be applied with reasonable accuracy in two different regimes. The first one is what we call the low-field limit. In this case, only a low magnetic field is applied and the magnetic energy is dominated by the involved anisotropies along which the magnetic moments will align. The second one is the opposite scenario, which we call the high-field limit. The magnetic energy is dominated by a high applied magnetic field, and the magnetic moments are aligned parallel to the field direction. In the low-field limit, the SW model makes sense for example in the case of nano particles below the mono-domain boundary [55]. In this regime, the formation of a domain wall is energetically not favorable, and the macro spin model can be applied. For magnets with sizes above the mono-domain boundary, the model may be considered in the high-field limit.

The SW model reaches its limit in cases where the measured signal shows features that arise due to individual switching events in the sample, since the spatial distribution of the magnetization is not considered. In this case, the equations can not be solved analytically and require numerical methods [56]. Numerical solutions use a discretization of the sample

geometry in order to find solutions of $\mathbf{m}(\mathbf{x})$. Unlike the SW model, this method considers the spatial distribution of magnetic moments in the sample. The numerical frameworks used in this thesis are MuMax³ and nmag.

Given the knowledge of the cantilever properties, the frequency shift can be calculated in both a SW and numerical framework using eq.(2.4), which allows for a direct comparison with a measured quantity. The following sections will introduce analytical as well as numerical methods used for the analysis of the data. The relevant magnetic energy terms will be introduced for each example individually.

2.2.2 DCM in a Stoner-Wohlfarth framework

In their 1947 theory [57], Stoner and Wohlfarth describe one of the rare situations where the micromagnetic equations can be solved analytically. This is the case for small magnets where the exchange interaction keeps the spins parallel. The magnetization then rotates in unison and can be treated like one big macro-spin, which avoids the calculation of the precise $\mathbf{M}(\mathbf{x})$ dependence. It can be shown that the magnetization of a mono-domain particle in a homogeneous magnetic field behaves in the same way, as the magnetization of a suitably chosen ellipsoid [58]. In this chapter we introduce the Stoner-Wohlfarth (SW) approximation for different situations, starting with a purely ferromagnetic system described by a prolate ellipsoid. We then discuss the difference of a prolate and oblate ellipsoid, which has the same physical effect as having a positive or negative uniaxial anisotropy constant. Afterwards, we extend the model by introducing a thermally activated SW model, which approximates a super-paramagnetic particle. For all these situations, we calculate Δf from the magnetic energy.

2.2.2.1 Ferromagnetic particles with easy axis and easy plane anisotropy

We start with the description of a simple case of a ferromagnetic ellipsoid of revolution with a uniaxial anisotropy. For this, we use the following magnetic energy terms:

$$E_m = E_Z + E_u \quad (2.7)$$

where E_Z is the Zeemann energy and E_u a uniaxial anisotropy energy of the magnet.

The Zeemann term describes the potential energy of the magnetization in the external field and is given as

$$E_Z = -\mu_0 \int_V \mathbf{M} \cdot \mathbf{H} dV = -\mu_0 V \mathbf{M} \cdot \mathbf{H} \quad (2.8)$$

The anisotropy term describes a preferential direction of the magnetization in the sample. Uniaxial anisotropy can in some materials occur in form of a magnetocrystalline anisotropy [59] but can also appear due to the geometry of the sample. Magnetocrystalline anisotropy has its origin in the spin-orbit interaction, while geometry related anisotropy stems from dipolar interaction between the magnetic moments [60]. The resulting mathematical terms, however, have the same form. The term for the uniaxial anisotropy can be derived by analyzing the total magnetic field and energy inside and outside the ellipsoid. The derivation (see Ref.[60]) results in the following energy term:

$$E_U = \frac{\mu_0}{2} V (D_x M_x^2 + D_y M_y^2 + D_z M_z^2) \quad (2.9)$$

Where the D_i are the components of the demagnetization tensor D [61]. The D_i are interdependent since $\text{Tr}(D) = 1$ and their values depend on the ratios a/b and b/c of the ellipsoid's axes a , b and c . Note that the calculation of the parameters can be quite complicated and exact values can only be determined for a few special geometries [62, 63].

Here, we want to focus on the two extreme cases of a very long and thin, and one flat and wide geometry. The first one is the limit of an ideal easy axis anisotropy, the second one of an easy plane anisotropy. In general, if two axes of the ellipsoid are equal, their corresponding demagnetization factors are equal as well. We will use this in order to simplify eq.(2.9) by focusing on ellipsoids of revolution. For the first case, we assume $a = b \ll c$ and hence $D_x = D_y \gg D_z$. In an ideal case, $D_x = D_y = 0.5$ and $D_z = 0$. We introduce an effective demagnetization factor $D_u = D_z - D_x$ and consider only uniaxial shape anisotropy with an easy axis along the long axis of the ellipsoid. We further describe the direction of the uniaxial anisotropy by a vector \mathbf{n} in spherical coordinates with a set of angles (θ_n, φ_n) :

$$\mathbf{n}(\theta_n, \varphi_n) = \begin{pmatrix} \sin\theta_n \cos\varphi_n \\ \sin\theta_n \sin\varphi_n \\ \cos\theta_n \end{pmatrix} \quad (2.10)$$

In addition, we define the vectors of the external field and the magnetization in terms of spherical coordinates with angles (θ_h, φ_h) for the field and (θ_m, φ_m) for the magnetization in the coordinate system given in Fig. (2.1) in the same fashion.

If a magnetic field is applied, the magnetization will orient itself at some angle from the easy axis depending on the relative orientation and strength of the anisotropy and the magnetic field. This can be described by the scalar product between the magnetization and the uniaxial anisotropy vector and the magnetic energy can be rewritten as

$$E_m = -\mu_0 V M_s H_0 \mathbf{m} \cdot \mathbf{h} - K_{u1} V (\mathbf{m} \cdot \mathbf{n})^2 \quad (2.11)$$

with $K_{u1} = -\frac{\mu_0}{2} D_u M_s^2$ taking the role of an effective, shape related anisotropy constant. The elegance of this description becomes evident, when we consider the opposite case of an oblate ellipsoid with an easy plane anisotropy. By retaining the direction of \mathbf{n} as the orientation of the anisotropy, the description stays perfectly valid with only K_{u1} becoming negative and doubling in magnitude, since $D_x = D_y = 0$ and $D_z = 1$ for an infinitely flat ellipsoid with $a = b \gg c$. \mathbf{n} takes the role of a magnetic hard axis now, while the magnetization has no preferred direction in the \mathbf{xy} -plane. This is the case e.g. for a ferromagnetic disc, the physics of which has been studied extensively [64–71].

Now that the magnetic energy terms are established, we introduce a DCM model for this type of magnetic system. In order to study the differences of the two cases, we consider the high and low-field limit separately. For the high-field limit, the Zeemann term becomes dominant and $E_Z \gg E_u$. Therefore, $\mathbf{m}(\theta_m, \varphi_m) \parallel \mathbf{h}(\theta_h, \varphi_h)$ for all values of θ_h . In the experiment, the direction of the external field is restricted to the \mathbf{xz} -plane, of the coordinate system, i.e. perpendicular to the cantilevers rotation axis, as given in Fig.(2.1) and we set $\varphi_h = 0$ at all times. Applying this limit yields

$$\mathbf{m}(\theta_h) \equiv \mathbf{h}(\theta_h) = \begin{pmatrix} \sin\theta_h \\ 0 \\ \cos\theta_h \end{pmatrix} \quad (2.12)$$

The Zeemann term in eq.(2.11) becomes constant with $E_Z = -\mu_0 V M_s H_0$ since the scalar product $\mathbf{m} \cdot \mathbf{h} = 1$ and the cantilever oscillation only probes the second term in eq.(2.11), which then translates a change in energy due to the rotation of the anisotropy axis \mathbf{n} .

To account for the oscillation of the cantilever in the magnetic model, a rotation matrix is applied to \mathbf{n} , which is rotated around the \mathbf{y} -axis by an angle θ_c . The frequency shift is then determined using eq.(2.4).

We mentioned before that, in the high-field limit, the frequency shift is at an asymptotic high field value Δf_{hf} which is only dependent on the cantilever constants and the orientation of the anisotropy vector with respect to the external field vector and thus becomes a measure for the anisotropy in the system. Note that, if other anisotropies are present, Δf_{hf} probes the superposition of all involved anisotropies. Neglecting E_Z , the contribution from the uniaxial anisotropy to the high-field frequency shift for an arbitrary orientation of \mathbf{n} is given as follows:

$$\Delta f_{hf} = \frac{K_{u1} V f_0}{4k_0 l_e^2} \left[\cos(2\theta_h) \left(1 + 3 \cos(2\theta_n) - 2 \cos(2\varphi_n) \sin^2(\theta_n) \right) + 4 \cos(\varphi_n) \sin(2\theta_h) \sin(2\theta_n) \right] \quad (2.13)$$

In Fig.(2.2) we plot Δf_{hf} as a function of θ_h with \mathbf{n} aligned with the \mathbf{x} -axis, e.g. $(\theta_n, \varphi_n) = (\pi/2, 0)$ for both the easy axis and the easy plane situation. Since they only provide a scaling of the absolute value, we set all cantilever constants, the saturation magnetization, μ_0 and the volume V equal to one.

Assuming an ideal case for the easy axis and easy plane anisotropy, we set $D_u^{ea} = -0.5$ ($K_{u1}^{ea} = 0.25$) for the easy axis and $D_u^{ep} = 1$ ($K_{u1}^{ep} = -0.5$) for the easy plane type.

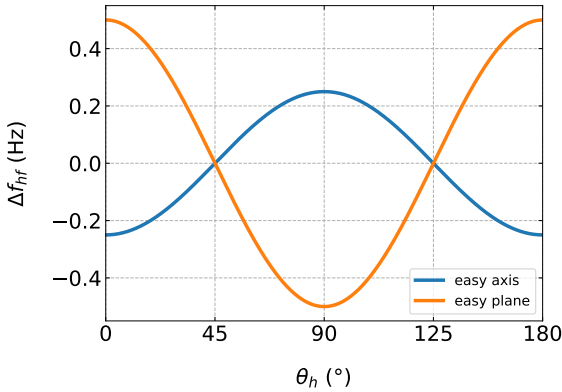


Figure 2.2 | High field frequency shift as calculated from a SW model for a prolate (easy axis, blue curve) and an oblate (easy plane, orange curve) ellipsoid. Minima and maxima correspond to field orientations perpendicular and parallel to the respective hard and easy directions.

For the situation corresponding to the curves in Fig.(2.2), the magnetic field is parallel to the \mathbf{z} -axis for $\theta_h = 0^\circ$, e.g. perpendicular to \mathbf{n} . Consequently, the field is parallel to \mathbf{n} for $\theta_h = 90^\circ$.

Looking at the easy axis curve (blue) first, it exhibits a minimum for $\theta_h = 0^\circ$ and a maximum for $\theta_h = 90^\circ$, where the field is perpendicular and parallel to the magnetic easy and hard direction, respectively. In these orientations, the frequency shift reaches the most positive and most negative asymptotic value. The same holds true for the easy plane curve (orange). In this case, however, the minima and maxima are exchanged, even though the direction of \mathbf{n} is the same. Also the amplitude of the curve is doubled. Both effects are directly related to the different sign and value of the anisotropy constants.

This behavior can be observed for any kind of anisotropy. If the field is parallel (perpendicular) to the magnetic easy direction, a positive (negative) frequency shift can be observed. This, in turn, allows for determination of the anisotropy direction, and in some cases also the type of anisotropy, using angle dependent measurements in the high-field limit.

The same analysis can be done for an easy axis anisotropy in the low-field limit. In this case $E_Z \ll E_u$ and the magnetization is either fixed to be parallel or anti-parallel to the anisotropy vector \mathbf{n} which means that the cantilever oscillation now only probes the first term in eq.(2.11), which is now a change in energy due to the rotation of the magnetization in the applied field. The low-field frequency shift Δf_{lf} can be calculated equivalently to Δf_{hf} and results in

$$\Delta f_{lf} = \frac{f_0 V H_0 \mu_0 M_s}{2k_0 l_e^2} (\cos(\theta_h) \cos(\theta_n) + \cos(\varphi_n) \sin(\theta_h) \sin(\theta_n)) \quad (2.14)$$

The term in parenthesis is the projection of the anisotropy vector on the magnetic field vector. Therefore, either M_x or M_z can be probed by aligning the magnetic field either with the \mathbf{x} or \mathbf{z} axis, since one of the terms goes to zero.

The situation in the low-field limit is less clear for the easy plane anisotropy. The problem can be understood by drawing an intuitive picture as follows: We assume the case of a real sample with easy plane anisotropy, as for example a perfectly symmetrical magnetic disk. In such a sample, the magnetic state that minimizes the energy at low enough field is a vortex. As it is not possible to assign a single macroscopic spin that represents the situation correctly, translating this into the SW model is hardly valid. A possible attempt to derive an easy-plane version of eq.(2.14) would be to assume that the macroscopic spin aligns in the plane perpendicular to \mathbf{n} in a way that is "most parallel" to the magnetic field vector. The validity of the result would probably be quite questionable, and shall therefore be omitted at this point.

Regardless of the anisotropy type, the situation becomes more complicated in the case of intermediate field strengths. The magnetization is oriented in an equilibrium position between \mathbf{h} and \mathbf{n} and the frequency shift becomes a function of the coordinates of the magnetization vector (θ_m, φ_m) . In order to calculate Δf in this regime, it is necessary to minimize the magnetic energy with respect to these coordinates. As a first step, it is necessary to find the orientation of \mathbf{m} , which can be achieved by finding solutions (θ_m, φ_m) for the following minimization conditions for E_m : [31]:

$$\frac{\partial E_m}{\partial \varphi_m} = \frac{\partial E_m}{\partial \theta_m} = 0 \quad (2.15)$$

$$\frac{\partial^2 E_m}{\partial^2 \varphi_m}, \quad \frac{\partial^2 E_m}{\partial^2 \theta_m} > 0 \quad (2.16)$$

Since we operate the cantilever in the small angle regime with $\theta_c \ll 1$, the solutions for θ_m and φ_m , which depend on θ_c , can be approximated by applying a Taylor series up to the first order in θ_c :

$$\varphi_m(\theta_c) \approx \varphi_m(0) + \left. \frac{\partial \varphi_m}{\partial \theta_c} \right|_{\theta_c=0} \cdot \theta_c \quad (2.17)$$

$$\theta_m(\theta_c) \approx \theta_m(0) + \left. \frac{\partial \theta_m}{\partial \theta_c} \right|_{\theta_c=0} \cdot \theta_c \quad (2.18)$$

In this limit, $\theta_m(0)$, $\varphi_m(0)$, $\partial \varphi_m / \partial \theta_c$, and $\partial \theta_m / \partial \theta_c$ can be determined analytically. The found solutions are substituted into E_m and Δf can be calculated. The behavior for an easy axis and an easy plane type situation are very similar and the field-dependent frequency shift as calculated from this model is shown in Fig.(2.3) for the exemplary values $\theta_h = 0^\circ$ ($\mathbf{H} \parallel \mathbf{z}$) and $\theta_h = 90^\circ$ ($\mathbf{H} \parallel \mathbf{x}$).

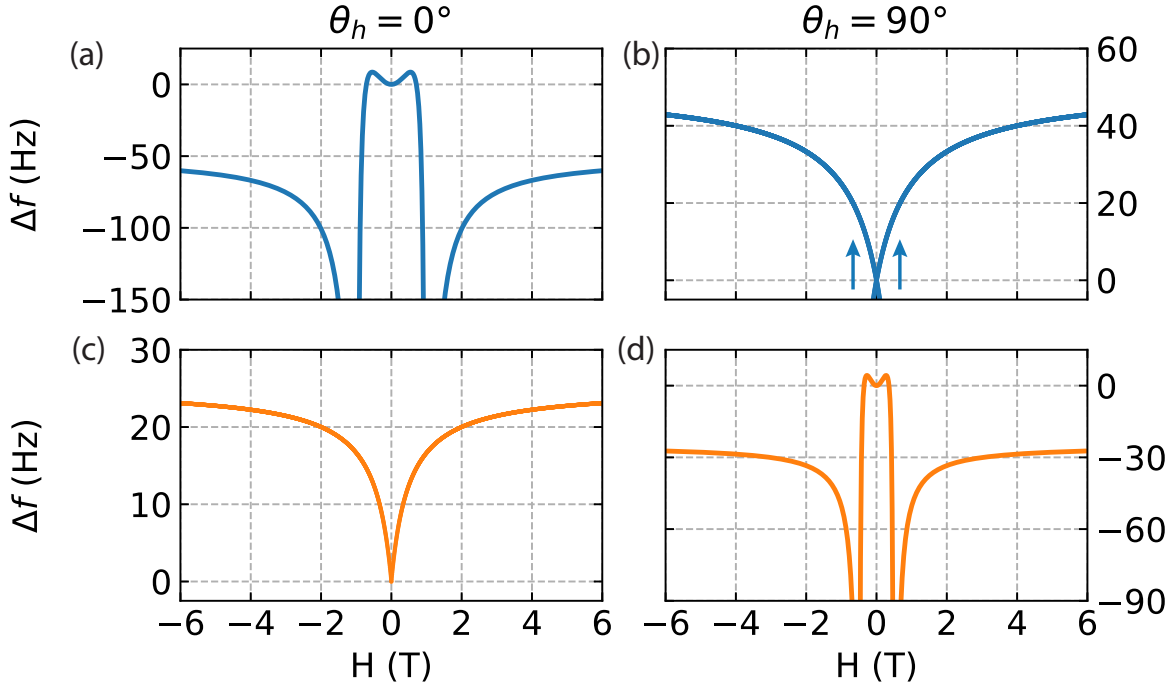


Figure 2.3 | Field dependent frequency shift for SW particles with easy axis (a)-(b) and easy plane (c)-(d) anisotropy. For $\theta_h = 0^\circ$ (e.g. external field along the \mathbf{z} -axis), the easy axis particle (a) exhibits a behavior typical for a magnetic hard direction, while the easy plane particle (c) shows a magnetic easy behavior. The situations switches for $\theta_h = 90^\circ$ (e.g. external field along the \mathbf{x} -axis), where the easy axis particle is shows magnetic easy behavior (b) and the easy plane particle shows magnetic hard behavior (d). The calculations for the curves shown here use the following parameters: $M_s = 1.6 \cdot 10^6 \text{ A/m}$, $f_0 = 5284.79 \text{ Hz}$, $l_e = 74.7 \mu\text{m}$, $V = 1.089155 \cdot 10^{-20} \text{ m}^3$, $k_0 = 165.7 \cdot 10^{-6} \text{ N/m}$. The demagnetization factors D_u are according to the main text.

These particular values correspond to the maxima and minima of the high-field frequency shift plotted in Fig.(2.2).

The curves corresponding to the field alignment with the easy directions in Fig.(2.3) (b) and (c) show a V-shape with positive values for the field strength dependent progression of the frequency shift, which can be understood as follows: The field and the magnetization are parallel to the anisotropy axis for high applied field magnitude. The magnetization remains in this orientation if the field strength is decreased and flips to the opposite direction upon reversal of the external field direction, once a certain threshold value is reached. This corresponds to a jump in the frequency shift indicated by the arrows in Fig.(2.3) (b) and (c). It then again remains in this orientation and flips in the opposite manner, if the field is increased again.

Fig.(2.3) (a) and (d) show the curves corresponding to the field alignment with the hard directions. In this case, the curves show a W-shape with a negative frequency shift. Initially, the magnetization is aligned with the magnetic field, and thus both of them are perpendicular to the anisotropy axis. If the field magnitude is decreased, the magnetization slowly rotates away from the external field towards the anisotropy axis. The beginning of this rotation is associated with a dip in the frequency shift, before it overshoots to small positive values and then crosses the Δf -axis. Magnets with an easy axis symmetry switch hysteretically. This behavior would not be expected for a perfect easy plane anisotropy, as shown in Fig.(2.3) (c) for the easy direction in the easy plane configuration. In experiment, the perfect symmetry

of an easy plane anisotropy is expected to be broken, leading to a preferred axis within the plane and thus magnetic hysteresis. For both hard and easy direction, the full hysteresis curves are symmetric upon field reversal. For any values of θ_h between the ones that maximizes the frequency shift, the field dependent curves transform smoothly between the V and W- shape, with the asymptotic value for high fields following the curve in Fig.(2.2).

Taking geometric relations of the participating vectors into account, the magnetization components can be calculated for some limiting cases. This has been done for both easy axis and easy plane situations and plotted for different values of (θ_n, φ_n) in Refs [31, 72].

In the following, we discuss a peculiarity of the frequency shift in the high-field limit^a. Increasing the magnitude of the external field, the frequency shift value of the high-field limit is approached asymptotically and generally has a constant value that is determined both by the sample's and the cantilever's properties, as well as the magnetic field orientation. Thinking in terms of the standard definition of the torque $\tau_y = \mathbf{m} \times \mu_0 \mathbf{H}$, this is a surprising result, since $\mathbf{m} \parallel \mu_0 \mathbf{H}$ for large fields, and hence $\mathbf{m} \times \mu_0 \mathbf{H} = 0$. Hence, we would expect $\Delta f = -\frac{\partial \tau}{\partial \theta_c}$ to be zero, as well. We have omitted here, however, that we have to take the derivative in the limit of $\theta_c \rightarrow 0$. This means that, even though the absolute value of the torque at $\theta_c = 0$ is zero, the slope of the torque curve $\tau_y(\theta_c)$ in this point e.g. the frequency shift might not be. Thus, we need to have a look at these properties as a function of θ_c . As an attempt to give the reader a more intuitive understanding of this, we show τ and Δf in Fig.(2.4) in dependence of θ_c for the simple case of an easy axis magnet.

Fig.(2.4) shows the curves for the torque and the frequency shift for three specific angles θ_n . The first two columns in Fig.(2.4) show the torque ((a) & (b)) and the frequency shift ((d) & (e)) as a function of the oscillation angle θ_c with $H = 2\text{ T}$ in the first column and $H = 10\text{ T}$ in the second column. The third column ((c) & (f)) shows τ and Δf as a function of the external field magnitude H at $\theta_c \rightarrow 0$. The chosen field angles correspond to the situation where the external field is aligned with the easy axis ($\theta_n = 0^\circ$, blue), hard axis ($\theta_n = 90^\circ$, orange) and an intermediate alignment ($\theta_n = 45^\circ$, green).

We first focus on the curves for $\theta_n = 0^\circ$ and $\theta_n = 90^\circ$. In Fig.(2.4) (a)-(c), it can be seen that $\tau(\theta_c \rightarrow 0) = 0$, as expected. However, the curves for $\tau(\theta_c)$ show sinusoidal behavior and have non-zero slopes at $\theta_c \rightarrow 0$, the values of which depend on the magnitude of the applied field (c.f. situations in (a) and (b)). Taking the derivative after θ_c , this leads to the frequency shift curves $\Delta f(\theta_c)$ shown in Fig.(2.4) (d)-(f). The dependence of the absolute value of $\Delta f(\theta_c \rightarrow 0)$ on the applied field is what creates the $\Delta f(\mathbf{H})$ curve, as indicated by the dashed arrows.

In addition, Fig.(2.4) shows the same kind of curves for $\theta_n = 45^\circ$. For this particular alignment, the asymptotic value of the high-field frequency shift is zero (c.f. Fig.(2.4) (f)), which requires a minimum in the $\tau(\theta_c)$ curve for $\theta_c \rightarrow 0$. This can be seen in Fig.(2.4) (b). At lower fields, the minimum is shifted towards non-zero values of θ_c (c.f. (a)), resulting in a non-zero frequency shift, as shown in (Fig.(2.4) (d) and (f)).

To conclude this discussion, we note that the intuitive picture of $\tau_y = \mathbf{m} \times \mu_0 \mathbf{H}$ can not explain the non-zero values of the frequency shift as soon as $\mathbf{m} \parallel \mathbf{H}$ for high enough fields. Rather than that, it is more instructive to consider τ and Δf as derivatives of the magnetic energy with respect to θ_c .

^aThis has caused several discussions among researchers working on this project, which sparked a more thorough analysis of the problem. The results of this are summarized here.

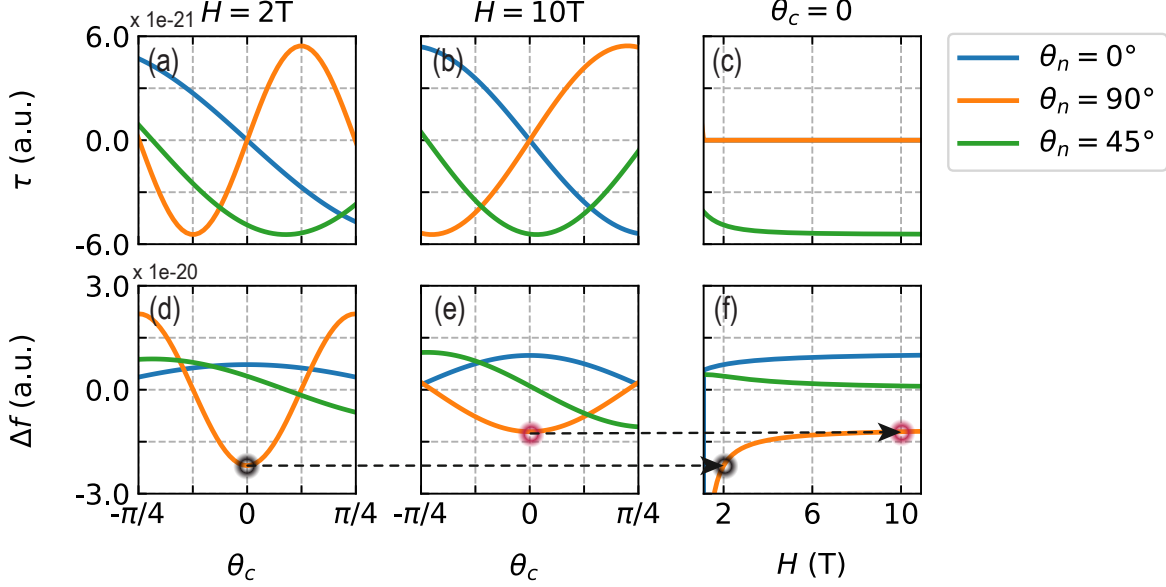


Figure 2.4 | Torque (a)-(c) and frequency shift (d)-(f) as a function of the oscillation angle θ_c at $H = 2$ T ((a) and (d)) and $H = 10$ T ((b) and (e)) as well as the external field magnitude H at $\theta_c = 0$ ((c) and (f)), all for different values of θ_n . The curves are calculated from the Stoner-Wohlfarth model using $\tau = -\frac{\partial E_m}{\partial \theta_c}$ and $\Delta f = \left(-\frac{\partial \tau}{\partial \theta_c}\bigg|_{\theta_c=0}\right)$. Most notably, the torque in (a)-(c) has an absolute value of $\tau_y = 0$ for both $\theta_n = 0^\circ$ and $\theta_n = 90^\circ$ but opposite slopes, with both curves switching signs at their turning points, leading to positive and negative asymptotes. Whereas, for $\theta_n = 45^\circ$, the torque has a minimum which leads to $\Delta f_{hf} = 0$.

2.2.3 DCM in numerical micromagnetics

The model described in the chapters above is a useful tool to extract numerical values for the investigated sample, such as the demagnetization factor, by fitting the model to the measured asymptotes. It can also help to gain a first intuitive understanding of the DCM curves. The model reaches its limitations for magnetic effects that include magnetic switching events or magnetic states that can't be approximated well by using a single macroscopic spin. Analyzing DCM signals with regard to such effects requires a more detailed consideration of the spatial distribution of the magnetic moment within the sample. This is provided by numerical micromagnetic tools, which we will introduce in this chapter.

At the center of the micromagnetic theory is the Landau-Lifshitz-Gilbert (LLG) equation, which describes the magnetization dynamics at nanometer length scale and picosecond timescale [73]. After applying a magnetic field, the magnetization will start to precess around the magnetic field direction on a spiral trajectory caused by a superimposed damping, until \mathbf{m} and \mathbf{H} are fully aligned. The precession frequency is given by [73]

$$f = \frac{\gamma \mu_0 \mathbf{H}_{\text{eff}}}{2\pi} \approx \mu_0 \mathbf{H}_{\text{eff}} \cdot (28 \text{ GHz/T}) \quad (2.19)$$

where $\gamma = ge/2m_e$ is the gyromagnetic ratio, μ_0 the vacuum permeability and \mathbf{H}_{eff} is the effective magnetic field. The damping parameter was phenomenologically introduced by Landau and Lifshitz. Later, Gilbert modified the term such that the damping is proportional to the time derivative of the magnetization. Different micromagnetic solvers may use several more implicit or explicit versions for the equation, but in a general form it reads as follows:

$$\dot{\mathbf{m}} = -\gamma_0 \mathbf{m} \times \mathbf{H}_{\text{eff}} + \alpha \mathbf{m} \times \dot{\mathbf{m}} \quad (2.20)$$

where α is the Gilbert damping factor. In order to solve the equation, the right hand side of eq.(2.20) needs to be integrated. Since it can only be solved analytically for a few special cases, most problems in micromagnetics are solved numerically. This can be done by virtue of finite-difference and finite-element methods.

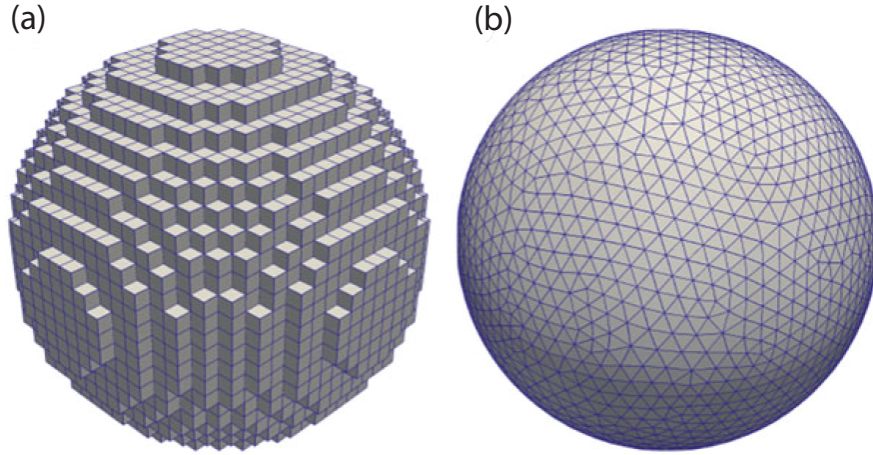


Figure 2.5 | Representation of different mesh types. Finite-difference methods use a mesh of regular rectangular cuboids (a), while finite-elements methods rely on a mesh of potentially irregular tetrahedra (b). Figure adapted from [47]

The integral of the right hand side of eq.(2.20) contains both temporal and spatial parts. To account for the spatial integral over the whole magnetic domain, typically the geometry is discretized in a certain way. The finite-difference method (FDM) uses a regular mesh of rectangular cuboids, in which the magnetization is assumed to be uniform. In contrast, finite-element methods (FEM) use a potentially irregular mesh of tetrahedra. The solution of eq.(2.20) is then approximated at the nodal points of the mesh [73]. Even though it is by far more challenging to make calculations on a GPU (see [74] for more details), FDMs make use of GPUs which makes them orders of magnitude faster than FEM, which rely on calculations on a CPU.

Time integration is typically done using a variety of Runge-Kutta methods [73, 75]. The spatial integral is solved for all cells during one time step and the value for each cell is updated. This process is iterated until the magnetic energy is minimized with an error below a given threshold.

Despite the much shorter computation times of finite-difference methods, it can be of disadvantage in some situations as the use of regular cuboids fails at the correct approximation of curved geometries, as shown in Fig.(2.5). This can induce errors in the solution of the spatial integration which is known as staircase effect. The effect can be reduced to a certain amount by reducing the cell size, which in turn increases the use of memory and computation time. In such a case, FEM methods yield better results at a comparable or reasonably longer computation time.

One important parameter that should be mentioned here is the exchange stiffness A_{ex} . The value of A_{ex} is related to the exchange and the lattice constants of the investigated material

and determines the exchange length $l_{ex} = \sqrt{2A_{ex}/\mu_0 M_s^2}$. The exchange length describes the distance after which a disturbance of the homogeneous magnetization has dropped by a factor $1/e$, where e is Euler's number [76]. In order to obtain reasonable results, the mesh's cell size in the simulation should be smaller than l_{ex} which affects the possible mesh size and computation time of the simulation.

In order to implement the calculation of the frequency shift Δf and the torque τ , we mimic the oscillation of the cantilever by applying the external field in three different directions. First, the simulation is run with the field set in the direction given by (θ_h, φ_h) . The procedure is then repeated with the field tilted by an angle $\tilde{\theta} = \pm\theta_c$. Once the simulation is completed in all three positions, τ and Δf can be obtained from the calculated E_m using the first and second order difference quotient, respectively:

$$\tau \approx -\frac{1}{l_e} \frac{E_m(\tilde{\theta}) - E_m(-\tilde{\theta})}{\tilde{\theta}} \quad (2.21)$$

$$\Delta f \approx \frac{f_0}{2k_0 l_e^2} \frac{E_m(\tilde{\theta}) + E_m(-\tilde{\theta}) - 2E_m(0)}{(\tilde{\theta})^2} \quad (2.22)$$

The cantilever itself is represented only by the pre-factors in eqs.(2.21)-(2.22). f_0 is the frequency of the magnet-on-cantilever system when no magnetic field is applied. The spring constant k_0 and the effective length l_e need to be calculated in a finite-element software (for example COMSOL), typically by adjusting for small variations of the cantilever's geometry. This is iterated until the resonance frequency calculated via COMSOL fits f_0 as measured the experiment. The cantilever dependent factor only provides a scaling of the curves calculated from the magnetic energy and does not interfere with the solution of the LLG equation.

Matching the measured DCM curves with the simulated frequency shifts allows for analysis of the data by correlating features in the curves with corresponding magnetization maps. This has been used for example to investigate vortex states in CoFeB nanowires [77] and to analyze the data reported later on in ch.(3).

2.3 Micromagnetic methods - Applications

2.3.1 Thermal activation: Superparamagnetic particles

The descriptions in the previous chapters are valid for ferromagnetic nano-particles and yield decent results in many cases. The Stoner-Wohlfarth model introduced above, however, doesn't consider any temperature dependence or effects related to a change in the sample temperature and therefore its results compare to a magnetic system at very low temperature. For ferromagnetic particles with a size and shape where the model applies well, this is not very problematic. It becomes of particular interest, if the size of the magnetic particle is small enough that the energy due to thermal activation becomes large in comparison to the anisotropy energy [78]. Under these conditions, the direction of the macro-spin is no longer stable and pointing along the anisotropy axis, but rather flips between its stable positions at a high rate and thus averages itself to zero. Having no net magnetic moment at zero applied field but magnetizing as soon as a field is applied, the sample is then called superparamagnetic: It exhibits the behavior of a paramagnet despite its inherently ferromagnetic nature. The size below which a particle becomes superparamagnetic depends on its specific morphology and material properties and

is typically on the order of a few tens of nanometers [78]. Subject to decreasing temperature, the fluctuations stop when the thermal energy is too small to flip the magnetic moment. The magnetization then stays in a stable orientation and the superparamagnetism blocks. In accordance to this, the corresponding temperature is called blocking temperature T_B .

A model for the DCM response of such a particle in form of an individual, thermally activated Stoner-Wohlfarth particle has first been developed in [79] and will be introduced in this chapter, following Refs.[79, 80]. The Hamiltonian of the magnetic system is given by energy terms as summarized in eq.(2.11) and we write $\mathcal{H} = \mathcal{H}_{\text{Zeeman}} + \mathcal{H}_{\text{uniaxial}}$. Again, we incorporate oscillations of the cantilever, which correspond to rotations of \mathbf{n} around the \mathbf{y} -axis by an oscillation angle θ_c via the application of a rotation matrix $\underline{\mathbf{R}}_y(\theta_c)$ to \mathbf{n} . The partition function of the system is given by:

$$\mathcal{Z} = \frac{1}{2\pi} \int_0^\pi d\theta_m \sin \theta_m \int_0^{2\pi} d\varphi_m \exp \left[-\frac{\mathcal{H}(\theta_m, \varphi_m)}{k_B T} \right], \quad (2.23)$$

where θ_m and φ_m are the polar and azimuthal angles of \mathbf{m} . This yields the free energy through

$$\mathcal{F}_m = -k_b T \ln \mathcal{Z} \quad (2.24)$$

Once all parameter values are set, the integral over θ_m and φ_m can be evaluated numerically. Analogous to the previous chapters, using the difference quotient to approximate the second derivative in eq.(2.4), we then calculate the frequency shift of the cantilever.

To show the effect of the temperature dependence, we calculate Δf of a magnetic particle for two different temperatures, one at $T = 5$ K leading to a blocked state and the other one at $T = 300$ K leading to a superparamagnetic state. We do the calculations for both easy and hard orientation, e.g with $\mathbf{H} \parallel \mathbf{n}$ and $\mathbf{H} \perp \mathbf{n}$, as shown in Fig.(2.6). The following parameters were used in this case: $f_0 = 5$ kHz, $l_e = 100$ μm , $k_0 = 100$ $\mu\text{N/m}$, $\theta_c = 1^\circ$, $V = 1000$ nm^3 , $M_s = 300$ kA/m, $D_u = -0.1$, $\varphi_n = 0$, and $\theta_n = 90^\circ$.

In the $\mathbf{H} \parallel \mathbf{n}$ configuration, the difference between the curves at 300 K and 5 K is small: the curve at 300 K is broader and approaches the horizontal asymptote more slowly than the curve at 5 K. In the $\mathbf{H} \perp \mathbf{n}$ configuration, however, the curves behave in a fundamentally different way. The curve at 300 K is similar to the case of $\mathbf{H} \parallel \mathbf{n}$, but mirrored across $\Delta f = 0$. The curve at 5 K has a distinct W-shape for low fields (see the inset of Fig.(2.6), approaching the horizontal asymptote from negative rather than positive values of Δf . This curve matches the DCM curves calculated from the ferromagnetic Stoner-Wohlfarth model introduced in the previous chapters (compare also Ref. [31]). There is a difference to the model in ch.(2.2.2.1) at low fields, where Δf overshoots to positive values as can be seen in Fig.(2.3) (a) and (d), but not in the model here. We ascribe this to a difference in methodology, as introducing a temperature dependence required to use a more complex statistical model. In the previous one we used a direct energy minimization which represents a more idealized case. In the $\mathbf{H} \perp \mathbf{n}$ case, the distinction between the Λ - and W-shape of the DCM curve can be used to identify the para- or ferromagnetic state of a magnetic specimen of the given geometry.

To understand the progression of \mathbf{M} with external field and the differences in the curves for different temperatures, it is instructive to look at the equilibrium probability distribution of magnetic moments, which is given by

$$P_e(\theta_m, \varphi_m) = \frac{\exp[-\mathcal{H}(\theta_m, \varphi_m)/k_b T]}{\mathcal{Z}} \quad (2.25)$$

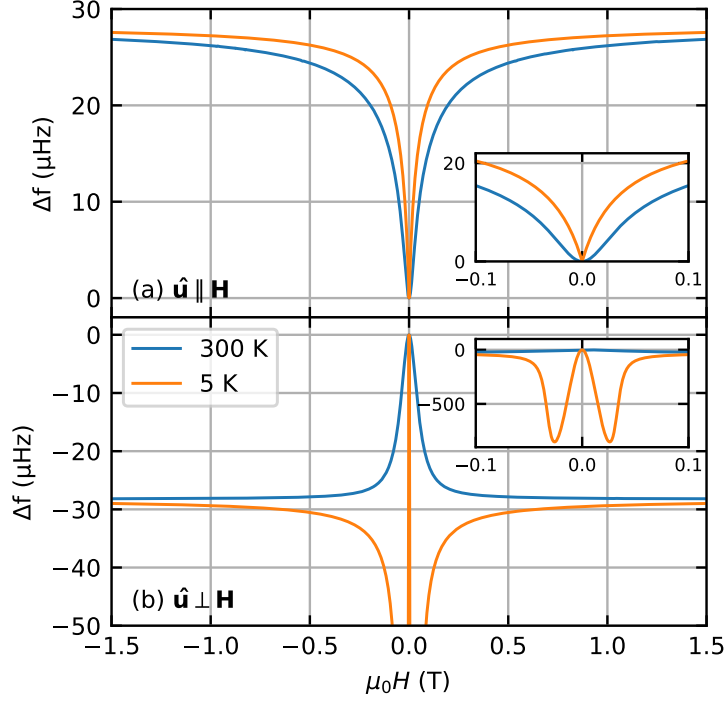


Figure 2.6 | Simulation of DCM for an individual, thermally-activated Stoner-Wohlfarth particle at $T = 300$ and 5 K. Simulated $\Delta f(H)$ with (a) $\mathbf{H} \parallel \mathbf{n}$, and (b) $\mathbf{H} \perp \mathbf{n}$. Graph is adapted from [79]

Integrating P_e over φ_m and plotting it as a function of $m_z = M_z/M_s = \cos(\theta_m)$ for a few values of the external field, illustrates the difference between the blocked and the superparamagnetic state, see Fig.(2.7).

For the sake of consistency with Ref. [79] and for didactic reasons, we break with the convention established in the previous models, that the direction of \mathbf{n} is fixed at $\theta_n = 90^\circ$ and θ_h is rotated. Instead, we fix the external field at $\theta_h = 0$ along the \mathbf{z} -axis and rotate \mathbf{n} . The established convention of fixing \mathbf{n} and rotating θ_h would not affect the validity of the model but would require a slightly different description compared to Ref. [79].

In (a), we plot the probability for $\mathbf{H} \parallel \mathbf{n}$. For the ferromagnet at 5 K (green), there are very sharp maxima at $m_z = \pm 1$ for $H = 0$. This means that \mathbf{M} favors alignment with \mathbf{n} , where parallel and anti-parallel alignment are equally probable. Away from these two peaks, P_e is essentially zero, i.e. the magnetization is very unlikely to point in any direction other than along \mathbf{n} . Switching on a slight external field ($\mu_0 H = 10$ mT), the peak at $m_z = -1$ vanishes, and only $m_z = +1$ is favored (dashed red curve).

Although not obvious in the DCM curves, P_e shows how this behavior differs from the paramagnetic behavior at 300 K (blue and orange curves). Here, $\mathbf{M} \parallel \mathbf{n}$ is still favored, but the probability for \mathbf{M} to point in any other direction is not negligible. Switching on a small external field has a much smaller effect on P_e at 300 K than at 5 K, which explains why the DCM curve for the paramagnetic case is broader than the ferromagnetic one.

Similar effects can be observed for $\mathbf{H} \perp \mathbf{n}$, see Fig.(2.7) (b). Let's first look at the ferromagnetic case: In this situation, \mathbf{n} is aligned with the \mathbf{x} -axis, while \mathbf{H} remains parallel to the \mathbf{z} -axis. Since $\mathbf{m} \parallel \mathbf{n}$ for $\mathbf{H} = 0$, the probability that \mathbf{m} points along \mathbf{z} is practically zero, which is reflected by the peak for $P_e(m_z)$ at $m_z = 0$.

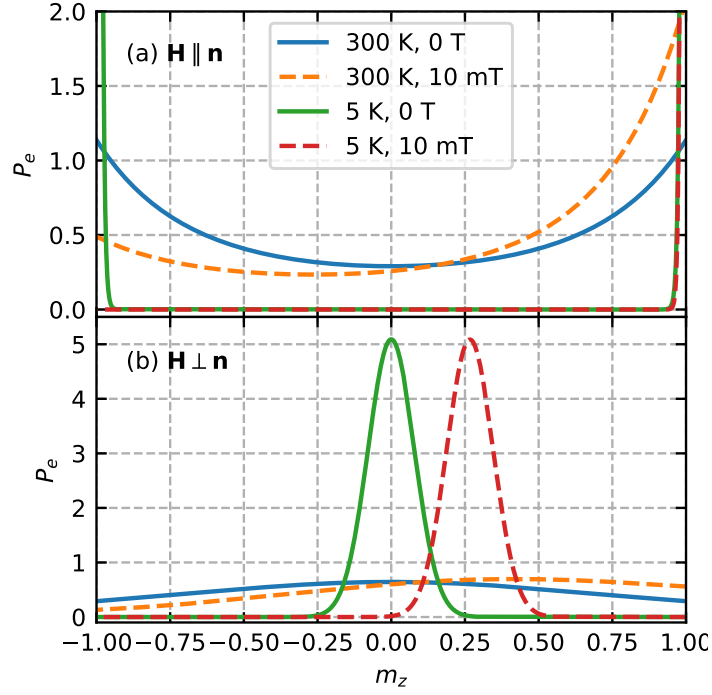


Figure 2.7 | P_e for an individual, thermally activated Stoner-Wohlfarth particle with (a) $\mathbf{H} \parallel \mathbf{n}$, and (b) $\mathbf{H} \perp \mathbf{n}$. Graph is adapted from [79]

Applying a magnetic field, the magnetic moment rotates away from \mathbf{n} and towards \mathbf{H} . This causes a shift of the peak towards $m_z = 1$, which is reached as soon as the magnetic moment is aligned with the field. For the paramagnetic case, the situation is very similar, only the peaks are vastly smeared out, resulting in very broad probability distributions. The macro spin may in this case fluctuate significantly in a broad range of directions, which appears in the DCM curve by avoidance of the dips of the W-shape and formation of the Λ -shape.

2.3.2 DCM and susceptibility

In standard laboratory magnetometry, the total magnetization of a sample can be measured for example via a vibrating sample magnetometer (VSM). VSMS often make use as superconducting quantum interference devices (SQUIDS) as a sensitive detector. For this method, a sample vibrates in a magnetic field between two pick-up coils that are coupled to a SQUID, which detects the flux variations as a function of the applied field, which can be related to the magnetization of the sample. The slope of the obtained magnetization curve can in general be described by a dimensionless tensor called magnetic susceptibility $\chi_{i,j}$

$$\chi_{i,j} = \frac{\partial M_i}{\partial H_j} \quad (2.26)$$

In general, the components of \mathbf{M} can react differently to the different components of \mathbf{H} . However, in the following, we only consider diagonal entries of $\chi_i = \partial M_i / \partial H_i$ of the susceptibility tensor for the sake of simplicity. Typically, the susceptibility is dependent on the

frequency ω_{Hac} of the applied ac magnetic field and one can distinguish between DC and AC susceptibility.

If this frequency is low enough, e.g. $2\pi/\omega_{Hac} \ll t_{mag}^c$, where t_{mag}^c is the characteristic timescale on which the magnetization dynamics of the given sample takes place, the magnetic moment align well with the applied field. If $1/\omega_{Hac} > t$, which e.g. typically happens if phase boundaries are crossed, the magnetic moments can not follow the oscillating field anymore, the susceptibility becomes imaginary and the imaginary part $\chi_{i,j}^{im}$ can be interpreted as a measure for dissipative processes [81].

The thermodynamic potential for the Gibb's free energy of a magnetic system is given by [82]

$$dG = -SdT + VdP - \mu_0 V_m \mathbf{M}d\mathbf{H} \quad (2.27)$$

where T is the temperature, S the entropy, P the pressure, V the volume of the thermodynamic system. The magnetization and susceptibility can be expressed as a derivative of the magnetic energy with respect to the external field:

$$M_i = -\frac{\partial G}{\partial H_i} \quad \text{and} \quad \chi_i = -\frac{\partial^2 G}{\partial H_i^2} \quad (2.28)$$

This allows for a comparison of magnetization and susceptibility with the torque and the frequency shift in DCM, as given by table (2.1). The difference between the two sets of properties is the fashion in which the external field oscillates. While for \mathbf{M} and χ the field is oscillating linearly, in DCM the field is oscillating around an angle θ_c , induced by the motion of the cantilever.

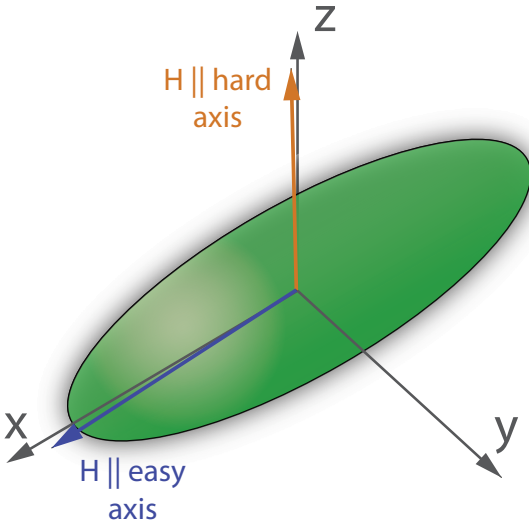


Figure 2.8 | Field direction with respect to the magnetic particle for hard and easy axis orientation.

We study the differences and similarities of the two situations by means of micromagnetic simulations of a prolate ellipsoid using Mumax3. As indicated in Fig.(2.8), the long axis of the ellipsoid is aligned with the x direction of the coordinate system, which, in the experiment, coincides with the long axis of the cantilever. The system is in the magnetic easy configuration for the external field parallel to the the \mathbf{x} axis with $\theta_h = \pi/2$, as indicated by the blue arrow in Fig.(2.8). Accordingly, the system is in a hard axis configuration, if the field is perpendicular to \mathbf{x} .

Note that the direction of the external field is off by the perfect alignment by 2 and 1 degrees in θ and φ direction, respectively, in order to prevent the system from entering an energetically metastable state. The calculation of Δf and τ is done as explained in

ch. (2.2.3). For simplicity, we omit the cantilever dependent pre-factor, which only accounts for a scaling of the absolute value of Δf .

Although the magnetic energy and the magnetization components are calculated by default in micromagnetic simulations, it is necessary to also simulate the measurement with a linearly

oscillating field in order to obtain a valid comparison. Hence, to mimic the VSM measurement, the magnetic energy is minimized with a small linear field on the order of 2% of the external field strength added first in positive, then in negative direction of each vector component of the external field, and with the external field in its main direction in order to calculate the three magnetization components. Using the difference quotient, we obtain

$$M_z \approx \frac{E_m(\delta H_{ac}) - E_m(-\delta H_{ac})}{\delta H_{ac}} \quad (2.29)$$

for the magnetization and

$$\chi_z \approx \frac{E_m(\delta H_{ac}) + E_m(-\delta H_{ac}) - 2E_m(0)}{(\delta H_{ac})^2} \quad (2.30)$$

for the susceptibility. In order to verify this procedure, we show in Fig.(2.9) (a)-(b) the results for the magnetization components for both the magnetic easy and hard direction as calculated by default from MuMax3 (blue circles) with the results according to eq.(2.29) (orange curve).

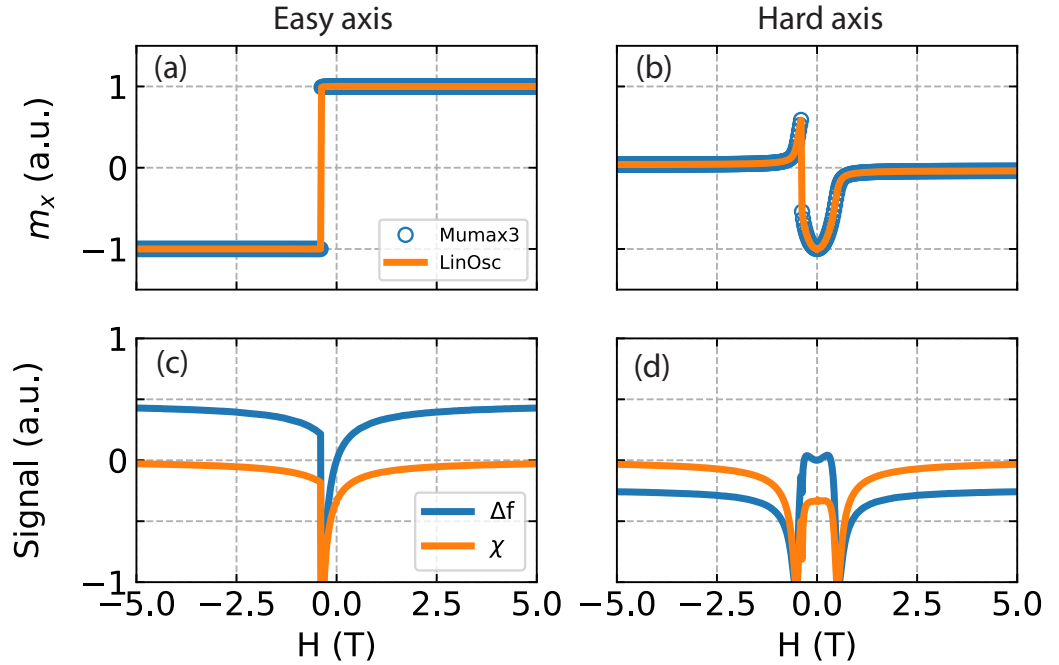


Figure 2.9 | The top row shows m_x for both easy (a) and hard axis (b) alignment of the external field (c.f. Fig.(2.8)). The two curves correspond to the magnetization components as calculated from Mumax3 (blue circles) and for a linearly oscillating field according to Eq.(2.29). Bottom row shows the corresponding frequency shift (blue curve) and susceptibility (orange cure). Curves in (c) and (d) are scaled for better comparability.

The field is swept form positive to negative direction, thus representing half a hysteresis curve. The results match each other perfectly. We can see a sudden jump in the easy axis curve when the magnetization flips its direction at a coercive field with a negative value. For the hard axis alignment, where the external field is perpendicular to the x direction, m_x is zero at first, and then rotates smoothly into the easy direction. At negative fields, the rotation is first continued before it flips direction and approaches zero from negative values.

Therefore eqs. (2.29) and (2.30) obtain valid results and we now proceed to compare the frequency shift Δf with the susceptibility χ , as plotted in Fig.2.8 (c)-(d). The curves have very similar shape, but are scaled for better comparability. Again, the external field strength is swept from positive to negative values. For both orientations, χ and Δf approach a horizontal asymptote for large values of H_x , differing in their asymptotic value. While the susceptibility approaches zero from negative values, the value of the asymptote for Δf depends on the orientation of the external field, as described in the chapters above. Magnetic switching is visible equally in both curves. The dips in the hard axis curve in Fig.2.8 (d) correspond to the rotation of the magnetic moments from the anisotropy axis towards the external field, as the field is increased (c.f. behavior of m_x in (b)).

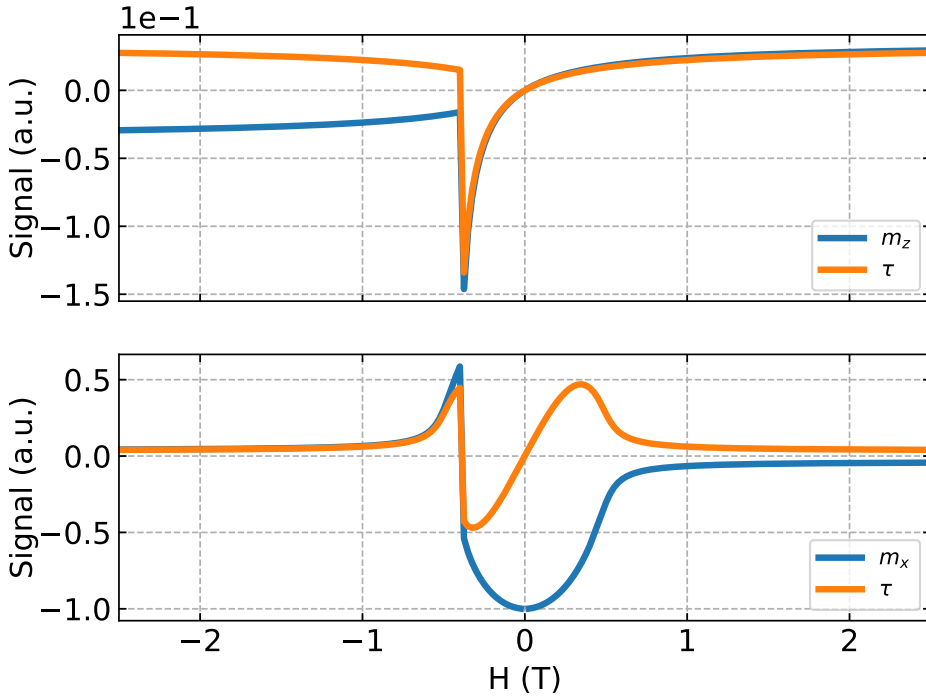


Figure 2.10 | Simulated torque and magnetization component for both easy (upper plot) and hard (lower plot) orientation.

In Fig.(2.10), we plot the simulated static torque for both field orientations. In order to get a valid comparison, we have to choose the correct magnetization component. In the easy axis orientation, we compare to the m_z component, while for the hard axis, we compare to the m_x component. The curves carry similar information as the magnetization component we compare them to. One drawback, however, is that the torque curves don't reflect the orientation of the external field for high field values. Also, for $\mathbf{H} = 0$ the torque is zero.

In conclusion, the simulations show, that the frequency shift retrieved from DCM can be regarded as a rotational analog to a susceptibility measurement with a linearly oscillating magnetic field. The results for the static torque compared to its corresponding magnetization components have to be interpreted more carefully, as the curve show some qualitative disagreements, while still containing similar information.

2.4 Detecting Phase transitions

2.4.1 Introduction

The theory of thermodynamic phase transitions goes back to 1822 where Charles Caignard de la Tour characterized the transition between liquid and gas phases in alcohol by a triplet of values: temperature, pressure and volume [83]. The work of van der Waals 1873 and Pierre Curie 1895 lead to a first equation of state and the discussion of the transition temperature, after which ferromagnetism occurs, now known as Curie temperature. Based on the findings of an unusual phase transition in liquid helium by W.H. Keesom in 1932, Paul Ehrenfest introduced the first comprehensive scheme for classifying phase transitions, which is today known as Ehrenfest classification [83, 84].

Ehrenfest's classification is based on the description of the Gibb's free energy G of a given system and its respective derivative: If a system that passes a phase transition is continuous in G but discontinuous in its first derivatives, it is classified as a first-order phase transition. Consequently, if G and its first derivatives are continuous, but not the second derivatives, it is classified as second-order transition. There is no intrinsic limit on how high an order of a phase transition can be and while Ehrenfest mentioned higher-order transitions, he studied only first and second-order [83]. In reality, however, it becomes less and less clear whether it is still reasonable to think of a phase transition for higher orders, since the discontinuities in the derivatives becomes less and less significant so that typically only the first and second order are of interest ^b. [85].

Essentially, according to Ehrenfest's work, all information about phase transitions is contained in G . In a thermodynamic framework, magnetization and susceptibility are the first and second derivatives of the free energy at a constant temperature T . In a similar way, the specific heat C can be derived as the second derivative of the free energy at constant external field H and/or constant magnetization M via the internal energy or the entropy, respectively. We have shown in the previous chapters that, being derivatives of E as well, the torque τ and the frequency shift Δf , can be compared to the magnetization and the the magnetic susceptibility with respect to an oscillating magnetic field, induced by the motion of the cantilever. Consequently, these properties can be linked to other thermodynamic coefficients like C or χ via the Ehrenfest relations. This has been done in 2018 by Modic *et al.* [32] and we follow their derivation in order to establish a framework for measurements of phase transitions with DCM.

While phase transitions in ferromagnetic systems have been studied intensively for a long time, they also play an important role in the more recently discovered class of non-collinear magnetic systems, such as chiral magnets. Besides ferromagnetic states, these materials can host magnetic states, where the magnetization is not only aligned parallel anymore, but also in helices, spirals, cones or whirlpool- like structures called magnetic skyrmions. Mapping out magnetic phase diagrams of those materials is of interest both for basic science and potential applications in fields like data storage or spintronics. As we will see in this chapter, DCM is a powerful tool to detect those transitions. Subsequently, we will compare susceptibility measurements from the literature to DCM measurements on the same materials in order to verify the procedure. Note that an introduction to non-collinear magnetism can be found in ch.(5.2)

^bSee Ref [85] for a more detailed discussion of higher order transitions

2.4.2 DCM properties in a thermodynamic framework

2.4.2.1 Basic example: Susceptibility at paramagnetic to ferromagnetic transition

We establish an understanding of the processes happening at phase transitions by having a look at the paramagnetic to ferromagnetic transition in a ferromagnetic material with the Curie temperature T_c . We follow [82], starting at Gibbs free energy

$$dG = -SdT + VdP - \mu_0 V_m \mathbf{H}d\mathbf{M} \quad (2.31)$$

We assume the pressure P to be constant and (following the approach of Landau-Lifshitz) [86] expand for M around T_c :

$$G = G_0 + a(T - T_c)M^2 + bM^4 \quad (2.32)$$

where a and b are numbers. The energy is now a function of the magnetization and the temperature, including T_c as a coefficient. In Fig.(2.11) (a) we plot G as a function of the magnetization at different temperatures above and below T_c . For $T > T_c$, the energy has the shape of a parabola with a minimum at $M = 0$. Lowering the temperature, it evolves into a mexican-hat shape with the minima being symmetric around $M = 0$ after passing T_c . For an equilibrium state of the magnetization, the energy needs to be minimized, so naturally, the value of the equilibrium magnetization follows the behavior of the energy minima, whose positions we find as follows:

$$\left(\frac{\partial G}{\partial M}\right)_T = 0 = 2a(T - T_c)M + 4bM^3 \quad (2.33)$$

The solutions for this are:

$$M = 0 \quad \text{and} \quad M^2 = -\frac{a(T - T_c)}{2b} \quad (2.34)$$

Setting $M = 1$ at $T = 0$ one can obtain T_c :

$$T_c = \frac{2b}{a} \quad (2.35)$$

In the following example, we choose a and b such that $T_c = 8K$, for no particular reason. The energy minimum at $M = 0$ for $T > T_c$ indicates that the distribution of the magnetic moments is such that the overall magnetization cancels out, which is true for a paramagnet. Passing T_c , the minimum transforms in a maximum and the $M = 0$ state is not favorable anymore. The magnetization can now be used as an order parameter for the magnetic state of the system. Whether the positive or the negative minimum state is realized depends on different factors such as external fields or anisotropies. In a perfectly isotropic system with no external influences, this is a process of spontaneous symmetry breaking and realization of each of the states have the same probability.

The magnetization shown in Fig.(2.11) (b) follows a parabolic curve for $T < T_c$, as given by eq.(2.34). Below T_c , the material is in the ferromagnetic phase with the magnetization now serving as the corresponding order parameter. The onset of the latter causes the material to exhibit a non-zero susceptibility, which results in a sharp jump from zero to a finite value as the temperature crosses T_c coming from high temperatures. This is shown in Fig.(2.11) (c). This behavior is indicative of a magnetic phase transition and can occur not only in paramagnetic to ferromagnetic transition but also between substates that incorporate a change in susceptibility.

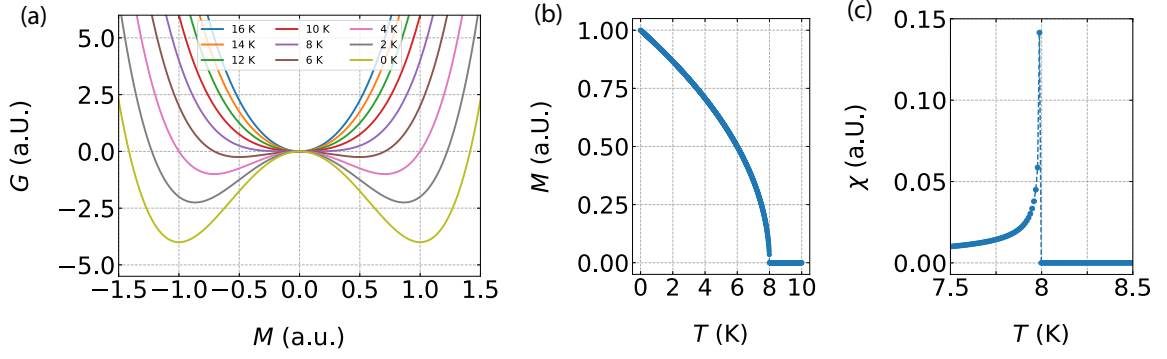


Figure 2.11 | Paramagnetic to ferromagnetic transition of a ferromagnet with $T_c = 8$ K. (a) shows the magnetic energy as a function of the magnetization at different temperatures. The energy transforms from a parabola with a minimum at $M = 0$ to a symmetric mexican-hat shaped curve with a maximum at $M = 0$. (b) plots the position of the positive minimum as a function of temperature at $\mathbf{H} = 0$ T. The susceptibility $\chi = \partial \mathbf{M} / \partial \mathbf{H}$ is shown in (c), exhibiting a sharp peak at the transition temperature.

2.4.2.2 Relation between thermodynamic properties

We can build a thermodynamic potential for a magnet-on-cantilever system similar to eq.(2.31) by considering the potential energy of a magnet, given by

$$U_{mag} = -V_m \mathbf{M} \cdot \mu_0 \mathbf{H}. \quad (2.36)$$

To build the differential, we consider the change of the potential energy with respect to an infinitesimal rotation by an angle $d\theta$ about some rotation axis $\boldsymbol{\eta}$:

$$\begin{aligned} \frac{dU_{mag}}{d\theta} &= -\mu_0 V_m \frac{d\mathbf{M}}{d\theta} \cdot \mathbf{H} - \mu_0 V_m \mathbf{M} \cdot \frac{d\mathbf{H}}{d\theta} \\ &= -\mu_0 V_m (\boldsymbol{\eta} \times \mathbf{M}) \cdot \mathbf{H} - \mu_0 V_m \mathbf{M} \cdot \frac{d\mathbf{H}}{d\theta}. \end{aligned} \quad (2.37)$$

The term $\frac{d\mathbf{M}}{d\theta}$ in this equation has been replaced with $\boldsymbol{\eta} \times \mathbf{M}$. This identity can be found by using the general formula for actively rotating a vector by an angle θ about $\boldsymbol{\eta}$, known as Rodrigues' rotation formula:

$$\mathbf{r}' = \mathbf{r} \cos(\theta) + \boldsymbol{\eta} (\boldsymbol{\eta} \cdot \mathbf{r}) [1 - \cos(\theta)] + (\boldsymbol{\eta} \times \mathbf{r}) \sin(\theta) \quad (2.38)$$

For an infinitesimal rotation ($\theta \rightarrow d\theta$, $\cos(d\theta) \rightarrow 1$, $\sin(d\theta) \rightarrow d\theta$), eq.(2.38) reduces to

$$\mathbf{r}' - \mathbf{r} = d\mathbf{r} = (\boldsymbol{\eta} \times \mathbf{r}) d\theta \quad (2.39)$$

which gives the desired identity by dividing through $d\theta$.

Rearranging the scalar triple product in the first term of the last part of eq.(2.37), and identifying the magnetic torque $\boldsymbol{\tau}$ we get

$$\begin{aligned} \frac{dU_{mag}}{d\theta} &= -\boldsymbol{\eta} \cdot (V_m \mathbf{M} \times \mu_0 \mathbf{H}) - \mu_0 \mathbf{M} \cdot \frac{d\mathbf{H}}{d\theta} \\ &= -\boldsymbol{\eta} \cdot \boldsymbol{\tau} - \mu_0 V_m \mathbf{M} \cdot \frac{d\mathbf{H}}{d\theta}. \end{aligned} \quad (2.40)$$

Multiplying with $d\theta$ gives the final result:

$$dU_{mag} = -\boldsymbol{\eta} \cdot \boldsymbol{\tau} d\theta - \mu_0 V_m \mathbf{M} \cdot d\mathbf{H} \quad (2.41)$$

Note that this is true for any rotation axis $\boldsymbol{\eta}$. In the following, we choose $\boldsymbol{\eta} = \mathbf{y}$ in consistency with our experimental setup and thus $\boldsymbol{\eta} \cdot \boldsymbol{\tau} = \tau_y \equiv \tau$ and $d\theta = \theta_c$. The Helmholtz free energy is obtained by Legendre transformation of $dU = TdS - pdV + dU_{mag}$ and is given by [32]

$$dF = -SdT - PdV - \mu_0 V_m \mathbf{M} \cdot d\mathbf{H} - \tau d\theta \quad (2.42)$$

For the magnetic phase transitions, in which we are interested here, we expect that no change in volume (or pressure) occurs, so $-PdV$ vanishes. Note that the torque term only exists, if there is magnetic anisotropy present, and the last two terms correspond to E_m as given in eq.(2.2).

To relate the thermodynamic quantities given in eq.(2.42), we assume a second order phase transition, so the energy is the same at two points A and B on the phase boundary between phase 1 with energy F_1 and phase 2 with energy F_2 :

$$F_1 = F_2 \quad (2.43)$$

First we look at a magnetic field driven phase transition, so the temperature is constant:

$$dF = -\mu_0 V_m \mathbf{M} \cdot d\mathbf{H} - \tau d\theta. \quad (2.44)$$

Further, for a second order phase transition the first derivatives do also not change. Let's first analyze the magnetization:

$$\left(\frac{\partial F_1}{\partial H} \right)_\theta = \left(\frac{\partial F_2}{\partial H} \right)_\theta \Leftrightarrow \Delta M_A(H, \theta) = 0 \quad (2.45)$$

where $\Delta M_A = M_1 - M_2$ at point A as given by the derivatives. Moving an infinitesimally small step along the phase boundary, to point B, this reads as $\Delta M_B(H + dH, \theta + d\theta)$. A Taylor expansion of ΔM_B results in:

$$\left(\frac{\partial M_1}{\partial H} \right)_\theta dH + \left(\frac{\partial M_1}{\partial \theta} \right)_H d\theta = \left(\frac{\partial M_2}{\partial H} \right)_\theta dH + \left(\frac{\partial M_2}{\partial \theta} \right)_H d\theta \quad (2.46)$$

Sorting after equal derivatives yields

$$\Delta \left(\frac{\partial M}{\partial H} \right)_\theta dH + \Delta \left(\frac{\partial M}{\partial \theta} \right)_H d\theta = 0 \quad (2.47)$$

By using the definition of the susceptibility and the Maxwell relations [87] between the magnetization and the torque

$$\left(\frac{\partial M}{\partial \theta} \right)_H = - \left(\frac{\partial \tau}{\partial H} \right)_\theta \quad (2.48)$$

we can rewrite eq.(2.47) as follows:

$$\Delta \chi dH - \Delta \left(\frac{\partial \tau}{\partial H} \right)_\theta d\theta = 0 \quad (2.49)$$

This can be done in the same manner for the torque, which gives

$$\Delta \left(\frac{\partial \tau}{\partial H} \right)_\theta dH + \Delta \left(\frac{\partial \tau}{\partial \theta} \right)_H d\theta = 0 \quad (2.50)$$

in analogy to eq.(2.47). Solving eq.(2.50) for $\Delta \left(\frac{\partial \tau}{\partial H} \right)_\theta$ and inserting into eq.(2.49), we can establish the following relation between the frequency shift and the susceptibility:

$$\Delta f = -\Delta \chi \left(\frac{dH}{d\theta} \right)^2 \quad (2.51)$$

It is a straight forward task to link the susceptibility with the specific heat C using the exact same path for phase transition with a constant θ . We assume the difference in entropy and magnetization in the two phases to be a function of the temperature and the external field. Then we Taylor-expand both properties, and use the Maxwell relation between magnetization and entropy as well as the identity $(\partial S / \partial T)_H = C/T$. Then we can relate the susceptibility with the specific heat as follows:

$$\Delta \chi = \frac{\Delta C}{T} \left(\frac{dT}{dH} \right)^2 \quad (2.52)$$

Inserting this into eq.(2.51) yields the relation between the specific heat and the frequency shift.

$$\Delta f = -\frac{\Delta C}{T} \left(\frac{dT}{d\theta} \right)^2 \quad (2.53)$$

Note that eq.(2.53) could have been derived analogous to eq.(2.51) and eq.(2.52) instead.

2.4.2.3 Comparison of phase transition measurements using different methods

The model system in ch.(2.4.2.1) has shown a peak in the susceptibility around the transition temperature. Given the relations established above, we expect a similar behavior for the frequency shift and the specific heat. To verify this, we compare measurements on the chiral magnet MnSi [88] from the literature with data from our lab. The magnetic phase diagram of this material hosts non-collinear magnetic states such as a helical ground state, a conical state and a skyrmion lattice state. These magnetic phases and their transition values have been studied using a large variety of experimental techniques including magnetic susceptibility and dynamic cantilever magnetometry, and it thus qualifies perfectly as a model system to compare the data.

Specifically, we compare data from two studies by Bauer *et al.* using magnetic susceptibility [89] measurements with data taken in our lab using DCM and published in Mehlin *et al.* [33]. In both publications, the magnetic phase diagram was mapped out and the values of transition temperatures and fields compare sufficiently well.

In Ref. [89], the material was investigated measuring real and imaginary part of the magnetic susceptibility at the same time, both as a function of temperature and external field. We show the field dependent data in Fig.(2.12) next to similar measurements of a MnSi nanowire, using DCM [33].

The real part of the susceptibility shows several distinct features at different field values, that are also dependent on the temperature. The curves between ca. 28 K and 25 K all similarly show a parabolic behavior during the helical phase below 0.1 T, followed by two peaks around 0.1 T and 0.2 T where the system enters and exits the skyrmion phase. After those peaks, the

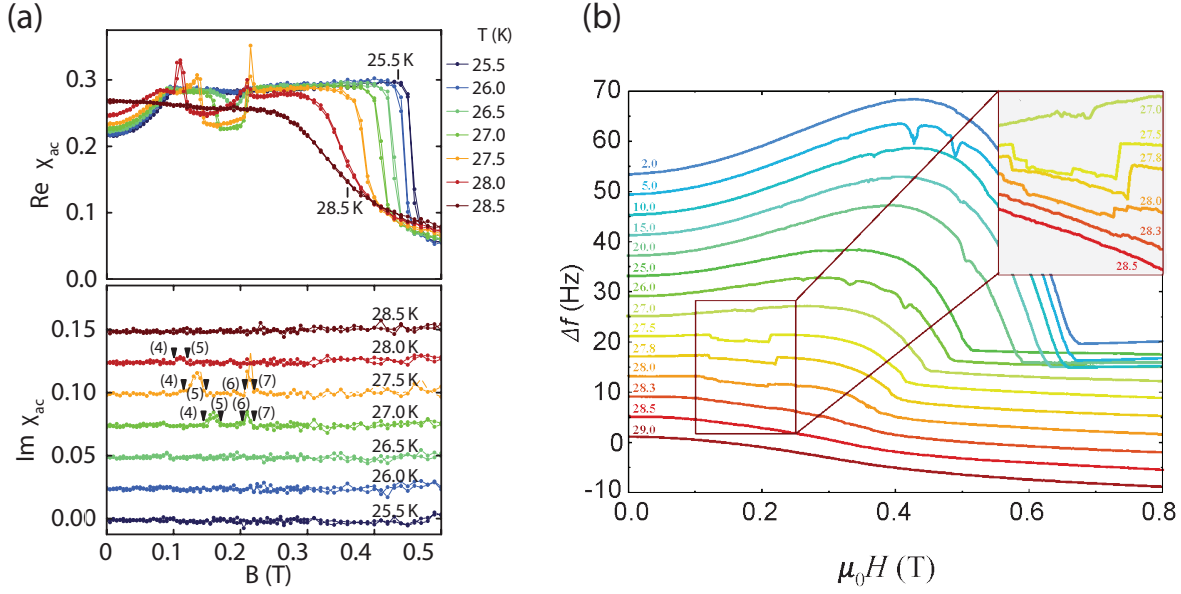


Figure 2.12 | (a) Real and imaginary part of the susceptibility and (b) frequency shift data of a MnSi sample. Graphs adapted from [89] and [33].

signal has a short linear part where the conical phase is modulated by the external field before it enters a fully field polarized state. For even lower temperatures, the signal transitions from the parabolic behavior in the helical phase directly to the linear behavior of the conical phase before transitional to the field polarized state. The DCM measurements show very similar features: the signal starts out with an increase to a positive frequency shift in the helical phase before it exhibits a sharp drop to a negative frequency shift in the skyrmion phase. Then it jumps back up to a positive value when the magnetization switches back to a conical phase. From there it transforms smoothly to a negative value before it shows a kink where the cones close and it transitions to the field polarized state. The values of the transition fields are comparable, however need to be corrected due to different anisotropies or crystal directions.

The imaginary part of the susceptibility exhibits some features around the transition in and out the skyrmion phase, indicating dissipative features and hence magnetic fluctuations in these regions, typical for magnetic phase transitions. Features like this can be observed in the dissipation signal Γ (not shown here) and in fact, Γ can be used to investigate phase transitions (c.f. ch.(2.1.3)). This will be of relevance in ch.(5).

3 Magnetic Hysteresis of Individual Janus Particles with Hemispherical Exchange Biased Caps

3.1 Introduction

The previous chapters have introduced DCM as a sensitive method to measure anisotropic behavior and phase transitions in individual, nano- to micron sized magnetic particles. Such particles have become of interest not only in fundamental sciences, but they also offer attractive applications for example in biomedicine [90] or spintronics [91]. In order to obtain a controllable behavior of magnetic particles via magnetic fields, the possibility to engineer their anisotropic properties is a necessity. One way to do this, is by making use of an effect called exchange bias [92–94], which arises due to the interaction of a ferromagnetic and an antiferromagnetic material and manifests itself in form of an artificial, unidirectional anisotropy. By changing the growth parameters and system properties, strength and direction of this anisotropy can be engineered. As a subgroup of micron and sub-micron sized magnetic particles, which are discussed as a multi-functional component in lab-on-chip or micro-total analysis systems [2, 3], magnetic JPs, consisting of a hemispherical cap of magnetic material on a non-magnetic spherical template, allow not only a controlled transversal motion, but also a controlled rotation by rotating external magnetic fields [4, 5]. Such JPs can be mass-produced via the deposition of magnetic layers on an ensemble of silica spheres. The transversal and rotary motion of these particles can be controlled via external magnetic fields, which exert magnetic forces and torques [6]. This ability to externally actuate magnetic JPs has led to applications in microfluidics, e.g. as stirring devices [7], as microprobes for viscosity changes [8], or as cargo transporters in lab-on-chip devices [9–11]. Magnetic JPs have also been proposed as an *in vivo* drug delivery system [12]. Although, in general, a transversal controlled motion can be achieved by both superparamagnetic particles or particles with a permanent magnetic moment, a control over the rotational degrees of freedom can only be achieved, if the particles possess a sufficiently large permanent magnetic moment. Streubel et al. [95] analyzed the remanent magnetic state of magnetic JPs with ferromagnetic (fm) magnetic caps. Their simulations show that permalloy JPs with diameters larger than 140 nm host a global vortex state at remanence. Because this flux-closed state has a vanishing net magnetic moment, magnetic JPs hosting such a remanent configuration are unsuited for applications involving magnetic actuation. Thus, for JPs larger than this critical diameter, strategies to overcome this limitation need to be developed.

Here, we apply an exchange bias to the fm layer by adding an antiferromagnetic (afm) layer beneath the fm layer of the magnetic cap, which is able to prevent the formation of a global vortex at remanence. In order to verify that this addition leads to a remanent configuration with large magnetic moment, we measure the magnetic hysteresis of individual JPs with and without this layer.

This chapter first gives a brief overview and an intuitive picture of the phenomenology of exchange bias, and subsequently presents the results on the measurements of the magnetic JPs, which are adapted from the following work:

Magnetic hysteresis of individual Janus particles with hemispherical exchange biased caps

Cite as: Appl. Phys. Lett. **119**, 222406 (2021); doi: 10.1063/5.0076116
Submitted: 21 October 2021 · Accepted: 16 November 2021 ·
Published Online: 3 December 2021



S. Philipp,¹  B. Gross,¹  M. Reginka,²  M. Merkel,²  M. M. Claus,¹  M. Sulliger,¹  A. Ehresmann,² 
and M. Poggio^{1,3,a)} 

3.2 Exchange bias as unidirectional anisotropy

When a system in which a layer of ferromagnetic material has an interface with an antiferromagnetic material is field-cooled through the Néel temperature T_N of the antiferromagnet, the two layers interact via the exchange interaction between the spins of the two materials at the interface, and an anisotropy is induced. This effect was first discovered in 1956 by Meiklejohn and Bean and is called exchange bias [92–94]. Though studied in a multitude of different systems [96–98] since its discovery, a clear understanding of exchange bias at a microscopic level is still lacking [93, 99].

Phenomenologically the effects of exchange bias on the hysteresis curve of the magnetic system are apparent mainly through a shift along the field axis by an amount $H_{eb} = (H_{c2} - H_{c1})/2$ called the exchange bias field and a superimposed broadening of the curve. H_{c1} and H_{c2} are the coercive fields. In addition, upon multiple loops through the curves, the magnetic state at the initial field value will change as a function of how many times the hysteresis loop is cycled. The effect results in a reduced saturation magnetization and is called training [100, 101]. The decreased curvature of the loop on the ascending branch of the hysteresis can be attributed to the fact that the field is pointing along the exchange bias direction and thus the switching rates of the magnetic moments is enhanced, causing it to rotate earlier as compared to a fully ferromagnetic system. The magnitude of this, like all exchange bias related effects, is typically dependent on several system parameters such as the thickness of the involved layers, the geometry of the magnet, anisotropies and the exchange strength of the materials. Fig.(3.1) (a) summarizes the effects in a schematic of an exchange-biased hysteresis loop.

Fig.(3.1) (b) displays an intuitive picture of how the shift of the hysteresis loop is generated. (1) Before field cooling through T_N with $T_N < T < T_c$, the spins in the AFM are not ordered, whereas the FM is already point along the field. (2) After field cooling, the FM is still saturated but the AFM is in an ordered, antiferromagnetic state. The exchange bias direction is now aligned with the ferromagnet's magnetic moments. One can imagine that the FM is used to imprint the exchange bias direction in the AFM. (3) if the field direction is inverted, the FM moments start to turn towards the external field, but are held back by the exchange interaction with the AFM spins that now points antiparallel with the exchange bias direction, before they subsequently switch (4) and saturate in the opposite direction. Note, that the AFM spins still point in the same direction as in the beginning. (5) Increasing the field and reversing the field direction again to the original direction, the exchange interaction is again parallel to the

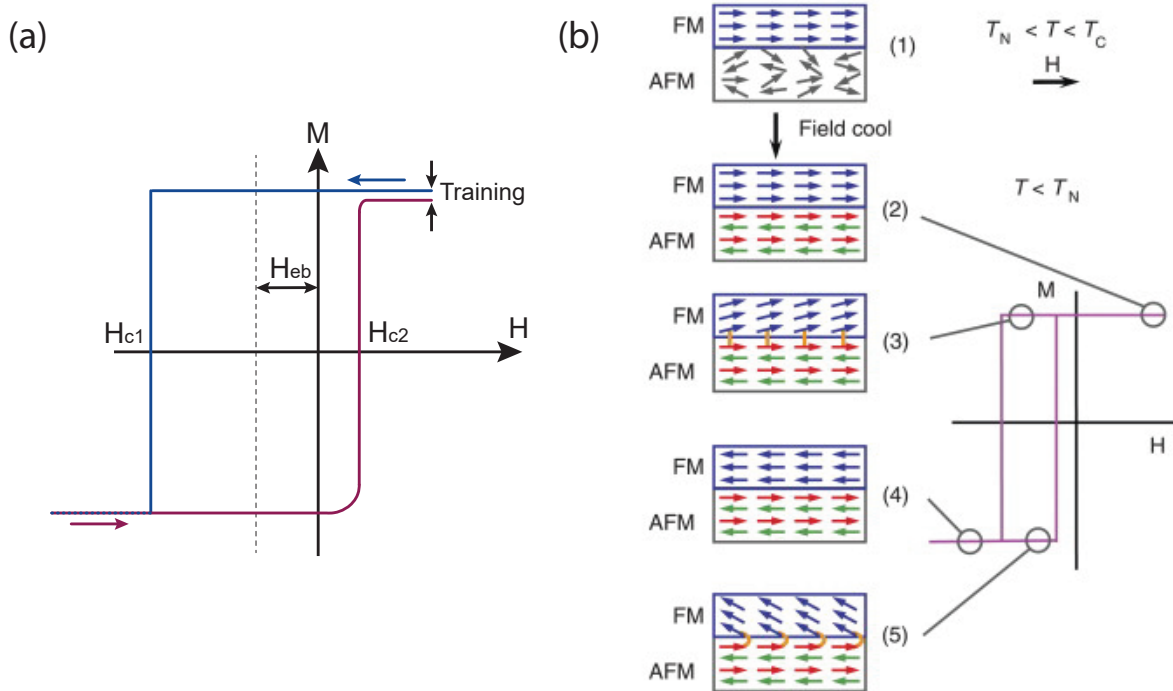


Figure 3.1 | (a) Schematic of a hysteresis loop of an exchange-biased magnetic system. The main features are a shift along the magnetic field axis by an amount $H_{eb} = (H_{c2} - H_{c1})/2$, which is called exchange-bias field. H_{c1} and H_{c2} are the coercive fields. On the increasing branch of the hysteresis, the curvature of the loop is decreased due to alignment of the external field with the exchange bias direction. The difference of the magnetic state at positive saturation is called training. (b) Intuitive picture of how the shift along the Field axis is generated. Picture adapted from [93]

external field and thus the switching process happens at much lower field values compared to a purely ferromagnetic system. The belated switching on the descending branch and the early switching in the ascending branch ultimately cause the shift in the hysteresis loop.

Micromagnetic simulations that account for local dependence of the magnetization and mimic the interaction between two materials have been done by De Clerc *et al* [102] in MuMax³. Their approach includes two layers of materials, given by two different mesh regions. The “antiferromagnetic” layer is discretized using a Voronoi tessellation with a given number of cell seeds. Each Voronoi cell includes a number of mesh cells. Subsequently, the Voronoi cells are divided into two classes of rotatable and pinned magnetizations, with a given ratio. Both types have their own uniaxial anisotropy constant, given by K_{rot} and K_{pin} , and their anisotropy axes are randomly distributed in the \mathbf{xy} -plane. The pinned grains cause an unidirectional shift of the hysteresis loop while the rotatable grains lead to a small enhanced coercivity [103] and are able to produce the athermal training effect [102]. Relaxing the energy, the “ferromagnetic” layer in the simulation is subject to the exchange interaction with the pinned cells, which reproduces the exchange bias. This procedure applies well to systems that can be discretized using finite difference methods with a cubic mesh. For systems that require finite element methods and a discretization using a tetrahedral mesh or an analytical approach such as the Stoner-Wohlfarth model, the method reaches its limit in applicability.

In order to reproduce the effects of exchange bias for a DCM measurement, we rely on a simplified model where we introduce the preferred direction that is imposed to the magnetiza-

tion by the exchange bias in form of a unidirectional anisotropy with anisotropy constant K_{eb} . This method applies in the SW framework as well as in micromagnetic simulations and works as follows:

We introduce a vector \mathbf{u}_{eb} along the exchange bias direction using a set of spherical coordinates $\{\theta_{eb}, \phi_{eb}\}$. The corresponding energy then reads

$$E_{ud} = -K_{eb}V (\mathbf{m} \cdot \mathbf{u}_{eb}) \quad (3.1)$$

We follow the procedure introduced in chapters (2.2.1)-(2.3.1) to calculate the high field frequency shift that occurs due to this additional energy term.

$$\begin{aligned} \Delta f_{ud} = & -\frac{f_0 V K_{eb}}{2k_0 l_e^2} \cdot \left(\cos \theta_u (\sin(\theta_h) \sin(\theta_{eb}) \cos(\varphi_u) \cos(\varphi_{eb}) + \cos(\theta_h) \cos(\theta_{eb})) \right. \\ & - \sin(\theta_{eb}) (\sin(\theta_u) \cos(\theta_h) \cos(\varphi_{eb}) + \sin(\theta_h) \sin(\varphi_u) \sin(\varphi_{eb})) \\ & \left. + \sin(\theta_u) \sin(\theta_h) \cos(\theta_{eb}) \cos(\varphi_u) \right) \end{aligned} \quad (3.2)$$

Here, $(\theta_h, \varphi_h = 0)$ define the orientation of the external field, (θ_u, φ_u) of the axis of the uniaxial shape anisotropy as defined in Ref. [79], and $(\theta_{eb}, \varphi_{eb})$ of the unidirectional anisotropy vector. The latter is oriented first, and rotated by (θ_u, φ_u) in a second step to be consistent with the situation in experiment. Cantilever and magnetic parameters are as defined before.

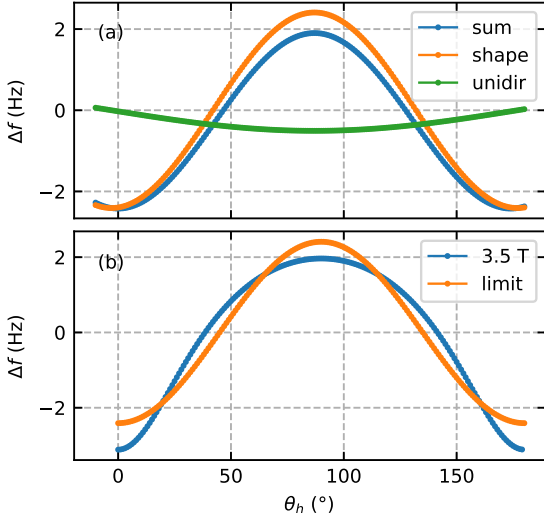


Figure 3.2 | (a) $\Delta f(\theta_h)$ in the high field limit with shape and unidirectional anisotropy. $\Delta f(\theta_h)$ in the SW model for 3.5 T applied field magnitude, and in the high field limit from (a).

possible in our experiment. This allows to compare the result of the SW model with the high field limit as discussed above, see Fig.(3.2) (b). The curve of the high field limit follows a (negative) cosine with $2\theta_h$ in the argument. In turn, for the SW model at 3.5 T, minima are deeper and maxima are shallower in Δf , respectively. However, there is no deviation from

We evaluate the high-field limit for the sum of shape and unidirectional anisotropy. However, we increase K_{eb} significantly to magnify its effects. The angles are set to be $(\theta_u, \phi_u) = (-3^\circ, 0^\circ)$ and $(\theta_{eb}, \phi_{eb}) = (-90^\circ, 0^\circ)$, while θ_h is varied as in experiment. The result is shown in Fig.(3.2) (a), together with the individual contributions from shape and unidirectional anisotropy.

This shows, that the sum of the two contributions may lead to a periodicity that deviates slightly from 180° , which would be given for pure uniaxial shape anisotropy. Furthermore, the magnitude of maxima and minima may differ significantly. Here we find 1.9 Hz for the maxima and 2.4 Hz for the minima, respectively.

The SW model, as described in ch.(2.2.2), can be used to calculate $\Delta f(\theta_h)$ for a fixed field magnitude. We set this field value to 3.5 T, in order to be consistent with values

the 180° periodicity. Further, maxima are wider than minima when the high field limit is not fully reached, which is a consequence of the fact that positive and negative asymptotes are approached with a different curvature when ramping up the external field in the SW model. This can be seen in Fig.(2.3) for both easy axis and easy plane curves.

3.3 Samples and Cantilevers

The magnetic JPs are fabricated by coating a self-assembled template of $1.5\ \mu\text{m}$ -sized silica spheres with thin layers of different materials via sputter-deposition in the group of Prof. A. Ehresmann at the University of Kassel. The non-magnetic silica spheres are arranged on a silica substrate using entropy minimization [104], which allows the formation of hexagonal close-packed monolayers. JPs with two different layer stacks, shown in Fig.(3.3) (b), are produced.

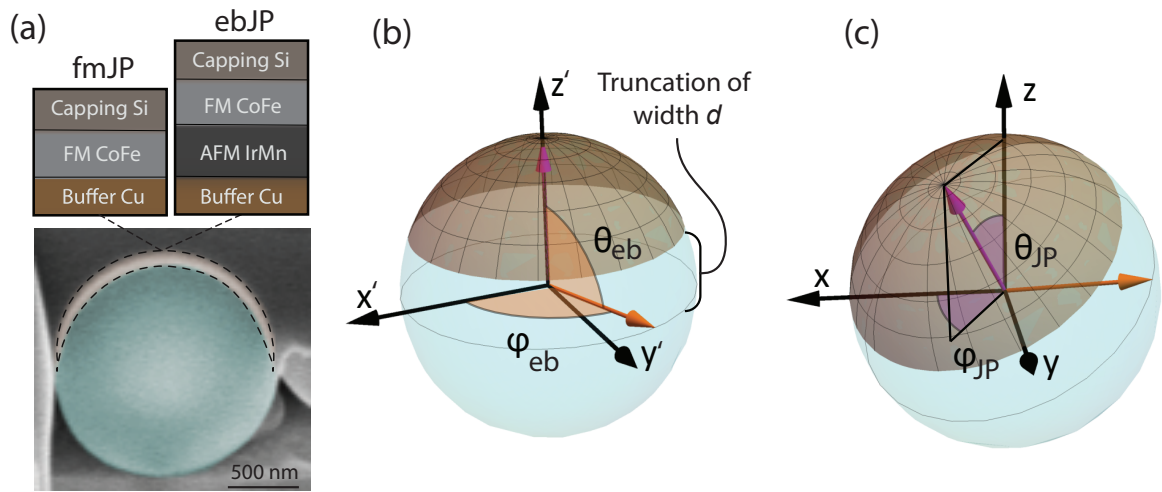


Figure 3.3 | (a) Cross-sectional SEM of a JP showing the gradient of the layer thickness. The two investigated layer stacks of the hemispherical cap are shown in the insets. (b), (c) Definition of the angles setting the orientation of the unidirectional anisotropy vector used to mimic exchange bias effects (θ_{eb} , φ_{eb}), and the angles defining the orientation of a JP on the cantilever (θ_{JP} and φ_{JP}).

Ferromagnetic JPs (fmJPs) are fabricated by depositing a 10 nm-thick Cu buffer layer directly on the silica spheres, followed by a 10 nm-thick layer of ferromagnetic CoFe. The film is sealed by a final 10 nm-thick layer of Si. A second type of JP, which we denote exchange-bias JPs (ebJPs), includes an additional 30 nm-thick afm layer of $\text{Ir}_{17}\text{Mn}_{83}$ between the Cu buffer and the fm layer. Layer deposition is performed by sputtering in an external magnetic field of 28 kA/m applied in the substrate plane, i.e. in the equatorial plane of the JPs, in order to initialize the exchange bias by field growth. This fabrication process is described in detail in Tomita et al. [105]. Individual JPs are then attached to the apex of a cantilever for magnetic characterization in a last fabrication step, as shown in the scanning electron micrographs (SEMs) of Fig.(3.4) (a) and (b). This was done using the hydraulic micromanipulator system. Note that the values given for thicknesses are nominal and that the film thickness gradually reduces towards the equator of the sphere with respect to the top, as shown in Fig.(3.3) (b), because of the deposition process [105]. Furthermore, the touching points of the next neighbors in the hexagonal closed packed arrangement of the silica spheres on the substrate template

Sample	f_0 [Hz]	k_0 [$\mu\text{N/m}$]	l_e [μm]
fmJP	5285.8	249	75.9
ebJP	5739.3	240	75.9

Table 3.1 | Properties of the cantilevers used for each the fmJP and ebJP.

impose a lateral irregularity on the equatorial line of the capping layers. This is best seen in Fig.(3.4) (a) and (b).

The cantilevers used for this experiment are fabricated from undoped Si. They are 106 μm -long, 3.5 μm -wide, 0.1 μm -thick with a mass-loaded end and have a 11 μm -wide paddle for optical position detection. The resonance frequency f_0 of the fundamental mechanical mode used for DCM is on the scale of a few kilohertz. Spring constant k_0 and effective length l_e are determined using a finite element approximation [106]. The mechanics and behavior of these types of cantilevers is described in detail in [42–44]. The properties of the cantilevers used here are given in table (3.1)

3.4 Results and Discussion

3.4.1 Measurements

After attaching the particles to the cantilevers, we first measure Δf_{hf} as a function of θ_h , as described in ch.(2.2.2). Fig.(3.4) (a) and (b) shows false color SEMs of the measured fmJP and ebJP, respectively, each attached to the tip of a cantilever. The orientation of the particles in the imaticges can be correlated with the angle θ_h of the maxima and minima found in the high-field frequency shift $\Delta f_{hf}(\theta_h)$ in dependence of the magnetic field angle θ_h , shown in Fig.(3.4) (c). Doing so, we find a magnetic easy direction in the equatorial plane of the particles and a hard direction along the axis of the pole. The 90° angle between easy and hard direction is a clear indication that uniaxial anisotropy is the dominant anisotropy in the system. We ascribe the latter to the shape of the JPs, because no other strong anisotropies are expected.

The field-dependent frequency shift $\Delta f(H)$ for \mathbf{H} aligned along the easy axis, see Fig.(3.4) (d), shows the typical hysteretic, V-shaped curve, that approaches a horizontal asymptote for high field magnitudes. The fmJP shows a symmetric asymptotic behavior for $\mu_0 H = 3.5 \text{ T}$ and -3.5 T (blue curve). Magnetic reversal at low fields, $\mu_0 H$ around $\pm 20 \text{ mT}$, is symmetric upon reversal of the field sweep direction, as shown in Fig.(3.4) (e). This behavior is expected for a ferromagnetic particle with a magnetic field applied along its easy axis. In contrast, measurements of the ebJP reveal asymmetric asymptotic behavior with Δf_{hf} values differing by about 0.9 Hz for $\mu_0 H = \pm 3.5 \text{ T}$, as seen in the brown curve of Fig.(3.4) (d). Furthermore, after a full hysteresis cycle, we observe a reduction in the difference of Δf_{hf} at $\pm 3.5 \text{ T}$ by about 0.4 Hz, which is evidence for magnetic training. Measurements of the ebJP also show a highly asymmetric magnetic reversal, which occurs at $\mu_0 H = -44 \text{ mT}$ when sweeping the field down and at $\mu_0 H = 12 \text{ mT}$ when sweeping the field up. All of these findings are characteristic of an exchange bias imposed on the fm layer by the afm layer and reflects the behavior of the hysteresis loop described in ch.(3.2).

The field dependent frequency shift was measured for both fmJP and ebJP each in the easy and hard orientation. Before we proceed to analyze these data in detail, we introduce the micromagnetic model that we established to reconstruct the frequency shift data.

3.4.2 Micromagnetic simulations

3.4.2.1 Modelling the DCM curves

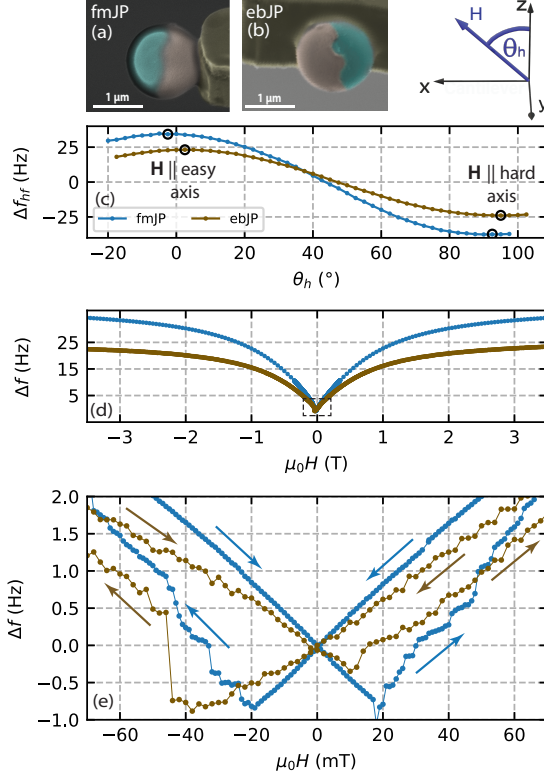


Figure 3.4 | False color SEMs of the (a) fmJP and (b) ebJP attached to the tip of a cantilever, respectively. The coordinate system is shown on the right. (c) $\Delta f_{hf}(\theta_h)$ measured at $\mu_0 H = 3.5$ T for the fmJP (blue) and ebJP (brown). Black circles indicate θ_h of the hysteresis measurements, which are shown in (d), (e), and Fig.(3.9).

respect to the cantilever rotation axis and \mathbf{H} is set by inferring the orientation from the SEMs and followed by an iterative tuning of the angles $(\theta_{JP}, \varphi_{JP})$, as defined in Fig.(3.3) (d), to match the measured $\Delta f(H)$. The exchange constant is set to $A_{ex} = 30$ pJ/m [108].

In case of the fmJP, opposing to the SEM image in Fig.(3.4) (a) which suggests a truncation of the fm layer by about 250 nm, it needs to be set to 350 nm or even more to match the high field progression of $\Delta f(H)$. For the same reason the nominal thickness of 10 nm of the fm layer needs to be increased to at least 12 nm at the pole, which is then gradually reduced to 0 at the equator. These two geometric constraints are necessary to keep M_s at a reasonable value below the bulk value of 1.95 MA/m [109]. This suggests, that significantly more fm material than anticipated is deposited on the region around the pole of the JPs, which is the most directly exposed area of the sphere during deposition.

In order to draw conclusions about the magnetic state of the JPs, we establish a micromagnetic model for each of the two types of JPs over many iterations of comparison to measured $\Delta f(H)$ and variations of the parameters for \mathbf{H} applied along the magnetic easy and hard axis, respectively. Due to the curved geometry of the samples, it is advantageous to use a finite-element approach to model the geometry of the magnetic cap in order to eliminate simulation errors due to a staircase effect along the surface, that would occur by using a cubic mesh in a finite-differences approach. The calculation of the frequency shift is according to the procedure established in ch.(2.2.3). The model assumes that the magnetic JPs are made from a hemispherical shell with a thickness gradient from the pole towards the equator, which accounts for the gradual reduction of the shell thickness away from the pole, as shown in Fig.(3.3) (b). The hemisphere is also truncated [107] by a latitudinal belt of width d around the equator, reflecting observations from the SEM images in Figs. 3.4 (a) and (b). For simplicity, in the simulations, we do not account for the magnetic film's irregular edge at the equator and a possible change in the crystallographic texturing with respect to the particle surface as a function of position within the cap. The orientation of a JP with

Sample	M_s [MA/m]	t [nm]	d [nm]	$(\theta_{JP}, \varphi_{JP})$ [°]	cs_{max} [nm]
fmJP	1.8	12	350	(91,2)	7.5
ebJP	1.44	10	350	(85,10)	7.0

Table 3.2 | Simulation parameters used for modelling of the fmJP and ebJP.

For the ebJP, we slightly adjust the geometrical parameters of the ferromagnetic layer and add the unidirectional anisotropy term given by eq.(3.1) to the total energy. We set the unidirectional anisotropy constant to $K_{eb} = 22.5 \text{ kJ/m}^3$ and the direction of the anisotropy is set by $(\theta_{eb}, \varphi_{eb}) = (-90^\circ, 0^\circ)$. This coincides with the external field when it is aligned with the easy direction of the particle and hence the effect of the exchange bias is maximized. K_{eb} thus sets a lower limit for this anisotropy constant. This adjustment is necessary, since the orientation of the exchange bias direction in the particle is unknown after the fabrication process, due to the physical movement of the particle from the substrate to the cantilever. The geometric parameters of the cap have to be adjusted less from their nominal values than for the fmJP, in order to match between the micromagnetic model to the experiment. This result suggests that the afm layer, which is deposited before the fm, acts as an adhesive for the fm, and the ebJP is coated more homogeneously than the fmJP. The common simulation parameters for each of the particles are given in table (3.2)

3.4.2.2 Shape anisotropy of a truncated spherical halfshell

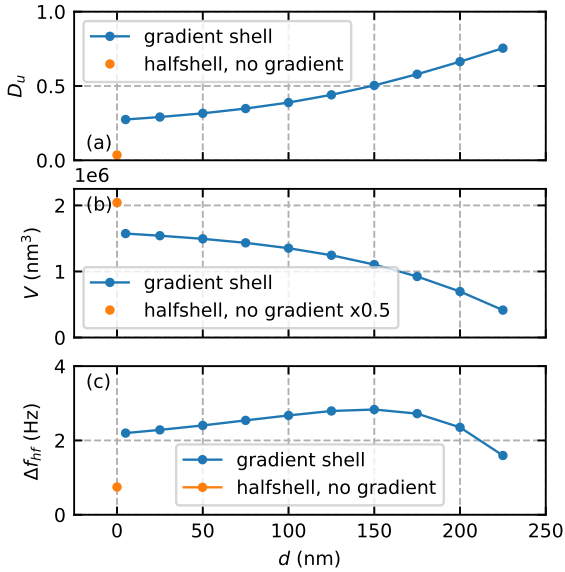


Figure 3.5 | (a) Effective demagnetization factor D_u of a truncated spherical halfshell with a gradient shell thickness in dependence of the truncation d (blue) and of a full halfshell (orange). (b) Volume and (c) high field frequency shift Δf_{HF} of the same geometries as in (a).

We assigned the uniaxial anisotropic behavior of the JP to the shape of the magnetic cap in the chapter above. In ch.(2.2.2), we introduced the uniaxial anisotropy with the aid of the demagnetization factor D_u as a measure of the strength of the shape anisotropy which we used as a parameter in the SW-model. As mentioned there, the exact calculation via an analytic model is only possible for a few specific geometries [110]. However, no such model is known for spherical caps and an intuitive understanding of the anisotropy strength as a function of the geometric parameters is more complicated than for other geometries like rectangles.

Using micromagnetic simulations as discussed above in ch.(3.4.2.1), we can extract a good approximation to the demagnetization factor of a given geometry, without necessity for an analytical formula by solving eq.(2.13) for D_u and inserting the simulation parameters. Here, we analyze a generic, truncated spherical halfshell as defined in section

(3.4.2.1) in order to gain some understanding of how D_u behaves as a function of d . We find a minimum D_u of approximately 0.25 for the smallest truncation, and D_u increases with trunca-

tion as shown in Fig.(3.5) (a). Hence, shape anisotropy gets stronger as d is increased, which can be roughly understood as the transformation from a spherical halfshell to a disc.

Note, that a spherical halfshell without thickness gradient and without truncation leads to a D_u just slightly larger than zero, comparable to a sphere of an isotropic material. This implies, that there is no drastically preferred direction for the magnetization, although there is a small preference if the field is aligned with the easy direction (compare the orange dots in Fig.(3.5)).

The high field frequency shift, Δf_{hf} , which is of relevance for extracting anisotropy constants from experiment [31, 79], first increases with truncation, but later decreases again, see Fig.(3.5) (c). This is owed to the loss of magnetic material for increasing truncation as seen in Fig.(3.5) (b).

3.4.3 Ferromagnetic Janus particles

$\Delta f(H)$, measured for \mathbf{H} parallel to the magnetic easy (blue data) and hard axis (orange data), respectively, are shown in Fig.(3.6) (a). We match the simulated frequency shift to the field dependent data over many iterations of fine tuning of the geometric parameters of the cap. For \mathbf{H} parallel to the magnetic easy axis, an overall V-shape suggest Stoner-Wohlfarth like behavior for most of the field range in Fig.(3.6) (a). As seen in the close-up in Fig.(3.6) (b), magnetic reversal appears to take place through a few sequential switching events at small negative reverse fields.

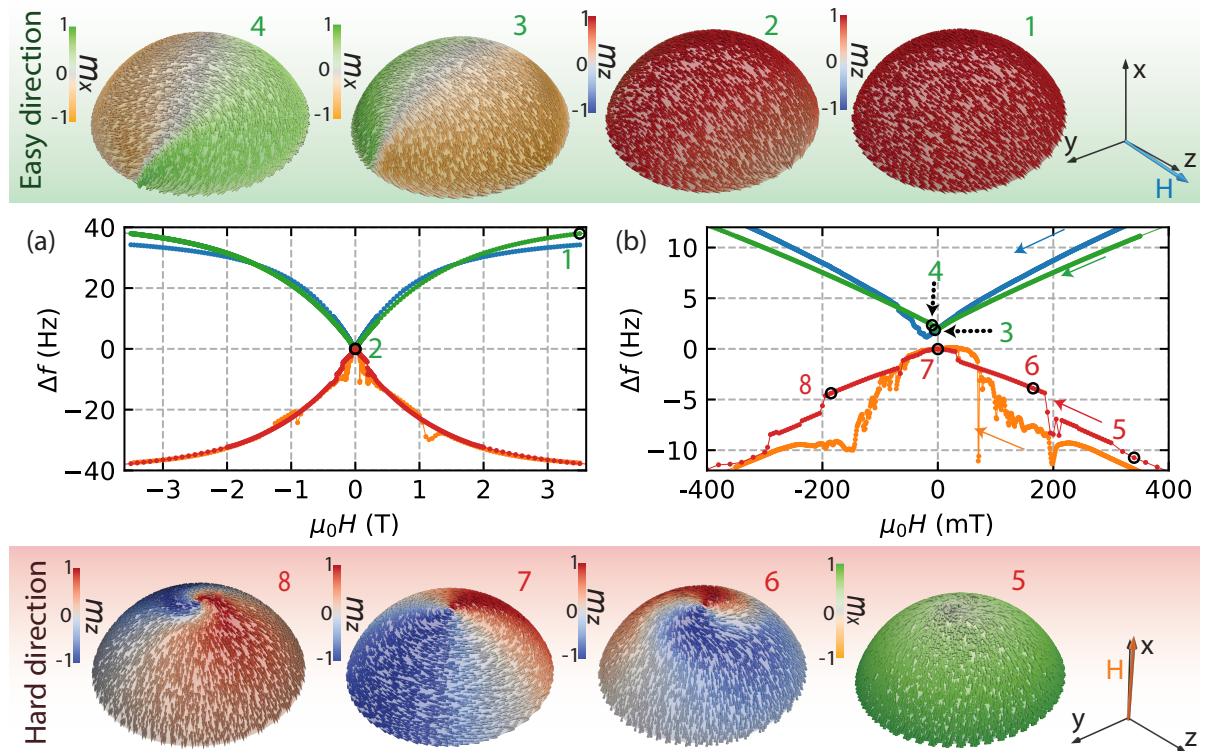


Figure 3.6 | Data for the ferromagnetic Janus particle. (a) Measured $\Delta f(H)$ for easy (blue) and hard (orange) alignment of the external field, as well as the simulated magnetic configurations in green (easy) and red (hard) orientation. (b) Close-up of (a) for low fields. Data with easy orientation is offset by 2 Hz for better visibility. Colored arrows indicate field sweep directions. Numbers in (a) and (b) denote the field values for the configurations of the magnetic state.

The simulated $\Delta f(H)$, also shown in Fig.(3.6) (green points) together with a few exemplary configurations of the simulated magnetic state of the JP, can give more insight into what happens during the field sweep. Starting from full saturation, most magnetic moments stay aligned with the easy direction down to very low reverse fields, nicely seen in Fig.(3.6), configuration 1 at 3.5 T and configuration 2 at remanence. The latter is an onion state. This progression of configurations is consistent with the Stoner-Wohlfarth-like behavior of the experimental $\Delta f(H)$. Magnetic reversal takes place through the occurrence of a so-called S-state, for which the magnetization follows the curvature of the letter S, which is known to appear in magnetic discs. The reversal is shown in configurations 3 and 4 in Fig.(3.6). Then, until full saturation is reached in reverse field, only magnetic moments in proximity to the equator of the JP are slightly canted away from the direction of the external field (and the easy plane). This progression is robust in simulation, even though sometimes, depending on slight variations of simulation parameters, a vortex appears in reverse field instead of the S-state. The observation of several, individual switching events during magnetic reversal in experiment may originate in vortex hopping, or switching of different regions in the JP due to variations in material and geometric parameters. Magnetic reversal through a vortex rather than an S-state may also explain the big difference of the coercive fields between experiment ($H_c \approx 32$ mT) and simulation ($H_c = 6$ mT).

For \mathbf{H} parallel to the magnetic hard axis, the experimental data has an inverted V-shape, and there is no easily identifiable sign of magnetic reversal. Yet, for relatively large fields, around 1.5 T, switching events that exist up to negative fields of similar magnitude are observed. This contradicts the W-shaped curves typically observed for measurements with the field aligned with the hard direction, that which can be explained within the SW-model discussed in ch.(2.2.2) of the theory section. The inverted V-shape can not be explained in the SW setting, but can be correctly reproduced by the simulations. To understand the reason for this behavior, the x component of the demagnetizing field H_{dm}^x within the magnetic layer is visualized for a cut through the geometry in Fig.(3.7) at high applied field in x direction. It shows a gradual change of the demagnetizing field magnitude with z position, which is a good measure of the preferred orientation of a magnetic moment.

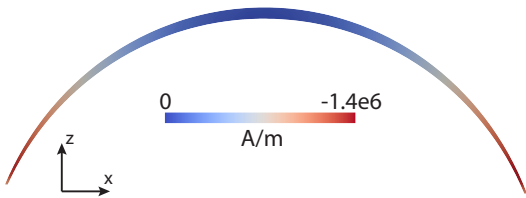


Figure 3.7 | Cut through the geometry of the JP at the position of the xz plane showing the x component of the demagnetizing field within the magnetic layer for $\mathbf{H} \parallel \hat{\mathbf{x}}$ and $\mu_0 H = 20$ T.

The magnetic moments in the top part with $H_{dm}^x \approx 0$ prefers the x orientation, whereas the bottom part with maximum H_{dm}^x needs a very high external field to be aligned in x direction. This shows, that magnetic moments in proximity to the pole need the smallest field magnitude to be aligned with a field in x direction. The required field magnitude gradually increases the closer a magnetic moment is situated to the equator. This explains the gradual change of Δf with increasing field in this orientation, opposing to what

is evident in the SW model, where all magnetic moments rotate in unison.

The angle between the local surface normal and the direction of the external magnetic field is different for every polar coordinate of the JP, which leads to a dependence of the local demagnetizing field on the polar coordinate. In consequence, the magnitude of the external magnetic field, for which the local magnetic moments start to rotate towards their local easy direction depends strongly on the position in the magnetic cap. This leads to the observed

curve shape of $\Delta f(H)$. The magnetic progression in simulation for external field alignment with the hard direction can be summarized as follows: Starting from full saturation, the magnetic moments start rotating towards the easy plane with decreasing field magnitude due to the competition between shape anisotropy and Zeeman energy. This takes place for different magnitudes of \mathbf{H} depending on where a magnetic moment is located in the JP, as discussed above. Configuration 5 in Fig.(3.6) shows a state for which magnetic moments at the pole have already started to rotate, while magnetic moments in proximity to the equator remain aligned with the external field. Superimposed to this rotation, a minimization of the system's energy by formation of a magnetic vortex localized at the pole for around 1.8 T takes place, which grows in size with decreasing field, see configuration 6. In simulation, this is a gradual evolution, and only for fields below about 300 mT jumps in Δf due to vortex movement are observed. This process is in contrast to the discontinuities that occur at around 1.5 T in the experiment, but can be explained by vortex hopping from pinning site to pinning site. The latter may be present due to fabrication inhomogeneities in the JPs [111]. For zero field the vortex dominates the magnetic configuration of the JP and has evolved into a global vortex state, as shown in configuration 7. Configuration 8 shows the vortex in reverse field, which has changed polarity, and has jumped to a slightly off-centered position. The latter is too small to be visible in the figure. Further decreasing the field, the vortex sits centrally in the JP and shrinks in size, and vanishes around -1.82 T. At the same time, the magnetic moments rotate towards the field direction depending on their position in the JP, as described earlier. Note, that by slightly changing simulation parameters, we find that features due to vortex entrance and hopping may manifest themselves in $\Delta f(H)$ with strongly differing magnitude and for different field values. Introducing artificial pinning sites in simulation can be used to adjust the vortex hopping to match the observed signals more precisely [111], but consumes vast amounts of computational time and should still be understood only as an exemplary progression of the magnetic state.

This analysis suggests that a remanent global vortex state, which has a vanishing total magnetic moment, is realized in fmJPs over time, independent of magnetic history. If we normalize the magnetic moment of this state by the saturation moment, $M_s V$, we find that the global vortex state hosted by the fmJP has a moment value of 0.03, precluding the use of such particles in applications.

3.4.4 Exchange biased Janus particles

The progression of the magnetic state for the ebJP is very similar to the fmJP, yet, there are crucial differences. See Fig.(3.8) for the DCM data, simulation results, and configurations of some magnetic states. For the field oriented in the magnetic easy direction the nearly polarized state, shown in Fig.(3.8) configuration 1, is similar to that shown in Fig.(3.6), configuration 1. Reducing the field down to remanence, as shown in Fig.(3.8) configuration 2, we find an onion state just as for the fmJP. Magnetic reversal occurs again through an S-state, rather than via vortex formation, as shown in configuration 3. However, the reversal is shifted towards negative fields, and occurs for -15 mT for the down sweep, and for -17.5 mT for the up sweep of the magnetic field. This does not match the experimentally observed values, especially for the latter case, for which the switching occurs for positive field. This is no surprise, since the employed model does not account for the contribution of the exchange bias to the coercivity. Yet, both simulation and experiment show a shift of the hysteresis loop towards negative fields as compared to the fmJP. We only observe a single switching event in experiment for the

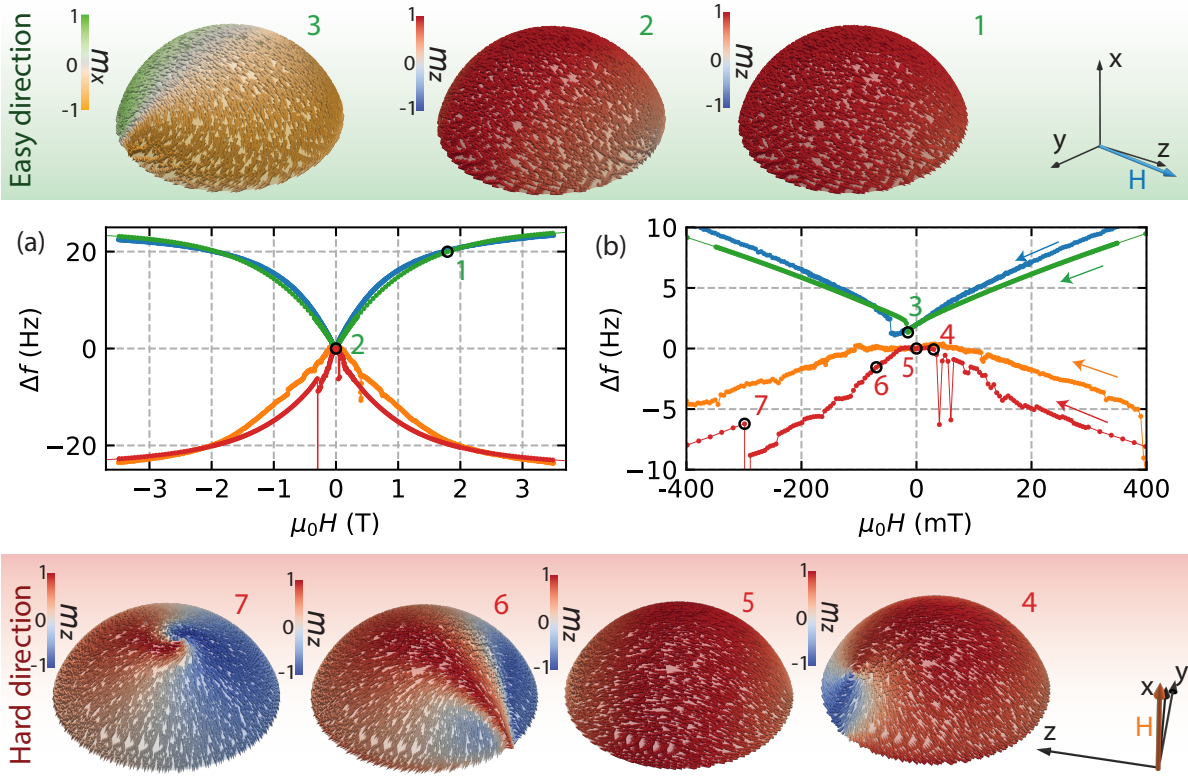


Figure 3.8 | Data for the exchange biased Janus particle. (a) Measured $\Delta f(H)$ for easy (blue) and hard (orange) alignment of the external field, as well as the simulated pendants in green (easy) and red (hard). (b) Close-up of (a) for low fields. Data with easy orientation is offset by 2 Hz for better visibility. Numbers in (a) and (b) indicate the field values for the configurations of the magnetic state shown in (c) for hard and in (d) for easy alignment.

magnetic reversal, which is consistent with the behavior of the S-state in simulation. For the alternative magnetic reversal process through vortex formation, we would expect several switching events due to vortex hopping. We find such a situation e.g. for a few reversal processes without unidirectional anisotropy, where geometrical parameters of the JPs have been varied, see appendix in [72]. Yet, it is also possible, that a strong pinning site favors the formation of a vortex, and keeps it in place for all field magnitudes up to the reversal point. If the magnetic field is swept from negative saturation up to remanence (not shown here), an onion state is present, that has its total magnetic moment pointing opposite to the exchange bias direction. For applications, this is an undesirable state. It is energetically less favorable than the state of parallel alignment, and if the energy barrier between the two states is overcome by an external influence, the JP will switch. Superimposed, a local vortex forms at the pole of the ebJP for an applied field of 1.34 T. As for the fmJP, the vortex occupies more and more volume of the JP with further decreasing field. However, upon further reducing the field, the vortex, rather than inhabiting the whole JP as a global vortex centered at the pole of the fmJP, it prefers to move to the side of the ebJP, as shown in configuration 4 of Fig.(3.8). Moving down from the pole towards the equator, the vortex exits from the JP through the equator for 5 mT, and an onion state is formed at remanence, as shown in configuration 5. The orientation of the onion state is governed by $\hat{\mathbf{u}}_{eb}$. For a small reverse field a domain wall state forms, as shown in configuration 6.

With further decreasing field, the domain wall is rotated with respect to the polar axis of the JP. This state seems to be a precursor of the vortex state, and the wall is subsequently replaced by the vortex, sitting again in the center of the JP, as shown in configuration 7. The vortex vanishes for -1.36 T. Whether such a domain wall state is indeed realized in the ebJPs for reverse fields, or if a vortex enters from the equator and moves back to the center of the JP, as seen for simulations of smaller JPs (see appendix in [72]), remains an open question. The DCM signal shows in both experiment and simulation many irregularities for the lower field range, which does not allow us to draw clear conclusions on the magnetic state present in the JPs. Nevertheless, the simulations clearly suggest that an onion state should be realized at remanence, irrespective of the states present during the hysteresis. This situation is markedly different than that of the fmJP and is a direct consequence of the presence of exchange bias.

For the simulations of the ebJP we find a total magnetic moment at remanence, normalized by its maximum value of $M_s V$, of 0.89 and 0.71 depending on whether \mathbf{H} is applied along the hard or easy direction of the external field, respectively. This remanent moment represents an increase of more than one order of magnitude compared to the remanent moment of the fmJP. Hence, introducing exchange bias to magnetic JPs, if strong enough, succeeds in stabilizing a high-moment onion state in remanence.

3.5 Summary and Conclusion

In this chapter we have introduced the concept of exchange bias as a uniaxial anisotropy. This can serve as a means for tuning the magnetic state of nanomagnets at remanence, a feature that allows for the use of such structures in technical or biomedical applications. This was done in the context of the investigation of magnetic Janus particles in the form of silica spheres capped with an antiferromagnetic/ferromagnetic or purely ferromagnetic thin film, which have been mass produced through a sputter-deposition process. The particles were attached to the cantilever and we have investigated the magnetic reversal and remanent magnetic configurations of individual specimens of these JPs using DCM and corresponding micromagnetic simulations. The simulations use an energy term that introduces a unidirectional anisotropy to the system

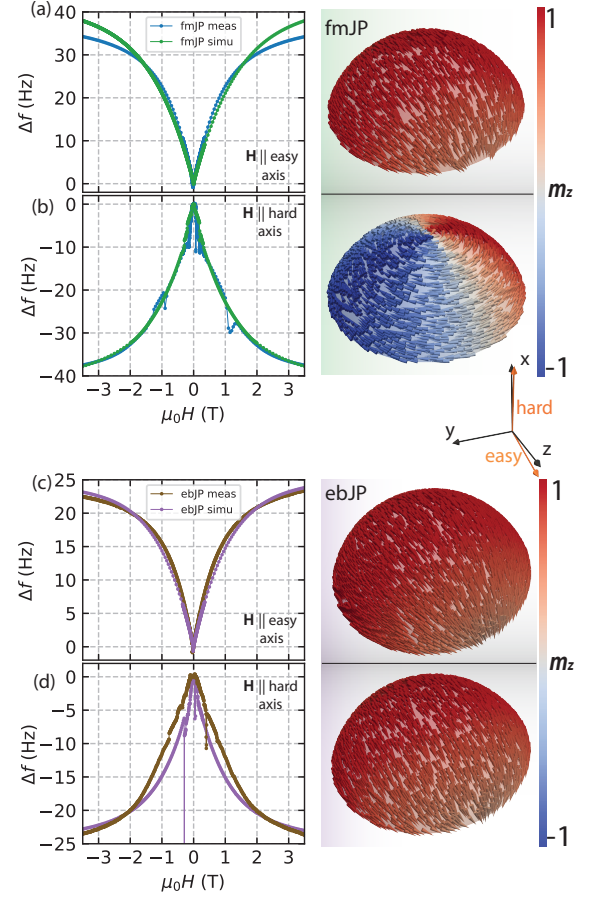


Figure 3.9 | Measured and simulated $\Delta f(H)$ of the fmJP for \mathbf{H} applied along the (a) easy and (b) hard axis, respectively. A visualization of each corresponding simulated remanent magnetic state is shown on the right. The same set of data for the ebJP is shown in (c) and (d).

and the simulated frequency shift could be matched with the data by fine tuning the geometric parameters and the direction as well as the strength of the exchange bias. In experiment, the knowledge about this direction is lost, and we set the direction such that the influence of the effect is maximized, and the unidirectional anisotropy constant $K_{eb} = 22.5 \text{ kJ/m}^3$ can be interpreted as a lower boundary of possible values. The simulations also allow to study the behavior of the uniaxial anisotropy constant D_u for a spherical cap, a geometry for which no analytic model exists to calculate a precise value for this property. Further analysis of generic Janus particles and how the exact geometric properties influence the curve shape and magnetic moment at remanence can be found in the appendix of [72]. We investigate the frequency shift both as a function of direction and magnitude of the external field, finding a clear indication of a uniaxial anisotropy with the hard direction pointing towards the pole of the cap. We also analyze the progression of the hysteresis curve and associate the switching behavior to different possible magnetic states, retrieved from the simulations. The results of this study are summarized in Fig.(3.9). Although the fmJPs host a global vortex state in remanence with a vanishing magnetic moment, the addition of an antiferromagnetic layer in ebJPs changes the remanent configuration to a stable high-moment onion state.

4 Magnetic Anisotropy of Individual Maghemite Mesocrystals

4.1 Introduction

Magnetic anisotropies can have several different contributions, each having their own origin within the investigated material. Crystalline anisotropies can contribute in a different way than shape anisotropy with the resulting effective anisotropy being the sum of each. In the chapter above, we have seen that artificially induced, e.g. a unidirectional anisotropy caused by an exchange bias, can be superimposed to the shape anisotropy of a magnetic material. Typically, in samples with a high aspect ratio such as nanowires or nanotubes [31], the uniaxial shape anisotropy is the dominant contribution. The situation changes, however, for more symmetrical samples, where the contribution of the crystalline anisotropy of the material is comparably stronger. This is the case for example in cubic nanoparticles, such as γ -Fe₂O₃ (maghemite) nanoparticles. These particles typically have sizes around a few nanometers to a few tens of nanometers per side, rendering them too small for most mechanical sensors to detect a magnetic signal from them.

However, maghemite nanoparticles can now be self-assembled into highly ordered three-dimensional (3D) superlattice structures up to micrometers in size, which allows for measurements using ultra-soft Si-cantilevers. The well-defined orientational order of the magnetic nanoparticles in the mesocrystal allows us to unambiguously identify the presence of cubic magnetic anisotropy, attributed to the crystal structure of the individual maghemite particles. In order to analyze our measurements, we use the model for the DCM response of a paramagnet developed in ch.(2.3.1). We find proof of superparamagnetic behavior down to a blocking temperature $T_b^{\text{spm}} = 133\text{ K}$ for three different mesocrystals. Furthermore, an exchange bias and frozen spin state below 90 K provide evidence for a disordered surface spin layer on the individual maghemite nanoparticles.

This chapter introduces the investigated mesocrystal samples and presents the results by closely following the corresponding publication:

PHYSICAL REVIEW B **103**, 014402 (2021)

Magnetic anisotropy of individual maghemite mesocrystals

B. Gross,¹ S. Philipp,¹ E. Josten², J. Leliaert³, E. Wetterskog,⁴ L. Bergström,⁵ and M. Poggio^{1,6}

¹Department of Physics, University of Basel, 4056 Basel, Switzerland

²Ernst Ruska-Centre for Microscopy and Spectroscopy with Electrons and Peter Grünberg Institute, Forschungszentrum Jülich, 52425 Jülich, Germany

³Department of Solid State Sciences, Ghent University, 9000 Ghent, Belgium

⁴Department of Engineering Sciences, Ångström Laboratory, Uppsala University, 75121 Uppsala, Sweden

⁵Department of Materials and Environmental Chemistry, Stockholm University, 10691 Stockholm, Sweden

⁶Swiss Nanoscience Institute, University of Basel, 4056 Basel, Switzerland

 (Received 9 November 2020; revised 15 December 2020; accepted 16 December 2020; published 4 January 2021)

4.2 Samples and Cantilevers

The ultrasensitive cantilevers we used here are of the same type as the one for the Janus Particles, described in the chapter above and differ only in the length, being only 90 μm -long. The rest of the properties remain the same, the cantilevers are 3.5 μm -wide and 0.1 μm -thick with a mass-loaded end and a 11 μm -wide paddle for optical detection. The resonance frequency f_0 of the fundamental mechanical mode used for magnetometry is between 5 and 6 kHz with k_0 and l_e 314 $\mu\text{N}/\text{m}$ and 74 μm , respectively. The mesocrystal samples are composed of nanopar-

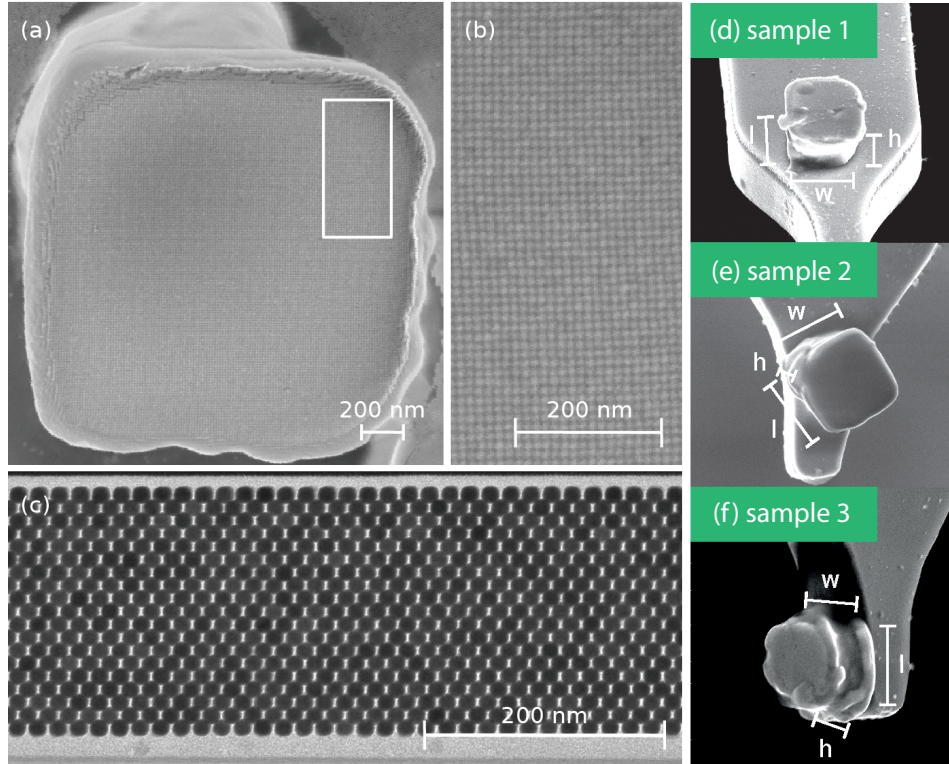


Figure 4.1 | (a) SEM image of a mesocrystal showing the superlattice structure from a top view. (b) Zoom of region shown in (a). (c) Cross-sectional TEM image viewed from the [100] direction of a thinned mesocrystal layer deposited on a Si single crystal, showing the BCT structure. Nanoparticles in the TEM image appear as dark circles. (d)-(f) SEM images of the investigated mesocrystals attached to cantilevers. The length $l \times$ width $w \times$ height h of the samples are determined from the images to be $1.95 \mu\text{m} \times 1.87 \mu\text{m} \times 1.58 \mu\text{m}$, $1.7 \mu\text{m} \times 1.89 \mu\text{m} \times 1.12 \mu\text{m}$, and $1.55 \mu\text{m} \times 1.54 \mu\text{m} \times 1.35 \mu\text{m}$, for samples 1, 2, and 3, respectively. h is defined to be along the [001] direction of the BCT crystal structure.

ticles, which are synthesized following a modified version of the metal oleate route [112, 113]. These particles consist of $\gamma\text{-Fe}_2\text{O}_3$ (maghemite) with less than 10% Fe_3O_4 (magnetite) content [114, 115]. The nanoparticles have an edge-length of 10.9 nm, their atomic structure shows a crystalline inverse spinel structure, and their morphology can be described by a rounded cube model [116]. The micron-sized mesocrystals, i.e. 3D superlattices of the maghemite nanocubes arranged with a high degree of both positional and orientational order, have been carefully grown using an optimized evaporation-driven self-assembly process [113, 116, 117]. Small angle X-ray diffraction performed on an individual mesocrystals reveals a body centered tetragonal (BCT) crystal lattice with an in-plane lattice constant $a = 13.47 \text{ nm}$, and an out-of-plane lattice constant $c = 15.08 \text{ nm}$ [116], cf. Fig.(4.1) (c) for a cross-sectional transmission electron

microscopy (TEM) image of a thinned mesocrystal layer showing the BCT structure. The self-assembly process for the mesocrystals is both size- and shape-selective [116, 117], i.e. the mesocrystals are composed of particles with a size dispersity which is drastically smaller than that in the initial dispersion [116]. Fig.(4.1) (a) and (b) show scanning electron microscopy (SEM) images of a typical mesocrystal.

4.3 Results and Discussion

4.3.1 Measurements

We investigate three different mesocrystals, which are each attached in different orientations to the end of a cantilever, as shown Fig.(4.1). The different orientations allow us to probe the anisotropy in different planes of the superlattice. The crystals have slightly different sizes, which we estimate from SEM images and list in the caption of Fig.(4.1).

We investigate the mesocrystals' magnetic anisotropy by measuring the high field frequency shift of the 3 samples as a function of θ_h for ($H = 3.5\text{T}$), at which the samples are near magnetic saturation. The bulk value of the saturation magnetization M_s is approximately $3 \times 10^5\text{A/m} = 0.38\text{T}/\mu_0$ [118]. In this case, we show $\Delta f_{hf}(\theta_h)$ in form of polar plots, which clearly show evidence of multi-axial anisotropy, most clearly in the case of sample 3. The measurements are displayed in Fig.(4.2).

We further investigate the full field dependence with the external field aligned with hard and easy orientation of the uniaxial anisotropy, as well as an intermediate angle in which the frequency shift is predominantly generated by a cubic anisotropy contribution. These measurements are displayed in Fig.(4.6). All DCM experiments are first carried out at $T = 270\text{K}$.

4.3.2 High-field Limit

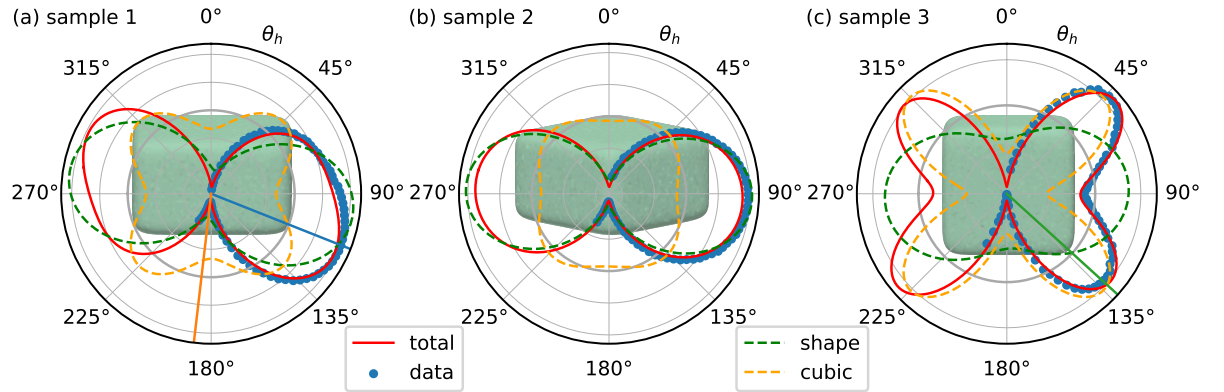


Figure 4.2 | Angular dependence of DCM in the high-field limit. (a)-(c) Polar plots of the high-field frequency shift $\Delta f(H = 3.5\text{T}/\mu_0, \theta_h)$ for sample 1 to 3 (blue dots) and corresponding fits (red, dashed green, and dashed orange lines). Straight, radial lines indicate the direction of the measurements and calculations in Fig.(4.6), according to the color code. Gray polar lines indicate Δf in steps of (a, b) 20 Hz and (c) 10 Hz, with a thick line for $\Delta f = 0$. In (a) a sketch of the mesocrystal is shown in the background to illustrate its orientation.

In order to fit the angle dependent high-field measurements shown in Fig.(4.2), we find that a sum of a uniaxial and a cubic anisotropy is required. In the following, we derive the required equations analogous to the case of a uniaxial anisotropy.

A material system can exhibit a cubic anisotropy term either because of the crystal symmetry or the shape of the crystal. For a system with a first order cubic anisotropy, we assume three anisotropy axes \mathbf{u}_i with $i = (1, 2, 3)$, with an effective anisotropy constant K_{c1} . The corresponding energy term looks as follows:

$$E_c = -VK_{c1} \left((\mathbf{m} \cdot \mathbf{u}_1)^2 (\mathbf{m} \cdot \mathbf{u}_2)^2 + (\mathbf{m} \cdot \mathbf{u}_2)^2 (\mathbf{m} \cdot \mathbf{u}_3)^2 + (\mathbf{m} \cdot \mathbf{u}_3)^2 (\mathbf{m} \cdot \mathbf{u}_1)^2 \right) \quad (4.1)$$

In general, the coordinate system given by the anisotropy axes is linked to the sample geometry. In the special case where it coincides with the coordinate system of the cantilever, as is given for samples 1 and 2, it can simply be described by the magnetization components and reduces to

$$E_c = -VK_{c1} \left(m_x^2 m_y^2 + m_y^2 m_z^2 + m_z^2 m_x^2 \right) \quad (4.2)$$

For any other orientation, it can be described by a simple coordinate transformation for the \mathbf{u}_i . The full magnetic energy term used here is

$$\begin{aligned} E_m = & -\mu_0 V M_s H_0 \mathbf{m} \cdot \mathbf{h} \\ & - K_{u1} V (\mathbf{m} \cdot \mathbf{n})^2 \\ & - VK_{c1} \left((\mathbf{m} \cdot \mathbf{u}_1)^2 (\mathbf{m} \cdot \mathbf{u}_2)^2 \right. \\ & + (\mathbf{m} \cdot \mathbf{u}_2)^2 (\mathbf{m} \cdot \mathbf{u}_3)^2 \\ & \left. + (\mathbf{m} \cdot \mathbf{u}_3)^2 (\mathbf{m} \cdot \mathbf{u}_1)^2 \right) \end{aligned} \quad (4.3)$$

Following the derivation in ch.(2.2.2.1), we apply a rotation matrix around the \mathbf{y} -axis on the \mathbf{u}_i as given in eq.(4.1) and calculate Δf_{hf}^{tot} . In addition, we assume that the particle has uniaxial shape anisotropy with \mathbf{n} aligned along the \mathbf{x} -axis and that \mathbf{u}_3 coincides with the \mathbf{z} -axis. We allow \mathbf{u}_1 and \mathbf{u}_2 to lie freely in the \mathbf{xy} -plane, independent of the direction of \mathbf{n} , as would for example be the case of a ferromagnetic material with cubic crystal anisotropy, which is shaped in a prolate ellipsoid at some angle between the \mathbf{u}_1 and \mathbf{u}_2 axes. To do so, we introduce a set of spherical coordinates (θ_u, φ_u) in order to describe \mathbf{u}_1 with respect to the main coordinate system given in Fig.(2.1) and keep $\theta_u = \pi/2$ all the time, while φ_u is arbitrary. From this, we obtain \mathbf{u}_2 by applying a rotation by $\pi/2$ around the \mathbf{z} -axis on \mathbf{u}_1 . The high-field frequency shift Δf_{hf}^{tot} now consists of the sum of the contributions from the uniaxial anisotropy and the cubic anisotropy. The uniaxial contribution Δf_{hf}^u is unchanged and given by eq.(2.13). The cubic contribution f_{hf}^c reads as follows:

$$\Delta f_{hf}^c = \frac{f_0 K_{c1} V}{8k_0 l_e^2} (\cos(2\theta_h) + 7\cos(4\theta_h) - 2(1 + 2\cos(2\theta_h))\cos(\varphi_u)\sin^2(\theta_h)) \quad (4.4)$$

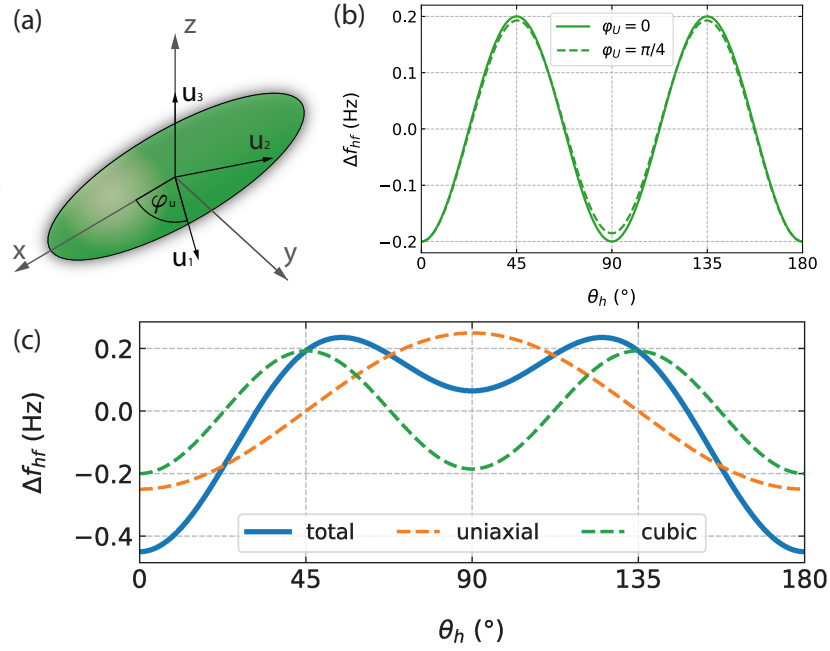


Figure 4.3 | (a) Orientation of the cubic coordinate system given by the axes \mathbf{u}_i , $i = \{1,2,3\}$ in the SW particle with respect to the main coordinate system. The rotation of the system is parametrized by the angle φ_u . (b) Δf_{hf}^c for $\varphi_u = 0$ (blue curve) and $\varphi_u = \pi/2$ (orange curve). As can be seen in eq.(4.4), the amplitude of the signal is modified by the cosine of the rotation angle φ_u . (c) High-field frequency shift for a SW particle with cubic anisotropy for $\varphi_u = \pi/4$. Dashed lines show the uniaxial (orange) and the cubic (green) contribution to the full frequency shift (blue).

The effect that a misalignment of the two coordinate systems has on the the frequency shift, becomes apparent through a modification of the amplitude of Δf_{hf}^c , as can be seen in Fig.(4.3) (b). For $\varphi_u = 0$ and other values that maximize the corresponding cosine in eq.(4.4), the signal has an unaltered sinusoidal behavior. For any other values, the amplitude is decreased periodically. Adding the uniaxial component to the signal yields the full frequency shift. We show an example curve calculated from the given model for $\varphi_u = \pi/4$ in Fig.(4.3) (c). The dashed lines show the uniaxial and cubic contributions, respectively, and the solid line the total frequency shift. Most notably, both cubic and uniaxial contributions naturally have zeros periodically. At these points, the frequency shift is generated fully by either one or the other contribution.

We use eqs.(2.2) and (4.4) as fit functions in order to analyze the data, with the K_i as fit parameters. A quantitative determination of K_{u1} and K_{c1} is not possible from these particular fits, since the magnetic fields of up to 4.5 T that are possible in our setup, are not strong enough to fully satisfy the high-field limit. We can, however, determine the relative weight of the two contributions to the anisotropy.

Since the mesocrystals consist of a large number of cubic particles, that interact with each other via the dipolar interaction, we expect the uniaxial contribution to be explicitly due to the overall shape of the mesocrystal, rather than due to the individual particles. Small deviations in the cubic shape of the nanoparticles average out due to their large number in the mesocrystal. In analogy to the shape anisotropy of a continuous magnetic solid, see ch.(2.2.2), the shape and lattice spacing of the mesocrystal determine this effective shape anisotropy. A

1D equivalent of such an effective anisotropy has previously been used to describe chains of iron oxide nanoparticles [119, 120].

A cubic component of the anisotropy may be present in the mesocrystals as a result of the cubic shape of the overall mesocrystal or of the individual maghemite nanoparticles [121], their crystalline anisotropy [122, 123], or their surface anisotropy, as suggested in Refs. [124–126]. The latter is calculated to be relevant only for particles with up to about 100 atoms per dimension, which is exceeded by our nanoparticles.

To quantify the influence of the exact lattice parameters and the shape of both nanoparticles and mesocrystal on the uniaxial and cubic anisotropy contribution, we use micromagnetic simulations in Mumax³.

Before investigating the mesocrystal structure, we analyze the symmetry and magnitude of the shape anisotropy of an individual maghemite nanoparticle by calculating $\Delta f(\theta_h)$ for a 11 nm cube. For these simulations, we use perfect cubes, so that the effect of the cubic shape anisotropy is maximized. The cube is discretized in cells with 0.2 nm edge length. To estimate the impact of a single cube's shape anisotropy on Δf of a full mesocrystal, we multiply with the approximate particle number $n \approx 2 \times 10^6$ in a mesocrystal.

The simulation results are shown in Fig.(4.4) (a) in blue. The symmetry of Δf is cubic, as expected, and the magnitude is below 0.5 Hz for $\mu_0 H = 3.5$ T. This is far too small to explain the observed magnitude of the cubic component of Δf (in the tens of Hz) in experiment. To contrast this result, we add a cubic crystalline anisotropy with $K_{c1} = -3 \text{ kJ/m}^3$ to the simulation and get a magnitude of Δf of around 25 Hz, which is on the scale of the experimental results. Note that the real particles are rounded cubes as compared to a perfectly shaped cube in the simulation, further reducing the cubic shape anisotropy. We will use this geometry in the simulation for the mesocrystal later on.

The same modeling procedure is carried out for a perfectly shaped $1 \times 1 \times 1 \mu\text{m}$ cube, in order to estimate the contribution of the mesocrystal's overall shape to the cubic component of the observed Δf . We use a cell size of 10 nm, which is well below the exchange length of 13.3 nm for the used material parameters, and have checked with 5 nm cells that the results are robust against a further reduction of the cell size. The simulation results are shown in

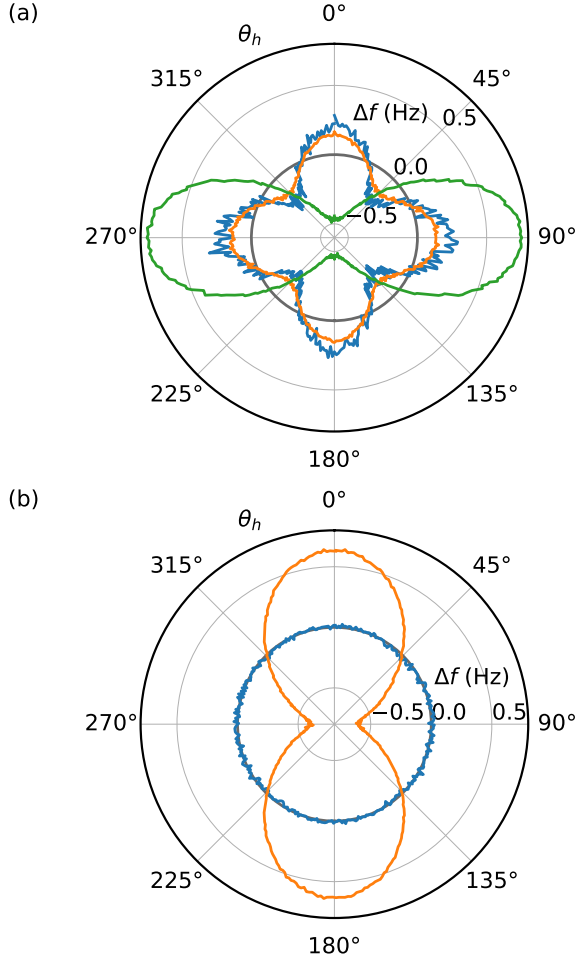


Figure 4.4 | (a) Simulated frequency shift of an individual nanoparticle of 11 nm side length multiplied by 2×10^6 (blue curve), a symmetric 1 μm sized cube (orange curve) and a slightly asymmetric 1 μm sized cube (green curve). (b) Simulated frequency shift of a BCT lattice of rounded nanocubes with lattice constants $a = c = 14$ nm (blue curve) and $a = 14$ nm, $c = 16$ nm (orange curve).

Fig.(4.4) (a) in orange. Again, the magnitude of this effect is too small to account for the observed magnitude of the cubic component of Δf . For comparison, we show the result for a slightly asymmetric cube ($1 \times 1 \times 0.99 \mu\text{m}$) in green. The small asymmetry already leads to a strong uniaxial component in Δf as compared to the cubic component.

We model the mesocrystal as BCT lattices of cubes with different lattice constants. To avoid uniaxial contributions to the shape anisotropy, resulting from elongation of the mesocrystal in one direction, we choose a cubic simulation volume of 112 nm on a side. The cubes themselves have a side length of 10 nm and rounded edges by intersecting with a 12 nm sphere. As mentioned before, we chose the rounded cube geometry of the nanoparticles in this case, in order to bring the simulations as close to the real experiment as possible. We use periodic boundary conditions in all directions with 4 repetitions on each side of the simulation volume, so that edge effects are negligible (half- and quartercubes sitting on the edges and corners of the simulation volume guarantee correct periodicity). In this way, each spatial dimension of the simulated mesocrystal is equally sized with approximately 1 μm length.

For the simulation of the mesocrystal, two sets of lattice constants are chosen. Set 1 is $a = c = 14 \text{ nm}$ and set 2 $a = 14 \text{ nm}$ and $c = 16 \text{ nm}$, where c points in z -direction in the coordinate system shown in Fig.(2.1). The calculated $\Delta f(\theta_h)$ for set 1, which is perfectly symmetric with respect to all three spatial dimensions, is shown as a blue curve in Fig.(4.4) (b). Δf is negligible in all directions compared to the value measured in our experiment. Set 2, for which the cubes have a slightly larger spacing in z -direction, shows an easy uniaxial anisotropy contribution in this direction. However, the magnitude of the effect is around 0.5 Hz, and hence small compared to the effect of elongations of the mesocrystal in one spatial direction.

The lattice constants of set 2 and their difference are very comparable with the values of the experimentally investigated samples ($a = 13.47 \text{ nm}$ and $c = 15.08 \text{ nm}$), and we thus expect a minor contribution of the superlattice structure on the shape anisotropy of the samples.

Our simulations show that the contribution from the cubic shape of the mesocrystals and the constituent nanoparticles are both at least one order of magnitude too small to account for the anisotropy observed in our DCM measurements. On the other hand, the crystalline contribution should appear in our measurements, due to the alignment of the individual nanoparticles with respect to each other. Indeed, in all three mesocrystal orientations shown in Fig.(4.2), both the uniaxial and the cubic components of the fitted curves match the expected orientation of the mesocrystal and its constituent crystalline nanoparticles. Furthermore, the magnitude of the uniaxial term is seen to scale with the overall shape of the mesocrystals: e.g. sample 3, the most symmetric mesocrystal (cf. caption of Fig.(4.1), shows a nearly vanishing uniaxial anisotropy. In conclusion, the results of the angle dependent measurements and analysis of the high-field limit suggest that the cubic component of the effective anisotropy is of crystalline type, measurable due to the perfect alignment of the cubic nanoparticles in the mesocrystal. The uniaxial part, in contrast, appears to be a result of the overall shape of the mesocrystal.

4.3.3 Full Field Dependence

In Fig.(4.6), we plot the field dependent measurements of $\Delta f(H)$ measured in samples 1 and 3, where the external field is swept between $H = \pm 3.5 \text{ T}$ for three orientations of θ_h . Most DCM curves show a V- or Λ -shape, depending on the orientation of the applied field. At low field, well below magnetic saturation, some curves present a W-shape, as seen in the inset. In this regime, $\Delta f(H)$ shows a small hysteresis with a coercive field of $\mu_0 H_c \approx 10 \text{ mT}$ for all

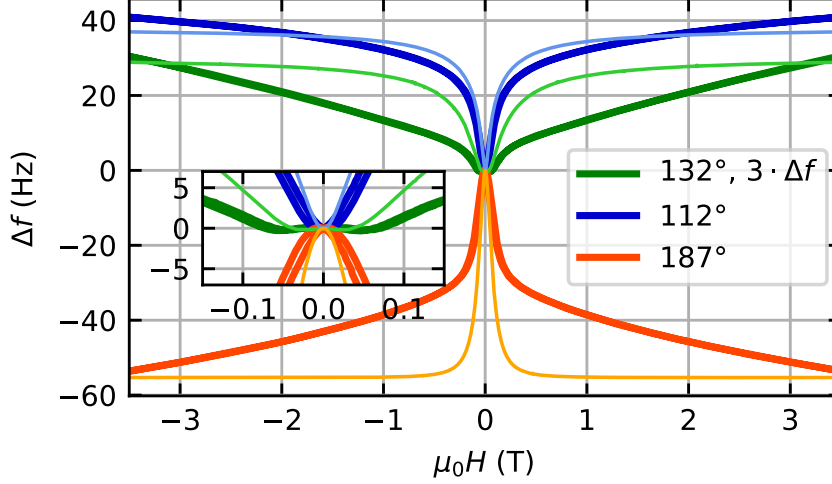


Figure 4.6 | DCM measurements at 270 K. Dark thick lines show measured $\Delta f(H)$ in sample 1 for orientations $\theta_h = 112^\circ, 187^\circ$ (blue and orange) and $\Delta f(H)$ in sample 3 for $\theta_h = 132^\circ$ (green). Light thin lines with similar coloring show the corresponding simulations according to a model for a thermally activated Stoner-Wohlfarth particle. The inset shows an enlargement around $H = 0$.

three mesocrystals. At high fields, the curves show an asymptotic behavior, associated with the external field along the hard or easy direction, as described in the chapters above.

In order to extract quantitative values for the uniaxial and cubic anisotropies and to understand the full field dependence of the measured $\Delta f(H)$ curves shown in Fig.(4.6), including the low-field regime, we rely on the model derived in ch.(2.3.1) for a thermally activated Stoner-Wohlfarth particle. This is necessary, since we expect the individual maghemite cubes of the given dimensions to be superparamagnetic at $T = 270$ K.

Even though the dipolar interaction between the nanoparticles alters the magnetic behavior of the system compared to individual superparamagnetic particles, resulting in a shifted blocking temperature, hysteresis, or even a suppression of superparamagnetism, the curves in Fig.(4.6) suggest that the mesocrystal is paramagnetic as well at the given temperature. For the model, we consider the given mesocrystals to consist of n interacting superparamagnets, where n is the number of nanoparticles in the mesocrystal lattice. Each obeys an effective Hamiltonian, which includes both uniaxial and cubic magnetic anisotropy terms.

Because we model the inter-particle interaction with an effective single particle term in the Hamiltonian, the model has limited validity, similar to approaches relying on mean-field Hamiltonians [127]. For the model fits shown in Fig.(4.6), we use a temperature of $T = 270$ K and a volume of the individual nanoparticles of $(9\text{nm})^3$. We use the same magnitude of $K_{c1} = -3.0\text{kJ/m}^3$ for all mesocrystals, since this term represents the crystalline anisotropy of the individual maghemite nanoparticles. This value is smaller than the -4.7kJ/m^3 of bulk $\gamma\text{-Fe}_2\text{O}_3$, perhaps due to interparticle interactions [128]. M_s is taken to be $3 \times 10^5\text{A/m}$ [118]. Fitting the data also yields $K_{u1} = 9.7, 20.8l$, and 2.1kJ/m^3 or $D_u = -0.17, -0.37$, and -0.04 in terms of the effective demagnetization factors for samples 1, 2, and 3, respectively.

The cantilever properties are $k_0 = 314\mu\text{N/m}$ and $l_e = 74\mu\text{m}$, and the angular oscillation amplitude is $\theta_c = 1.5^\circ$. n is estimated from the mesocrystal dimensions, as determined from SEM images and adjusted to match the measurements at high field. We find that $n = 1.87 \times 10^6, 0.83 \times 10^6$ and 1.67×10^6 works best in order to match the data. To account for the

expected presence of a disordered surface spin layer and to adequately fit the data, we model the individual maghemite particles to be slightly smaller, 9 rather than 10.9 nm on a side.

All of these values should be treated as approximate, given the simpleness of the model and the uncertainty (up to 20%) in precisely determining the magnetic volume of the mesocrystal samples. Calculated $\Delta f(H)$ curves are plotted along with measured $\Delta f(H)$ curves for the same field orientations in Fig.(4.6). The model adequately captures the overall features of the measurements, including V-, Λ -, and W-shapes. This agreement is evidence that the particles making up the mesocrystals are indeed in a superparamagnetic state at $T = 270$ K. Most notably, the Λ -shape is observed for a hard axis alignment of the external field (yellow curve) and is in strong contrast to the signature of a ferromagnet. The model also explains the occurrence of W-shaped curves: it is a consequence of the opposing sign of the cubic crystalline and the uniaxial shape anisotropy contributions for certain orientations of the external field, e.g. for $\theta_h \approx 135^\circ$, cf. Fig.(4.2) (c). A pure cubic system in this orientation leads to a relatively broad V-shape, while a pure uniaxial system leads to a relatively sharp Λ -shape with a small negative high-field asymptote. The presence of both anisotropies and their resultant competition produces a W-shaped curve. Despite this agreement, the model predicts high-field $\Delta f(H)$ asymptotes that saturate at lower field than in experiment, presumably as a consequence of the interactions between the particles, which we do not fully consider. Furthermore, in contrast to the experiments, the model does not predict hysteresis as a function of H . However, introducing strong interactions (e.g. with a mean field approach) or large anisotropies (increasing the anisotropy constants) to the model leads to ferromagnetic behavior, which includes hysteresis. We thus hypothesize that the observed hysteresis originates from the presence of the inter-particle interactions.

4.3.4 Behavior at low temperature

Temperature dependent measurements of the DCM response down to 5 K allow us to extract further information about the mesocrystals, such as the blocking temperature T_b^{spm} . Typically, the blocking temperature T_b^{spm} of a superparamagnetic system is identified by comparing FC to ZFC magnetization measurements [129]. As explained in the theory section, DCM does not

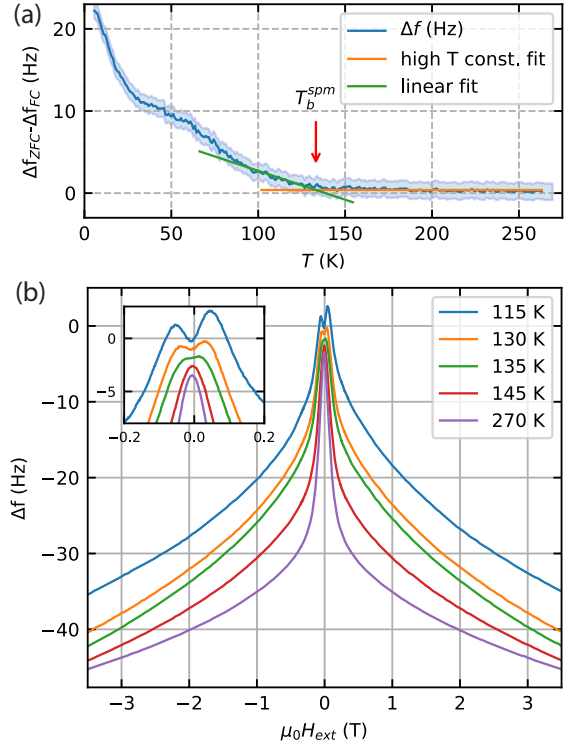


Figure 4.5 | (a) Field cooling data for sample 3. The graph shows the difference between the frequency shift for a zero field cooling and a field cooling measurement in $\mu_0 H = 125$ mT. (b) DCM response vs. external field with $\theta_h = 180^\circ$ for various temperatures around the blocking temperature for sample 2. The curves are offset for better visibility.

give access to the magnetization ($M \propto \partial\mathcal{F}/\partial H$), but is rather comparable to the susceptibility χ of a magnetic particle.

Frequency dependent measurements of χ allow the identification of T_b^{spmm} [129]. Although frequency dependent DCM measurements are complicated by the cantilever's discrete mechanical modes, we can compare FC and ZFC measurements of Δf . Fig.(4.5) (a) shows the difference between these frequency shifts, $\Delta f_{\text{ZFC}} - \Delta f_{\text{FC}}$, for sample 3. The mesocrystal is first cooled in zero field; then Δf_{ZFC} is recorded while the sample is heated to room temperature with 125 mT of field applied.

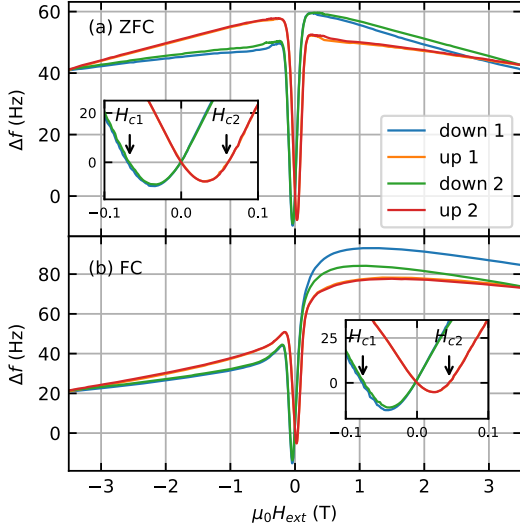


Figure 4.7 | Two consecutive Δf hysteresis loops at 5 K for (a) ZFC and (b) FC measurements with $\theta_h = 184^\circ$ for sample 3.

particles in the mesocrystal appear to increase T_b^{spmm} significantly. Temperature dependent hysteresis data, recorded for sample 2 and shown in Fig.(4.5) (b), provide further support for the value of T_b^{spmm} . With the magnetic field aligned along the hard axis, the shape of $\Delta f(H)$ drastically changes at T_b^{spmm} . Above T_b^{spmm} , the data match the predictions of our model of interacting superparamagnets. Below T_b^{spmm} , however, the maximum in Δf at zero field transforms into a asymmetric M -shape with two maxima. From the shape of the DCM curves predicted by our model for the para- and ferromagnetic states, we can identify the low-temperature onset of ferromagnetism. Hysteresis loops taken far below the blocking temperature at $T = 5$ K for sample 3 show that, at low temperatures not only superparamagnetism is blocked, but a more complicated magnetic state is present. Depending on the cooling procedure, the measurement proceeds differently, as can be seen in Fig.(4.7) for measurements with (a) ZFC and (b) FC in 3.5 T.

Three main observations can be made from the low temperature measurements: First, the hysteresis loops do not saturate even for the highest applied fields. Second, there is exchange bias present, which can be seen by comparing the positive and negative coercive fields ($\Delta f = 0$) in the insets of the figure. Both statements are true irrespective of the cooling procedure. Third, we find a highly asymmetric behavior with respect to the sign of the external field for the FC measurement. The high-field frequency shift differs strongly for positive and negative field values, which is considerably reduced for a second consecutive hysteresis loop. This means

To measure Δf_{FC} , the same procedure is repeated, but with field-cooling in 1 T. For temperatures above 133 K there is no difference between ZFC and FC measurements. Below this temperature, a difference begins to appear, suggesting that the individual nanoparticles stop behaving like superparamagnets and begin behaving like ferromagnets, i.e. they are blocked. Therefore, we conclude that the blocking temperature is $T_b^{\text{spmm}} \approx 133$ K for these mesocrystals. This temperature compares well with data from ensemble measurements of mesocrystals with similar sizes [117] (125 K for 9.6 nm and 155 K for 12.6 nm particles, while the present ones are 10.9 nm sized). Measurements on a dilute ensemble of similar-sized maghemite particles size, but with large silica shells to suppress inter-particle interactions, show $T_b^{\text{spmm}} \approx 60$ K [130]. Hence, the interactions between the

that the system can be trained, a typical behavior in an exchange biased system, as introduced in ch.(3.2).

To further understand these findings, we analyze temperature dependent hysteresis data, and extract coercive and exchange field. A few exemplary hysteresis loops are shown in Fig.(4.8) (a). The blue line in Fig.(4.8) (b) shows the temperature dependence of the coercive field $H_c = |H_{c2} - H_{c1}|/2$, where H_{c1} (H_{c2}) is the negative (positive) coercive field for a ZFC measurement. The coercivity $H_c \approx 10$ mT is constant above T_b^{spm} , as we may expect for a superparamagnetic system with strong interactions. Below T_b^{spm} , H_c starts to increase, suggesting that the net magnetic moments of an increasing number of nanoparticles switch collectively with decreasing temperature. Just below 50 K the curve steepens significantly. This may indicate a magnetic transition of unknown origin. H_{c1} and H_{c2} show the same magnitude above 90 K. Below 90 K, H_{c1} becomes larger than H_{c2} in magnitude. This effect can be quantified by the exchange bias field $H_{\text{eb}} = |H_{c2} + H_{c1}|/2$ and is shown as orange curve in Fig.(4.8) (b). From this data, we infer a blocking temperature of the exchange bias effect of $T_b^{\text{eb}} \approx 90$ K. Below T_b^{eb} , H_{eb} increases moderately with decreasing temperature. Doing the same experiment after a FC procedure leads to a significantly enhanced H_{eb} .

Fig.(4.9) shows high-field DCM data, similar to that shown in Fig.(4.2) (a)-(c), measured at different temperatures under both ZFC and FC. Fig.(4.9) (a) shows measurements of ZFC frequency shift. While the shape of $\Delta f(\theta_h)$ is preserved down to 5 K, its magnitude increases with decreasing temperature. This behavior indicates an increase of either the anisotropy, the saturation magnetization, or both. Measurements under FC give similar results as those under ZFC regardless of the FC field direction for all but the lowest temperature measurements. Below 90 K, however, the shape, orientation, and magnitude of the signal change for ZFC and FC. The direction of the maximum in $\Delta f(\theta_h)$ is observed to follow the direction of the FC field. This reorientation of the magnetic anisotropy by the FC field is observed both when the sample is cooled in an external field applied at 139° and 94° , as shown in Fig.(4.9) (b). Upon heating above 90 K, the original shape and magnitude of $\Delta f(\theta_h)$ is restored. Similar observations have been made in dilute systems of particles, where inter-particle interactions are negligible [130, 131].

As in those and similar studies [98, 132, 133], including small angle neutron scattering measurements [134, 135], we conclude that the individual nanoparticles are likely surrounded by a disordered system of surface spins. Below T_b^{eb} , these spins freeze, leading to the observed exchange bias and an additional magnetic anisotropy that can be set and oriented by FC. Given

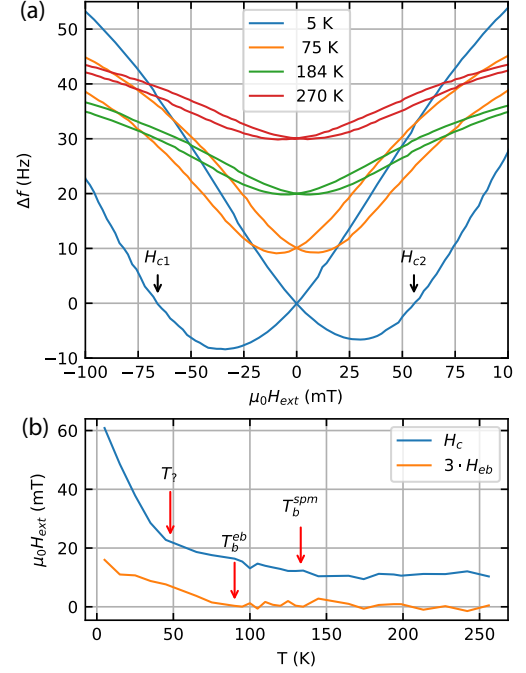


Figure 4.8 | (a) DCM response vs. external field with $\theta_h = 90^\circ$ for various temperatures around the blocking temperature for sample 2. The curves are offset for better visibility. (b) H_c and H_{eb} vs T for a field cooled measurement in hard anisotropy orientation, and zero field cooling in easy anisotropy orientation for sample 2 with $\theta_h = 90^\circ$.

the agreement of these previous measurements with our data, we find that frozen surface spins are more likely to explain the observed exchange bias and anisotropy than frustration of the core spins in our densely-packed superlattice of nanoparticles. Nevertheless, the configuration of the core spins at low temperatures remains unknown. States such as superferromagnetic and superantiferromagnetic [129] ordering or a superspin glass [136] are potentially present. Further experiments, such as real space imaging or aging experiments are necessary to pin down the mesocrystal's low-temperature magnetic configuration. The kink in the temperature dependence of H_c around 50 K, which is discussed above and shown in Fig.(4.8) (b), may be an indication of a phase transition of such a superspin state.

4.4 Summary and Conclusion

In conclusion, our measurements reveal the different contributions to the magnetic anisotropy of a mesocrystal of maghemite nanoparticles, most notably a cubic component, which we attribute to the crystalline anisotropy of the constituent nanoparticles. A model considering interacting superparamagnetic nanoparticles captures most of our findings. The system remains in a superparamagnetic state down to $T_b^{\text{spm}} \approx 133$ K. Below $T_b^{\text{eb}} \approx 90$ K, exchange bias and a frozen spin state are present in the system, consistent with a disordered layer of surface spins on the individual nanoparticles, as observed in earlier works. We emphasize that the observation of cubic magnetic anisotropy in these nanoparticles is only possible, because of the combination of two techniques: the size-selective self-assembly of nanoparticle mesocrystals with a narrow size distribution and a high degree of orientational order [116, 117], and measurement by DCM, which is sensitive enough to resolve the magnetism of individual mesocrystals. This ability to isolate the magnetic response of a single mesocrystal overcomes the limitations of measuring ensembles, which are composed of mesocrystals of varying size, shape, and orientation. This disorder and the potential for interactions between mesocrystals complicates the determination of their individual magnetic properties and those of their constituent nanoparticles, especially anisotropy. In the future, similar techniques combining self-assembly and DCM may become a powerful means for assessing the magnetic properties of other nanoparticles, which are too small to investigate individually.

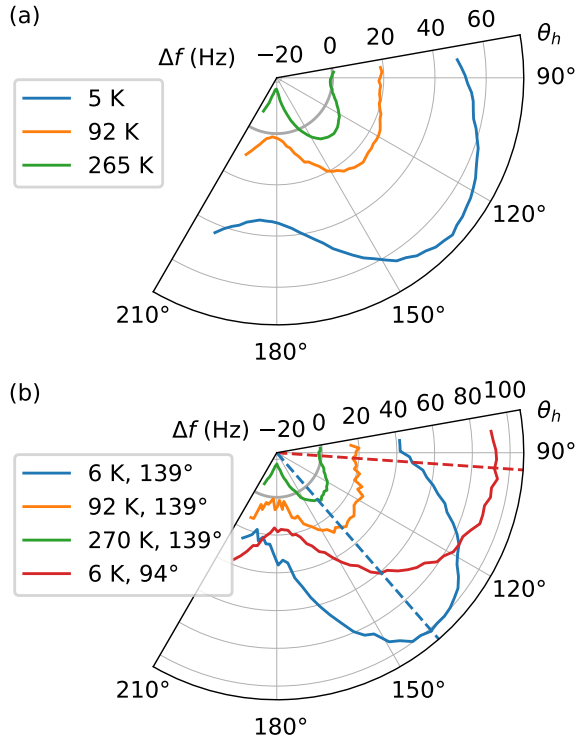


Figure 4.9 | High-field frequency shift $\Delta f(H = 3.5 \text{ T}/\mu_0, \theta_h)$ for sample 3 depending on the external field direction for various temperatures. The sample undergoes (a) ZFC and (b) FC. The magnetic field for FC is applied at the angle indicated by the color-coded dashed line.

5 Stability of Néel-Type Skyrmion Lattice Against Oblique Magnetic Fields in GaV_4Se_8

5.1 Introduction

Lacunar spinels are composite materials of the chemical formula AB_4X_8 , where $\text{A}=\text{Al, Ga, Ge}$; $\text{B}=\text{V, Mo, Nb, Ta}$ and $\text{X}=\text{S, Se, Te}$. They exhibit a multitude of correlation and spin-orbit effects [137], as well as more than one type of ordering simultaneously, making them a member of the family of multiferroics [138]. The material studied here is GaV_4Se_8 , which has a cubic crystal symmetry at room temperature but undergoes a Jahn-Teller structural transition to a rhombohedral state at $T \approx 42$ K. This induces electrical polarization along the main crystal axes, forming four distinct types of structural domains. In addition, magnetic ordering sets in at $T \approx 17$ K and develops in the polar phase, where each polar domain has its own anisotropy axis of easy plane type.

The occurrence of multiple anisotropy axes of the same type in a bulk crystal of a material is itself of interest in the context of this thesis. The magnetic structure of the material is more complex, however, since the rhombohedral phase lacks inversion symmetry and thus enables the onset of Dzyaloshinskii-Moriya interaction (DMI), allowing for non-collinear magnetic states such as cycloids and magnetic skyrmions, separated by sharp phase boundaries. Measurements of phase transitions with the goal to map out the stability phase diagram of GaV_4Se_8 has been done using a variety of methods, summarized in Geirhos *et al.* [137]. In that work, only phase transitions visible in most of the applied experimental methods are considered. While the main phase boundaries predicted by theory [139] are clearly visible in those measurements, there are additional transitions in some of the measurements, which indicate the presence of other magnetic states, which have not been reported before.

Transition between the magnetic states within a structural domain are induced by a critical field component along the anisotropy axis and can hence be triggered by a rotation of the external magnetic field at a given field strength. Mapping the full phase diagram at a given temperature thus requires measurement of hysteresis curves in small angular steps and reading out the values for the switching fields for each external field angle. Since multiple uniaxial anisotropy directions are present at the same time, assigning the features to the structural domain of a certain axis is complicated by the fact that the four domain types switch individually, depending on the field strength and their respective angle with the external field.

This chapter first gives a brief introduction to DMI and non-collinear magnetism before the DCM contribution to the results given in [137] will be described and placed in context. Note that we focus on GaV_4Se_8 in this chapter, even though DCM measurements have been performed on GaV_4S_8 as well, with the results of this study reported in [44] and alongside the GaV_4Se_8 measurements in the following publication, which this chapter is based on:

Stability of Néel-type skyrmion lattice against oblique magnetic fields in GaV₄S₈ and GaV₄Se₈

 B. Gross,¹ S. Philipp,¹ K. Geirhos,² A. Mehlin,¹ S. Bordács,^{3,4} V. Tsurkan,^{2,5} A. Leonov,⁶
 I. Kézsmárki,² and M. Poggio^{1,7}
¹Department of Physics, University of Basel, 4056 Basel, Switzerland

²Experimental Physics V, Center for Electronic Correlations and Magnetism, University of Augsburg, 86159 Augsburg, Germany

³Department of Physics, Budapest University of Technology and Economics, 1111 Budapest, Hungary

⁴Hungarian Academy of Sciences, Premium Postdoctor Program, 1051 Budapest, Hungary

⁵Institute of Applied Physics, MD-2028 Chisinau, Republic of Moldova

⁶Department of Chemistry, Faculty of Science, Hiroshima University Kagamiyama, Higashi Hiroshima, Hiroshima 739-8526, Japan

⁷Swiss Nanoscience Institute, University of Basel, 4056 Basel, Switzerland

 (Received 24 June 2020; revised 18 August 2020; accepted 19 August 2020; published 3 September 2020)

5.2 Non-collinear magnetic structures

The discussion of magnetic structures so far has been under the assumption that, on a microscopic level, the magnetic moments are preferentially aligned in parallel by virtue of the exchange interaction. There are, however, crystal structures that allow for an asymmetric exchange interaction, that tends to align the magnetic moments perpendicularly. This is now called Dzyaloshinskii-Moriya interaction (DMI) as it was first introduced by Dzyaloshinskii in 1958 in a model to describe weak ferromagnetism [140], with Moriya identifying the mechanism behind it in 1960 [141]. A prerequisite for DMI is the lack of inversion symmetry, which is inherent to a set of crystal structures identified by Bogdanov and Yablonskii in 1989 [142]. Among them is also the C_{nv} ($n=1,2,3$) class, represented for example by a rhombohedral crystal symmetry. DMI can be described by the following energy term:

$$E_{DM} = -\mathbf{D}_{ij} \cdot (\mathbf{S}_i \times \mathbf{S}_j) \quad (5.1)$$

where \mathbf{D}_{ij} is called Dzyaloshinskii-vector or DMI-vector. The competition between DMI and exchange interaction results in a slight tilt of the magnetic moments with respect to their direct neighbors, rather than a fully parallel or perpendicular orientation. As a result, magnetic states emerge, where the magnetic moments are not oriented in a collinear fashion anymore, such as spirals, helices, cones or magnetic whirl-pool like structures called skyrmions. Magnetic skyrmions have become a relevant research topic in both fundamental science and for applications such as magnetic racetrack memories [29, 143] and spintronic devices [25, 144].

There are two main types of crystalline bulk magnetic systems that host non-collinear magnetic states: the first ones are cubic helimagnets with a B20 crystal symmetry such as MnSi, FeGe or Cu₂OSeO₃. Skyrmions in this type of magnets are called Bloch-type skyrmions, in analogy to the rotation direction of the magnetization in a Bloch domain wall. The magnetization rotates perpendicular to the radial direction, as depicted in Fig.(5.1) (a). Typically, periodic lattices of Bloch skyrmions occur only in a small stability range in a $T - H$ phase diagram, a pocket shaped region just below the curie temperature of the magnet [88, 89]. Individual or metastable skyrmions of this type have been reported to occur in a much wider temperature range [146]. The symmetry of the B20 lattice reduces the DM energy to an isotropic form, with the consequence, that the axis of orientation of Bloch skyrmions always aligns with the external magnetic field [139]. Two more magnetic phases typically occur in helimagnets. In the helical phase, which typically is the ground state, the magnetization forms elongated helices ordered in stripes. Increasing the external field, the helices are modulated

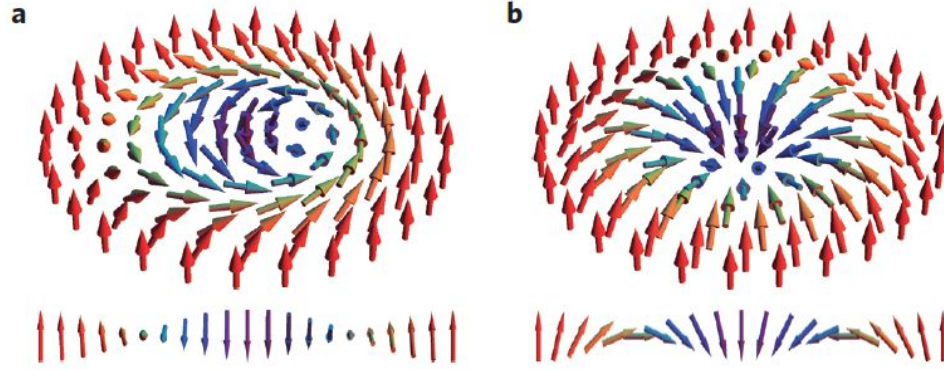


Figure 5.1 | Schematis of Boch-type (a) and Néel-type skyrmions. Adapted from [145]

and the spins are forming cones by tilting into the field direction, which is called the conical phase. Further increasing the field slowly narrows the cones, and eventually closes them upon the transition to a field polarized phase, where all the spins are pointing along the external field direction.

The other class of bulk materials are polar magnets, as investigated in this chapter, which host a different type of skyrmions called Néel-type skyrmions, also in analogy to the rotation sense of the Néel domain wall. For a long time, this type of skyrmions has only been observed in multi-layered thin films where the DMI arises at the interface of the different layers [147, 148], before it was discovered in GaV_4S_8 by Kézsmarki *et al.* in 2015 [145]. In this case, the magnetization rotates radially from the center, as depicted in Fig.(5.1) (b). Unlike in helimagnets, the orientation of the axis of orientation of the skyrmions is associated with the polarization axes of the crystal, which determines the orientation of the DMI vector. Typically there is only a cycloidal state observed besides the field polarized state in polar magnets. Consequently, the $T - H$ phase diagram shows a stabilized skyrmion lattice phase over a wide temperature and magnetic field range, even down to lowest temperature, which may be attributed to the absence of a competing conical phase [139, 149]. The cycloidal phase is comparable to the helical phase, with the magnetic moments rotating perpendicular rather than parallel to the \mathbf{q} -vector of the cycloids. As Geirhos *et al.* have shown in Ref. [137], a single polar domain in GaV_4Se_8 can host multiple directions of \mathbf{q} -vectors after zero-field cooling, which reorient into a single \mathbf{q} state upon application of an external field. This is not reversed if the field is turned off. A multi- \mathbf{q} state can be re-initialized only after repeated zero field cooling.

5.3 Sample and Cantilever

Single crystals of GaV_4Se_8 are grown by a chemical transport reaction method using iodine as a transport agent [145]. X-ray diffraction measurements of both sample materials show impurity-free single-crystals [150]. We attach an individual crystal of GaV_4Se_8 , which is a few tens of micrometers in size, to the end of a commercial Si cantilever (Nanosensors™TL-cont) using non-magnetic epoxy, as shown in Fig. (5.2). The cantilever is 440 μm -long, 50 μm -wide, and 2.3 μm -thick. Unloaded, it has a resonance frequency of about 16 kHz, quality factor around 5×10^5 , and spring constant of 300 mN/m. Due to the additional mass of the samples, the resonance frequency of a loaded cantilever shifts to around 3 kHz.

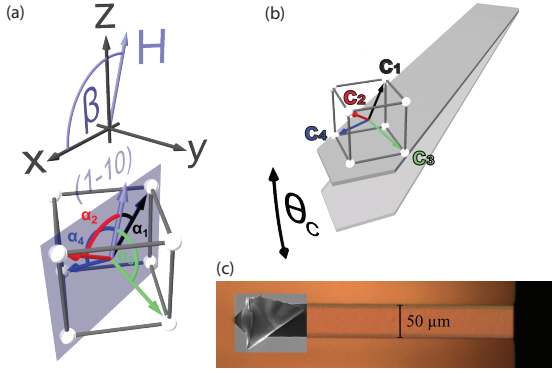


Figure 5.2 | Schematics of the measurement setup. (a) shows the coordinate system and the definition of $\beta = 90^\circ - \theta_h$ as the angle between \mathbf{H} and \mathbf{x} in the top figure. Below, the rotation plane of \mathbf{H} and the definition of the angles α_i is given. (b) The cantilever, its oscillation angle θ_c , and the crystalline axes of the measured sample. Black, red, green, and blue lines correspond to the four \mathbf{c}_i . (c) Composite optical and scanning electron micrograph of the measured GaV_4Se_8 sample mounted on the cantilever.

The sample is attached near the free end of the cantilever with the (001) surface pressed flat against the Si surface. The orientation can roughly be estimated from optical and scanning electron microscope images. The resultant direction of the sample's crystalline axes with respect to the cantilever is shown in Fig. (5.2): specifically the approximate orientation of the four cubic $\langle 111 \rangle$ axes \mathbf{c}_i ($i = 1, 2, 3, 4$) is shown in black, red, green, and blue.

As mentioned before, GaV_4Se_8 undergoes a Jahn-Teller structural phase transition from a non-centrosymmetric cubic to a rhombohedral structure at 42 K [26, 27, 150, 151]. The transition is characterized by a stretching of the cubic unit cell along one of the four cubic body diagonals \mathbf{c}_i , resulting in four different structural domains. The rhombohedral distortion also gives rise to polarization along \mathbf{c}_i , making these the polar axes of the system. The multi-domain state is composed of

sub-micrometer-thick sheets of these four different rhombohedral polar domains, which we label P_i [137, 152]. The polar axis \mathbf{c}_i also corresponds to the axis of magnetic anisotropy in the respective rhombohedral domain state, which is of easy-plane type [145, 149, 153] in GaV_4Se_8 .

For any given orientation of the applied field \mathbf{H} , there can be up to four different angles, α_i , between \mathbf{H} and \mathbf{c}_i as shown in Fig.(5.2) (a). Note that we define α_i modulo π . Due to crystal symmetry, if α_i exceeds 180° , the relevant angle is between \mathbf{H} and $-\mathbf{c}_i$. The domain walls (DWs) separating the structural domains need to be mechanically compatible and charge-neutral. DWs with these properties are normal to $\mathbf{c}_i + \mathbf{c}_j$, the sum of the two polar directions of the domain states P_i and P_j as shown in Fig. (5.4) [137, 152, 154]. For example, mechanically and electrically compatible DWs connecting a P_1 (black) and a P_2 (red) domain are parallel to (001) planes, cf. Fig.(5.4). The same is true for DWs between P_3 (green) and P_4 (blue) domains.

5.4 Results and Discussion

5.4.1 Magnetic phase diagram: In-domain transitions

We measure the frequency shift and the dissipation as a function of the external field magnitude and the angle $\beta = 90^\circ - \theta_h$ at a fixed temperature of 12 K. Note that this definition of the external field angle is made to be consistent with Ref. [46]. The field is rotated roughly in the (1-10) plane of the sample. By changing β , all angles α_i with the given domain directions change differently. Thus, the value of the external field component along the crystal axes is different for all \mathbf{c}_i , which means that the magnetic field strength required to induce a phase transition in the corresponding domains is different as well. This results in a number of features (peaks and dips) in the frequency and dissipation curves that need to be assigned to transitions in the

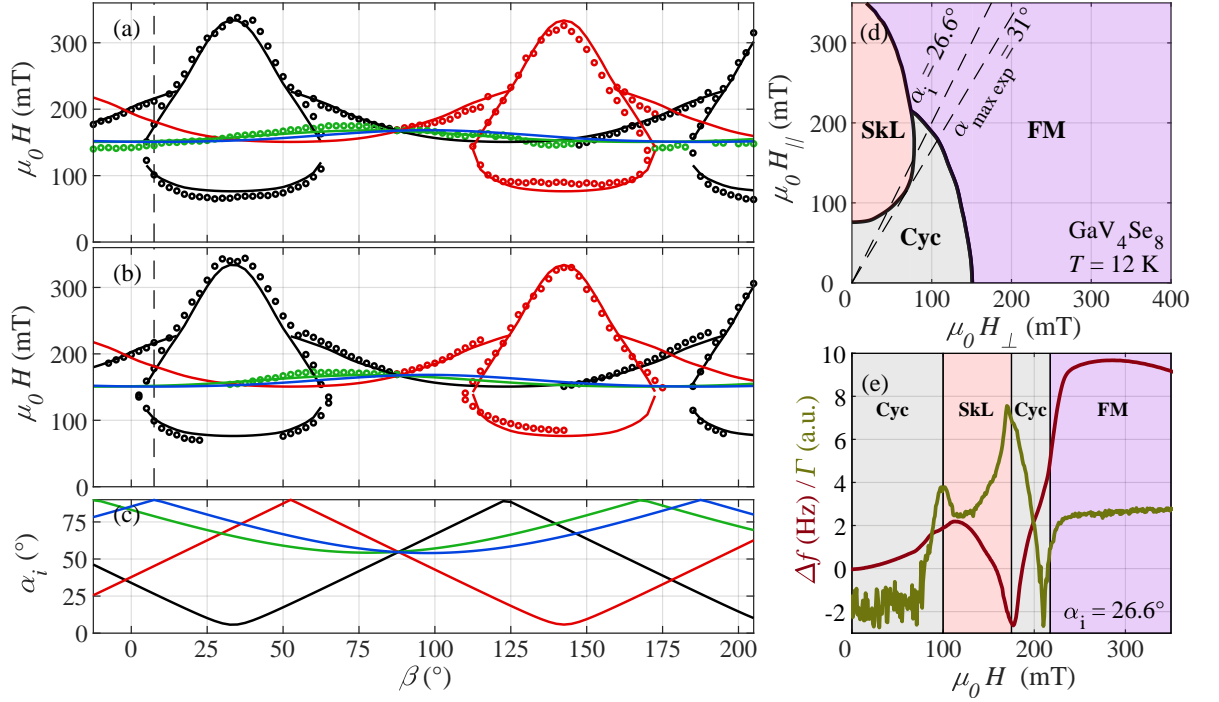


Figure 5.3 | Magnetic phase transitions measured in GaV_4Se_8 at $T = 12$ K. Transitions extracted from DCM measurement of (a) $\Delta f(H)$ and (b) $\Gamma(H)$ are plotted as circles as a function of β . Black, red, green, and blue markers correspond to transitions for domain P_1 , P_2 , P_3 , and P_4 , respectively. Color-coded lines correspond to phase boundaries for the each color-coded domain as indicated by lines in the phase diagram (d). (c) Angle α_i between corresponding polar axis and the external field \mathbf{H} vs β for all four rhombohedral domains, using the same color code as in (a) and (b). (d) Best-fit magnetic phase diagram for single-domain GaV_4Se_8 as a function of field applied perpendicular and parallel to the axis of symmetry. (e) DCM measurement of $\Delta f(H)$ for $\alpha_i = 26.6^\circ$ ($\beta = 7.5^\circ$) showing the reentrant Cyc phase of domain 1 (black). Transitions from other domains are not indicated. These measurements corresponds to line-cuts along the dashed vertical lines in (a) and (b) and the dashed diagonal line labelled $\alpha_i = 26.6^\circ$ in (d).

different domains. The same procedure is described in detail in Ref. [46] for measurements in GaV_4S_8 . Essentially, we compare all the measurements of Δf and Γ and associate features that occur in both measurements at the same external field value with phase transitions. Extracting those values and plotting against β results in the pattern shown by the circles in Fig.(5.3) (a) and (b). The color code corresponds to the different domains as given in Fig.(5.4). Knowing the orientation of the sample and thus the values for α_i (compare Fig.(5.3) (c)), we can calculate the values of β for which the field components $H_{||}$ along the domain axes reach the transition value. Thus, the solid lines in Fig.(5.3) (a) and (b) represent the phase boundary inside the domains as given in Fig.(5.3) (d).

Using previous measurements made by Bordács et al. along particular crystalline directions [149], as well as neutron diffraction data by Geirhos et al. [137] for guidance, we assign each feature to a transition between Cyc, SkL, or FM states for a certain domain and color-code it accordingly. The overall form of the phase diagram agrees with that suggested by Leonov and Kézsmárki [139]. Note that the rotation plane of \mathbf{H} , contains \mathbf{c}_1 and \mathbf{c}_2 , but not \mathbf{c}_3 and \mathbf{c}_4 .

An Euler rotation of the crystal (-14 , -1 and 7°) with respect to ideal configuration, shown in Fig.(5.4), is required such that the phase boundaries corresponding to the different domain states (P_1 , P_2 , P_3 , P_4) collapse onto the single boundary diagram of Fig.(5.3) (d). Features

assigned to the Cyc-to-FM transition of domain P_3 (green) are difficult to distinguish from those occurring for the same transition in P_4 (blue), because they are expected to occur at nearly the same H and β in Figs.(5.3) (a) and (b). Since this distinction does not affect the form of the phase diagram in Fig.(5.3) (d), our assignment of all such features to the P_3 rather than P_4 transition is unimportant. For the P_1 (black) and P_2 (red) domains, which are the only two experiencing sufficient H_{\parallel} to reach the SkL phase, the boundaries of the SkL state appear as prominent rain-drop-like shapes in Figs(5.3) (a) and (b). From the intersection of the SkL with the Cyc phase boundary in (d), we extract a threshold angle $\alpha_{\max} = 31^\circ$ for the SkL phase in GaV_4Se_8 at $T = 12\text{ K}$.

We note the presence of a reentrant Cyc phase for angles $19^\circ < \alpha_i < 30^\circ$, as predicted by Leonov and Kézsmárki [139]. For this range of α_i , two successive first-order phase transitions from Cyc to SkL and back occur as a function of increasing field. The signature of this behavior in DCM is shown in Fig.(5.3) (e).

5.4.2 Magnetic phase diagram: Domain Wall states

Geirhos et al. observed anomalies in various macroscopic thermodynamic properties of GaV_4Se_8 , emerging exclusively in crystals with polar multi-domain structure. They suggest a possible scenario for the formation of magnetic states at the structural DWs [137]. Magnetic interactions change stepwise at the DWs and spin textures with different spiral planes, hosted by neighboring domains, need to be matched there. This can, for example, lead to conical magnetic states at the DWs with a different closing field magnitude than bulk magnetic states. Here, we adapt and modify this model in order to analyze its applicability to anomalies observed in our DCM measurements of GaV_4Se_8 , which cannot be assigned to bulk magnetic phase transitions. For an arbitrary orientation of the external magnetic field, magnetic states confined to DWs with different orientations are expected to undergo field-induced transitions, similarly to the in-domain magnetic states. However, in this case the situation is more complex: The stability of the magnetic states confined to DWs is determined by the orientation of the field with respect to the magnetic anisotropy axes of adjacent domains and to the DW itself.

It is reasonable to assume, that the angle, γ_n , between \mathbf{H} and the normal of the DW planes, given by $\mathbf{c}_i + \mathbf{c}_j$ plays a decisive role in setting the angular range, across which confined states are stable. This leads to three pairs of DWs, as shown in Fig.(5.4), each sharing the same γ_n for a given \mathbf{H} . For DWs in a pair, however, the relative orientation between the magnetic anisotropy axes of the two domains involved and \mathbf{H} is not the same. For example, consider the P_1P_2/P_3P_4 pair: the rotation plane of \mathbf{H} ($1\bar{1}0$) contains the anisotropy axes of P_1 and P_2 , but not the anisotropy axes of P_3 and P_4 ; they span 54° with this plane. We therefore introduce another angle, γ_p , between \mathbf{H} and the difference of the two polar vectors $\mathbf{c}_i - \mathbf{c}_j$, which lies in the DW plane. Both these angles $\gamma_n(\beta)$ and $\gamma_p(\beta)$, plotted in Fig.(5.5) (a) and (b), respectively, are expected to affect the stability of the DW-confined magnetic states.

In the angular dependent torque measurements, shown in Figs.(5.5) (c)-(f), we observe at most four anomalies (open circles) for a given field orientation. Since there are six types of DWs, distinguished by γ_n and γ_p , some transitions, which occur simultaneously in different types of DWs appear as a single anomaly, while some transitions appear not to be experimentally observable. In the following analysis, we take into account an additional anomaly (crosses) between $\beta \simeq 40$ and 130° at field values around 100 mT, which is not present in our DCM measurements, but has been observed in magnetoelectric measurements [137]. Example

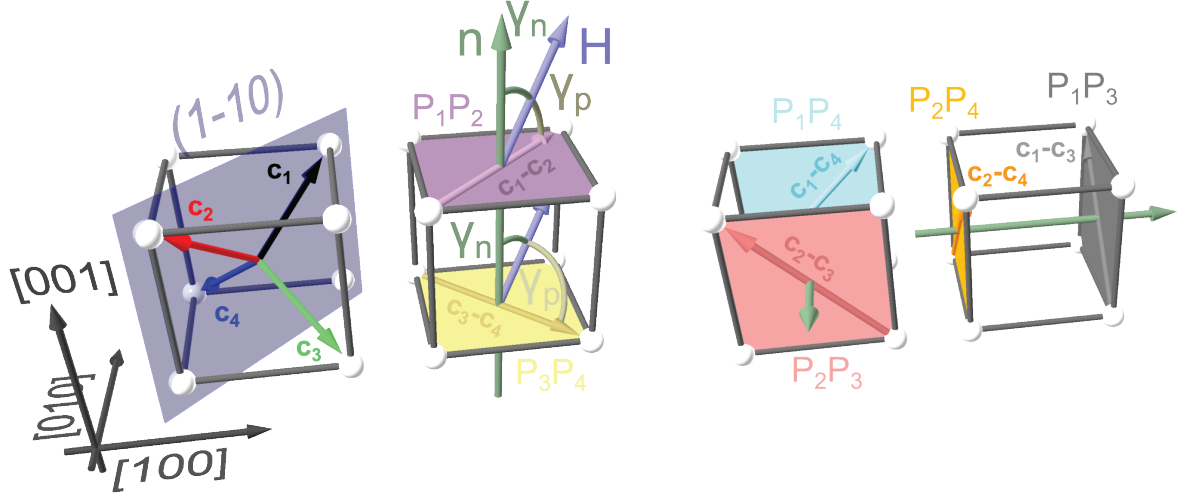


Figure 5.4 | Schematic for understanding the orientation of the 6 different domain walls types. Left: Directions of the four possible polar axes, P_1 - P_4 , which are parallel to the axes of magnetic anisotropy \mathbf{c}_i within the corresponding domains. The transparent blue plane indicates the approximate plane of rotation of the external magnetic field and the coordinate system indicates the crystal directions. Left center: Mechanically compatible and charge neutral DWs separating P_1 and P_2 domains are parallel to the (001) plane, just as DWs between P_3 and P_4 domains. The former and latter DWs are referred to as P_1P_2 and P_3P_4 , respectively. γ_n , the angle between \mathbf{H} and the normal vector \mathbf{n} , which is proportional to $\propto \mathbf{c}_i + \mathbf{c}_j$, is shown for both DW pairs. γ_p , the angle between \mathbf{H} and $\mathbf{c}_i - \mathbf{c}_j$, is also shown. Right center and Right: The other two pairs of DWs sharing the same orientation. The normal vector of the corresponding planes and their labels are indicated for the three cases, as well as the difference vector $\hat{\mathbf{c}}_i - \hat{\mathbf{c}}_j$, unique to each DW type.

measurements of Δf and Γ are shown in Figs.(5.5) (g) and (h), where anomalies assigned to DW states are indicated by vertical dash-dotted lines.

As a first scenario, we suggest the assignment of the observed anomalies as shown in Fig.(5.5) (c). In this way, both domains adjacent to a DW host the Cyc state and the DW-confined state emerges due to the matching of these two cycloidal patterns for all observed anomalies. This is specifically notable for the anomalies meeting at $\beta \approx 90^\circ$. For example, the anomaly assigned to be a P_2P_4 DW (orange), would progress above 150 mT for $\beta > 90^\circ$, but because in-domain states within the P_4 domain (blue axis) transform from the Cyc to the FM state for $\beta > 90^\circ$ and $H > 150$ mT, this anomaly disappears for larger angles. The same is true for the other end of this anomaly ($\beta = 12.5^\circ$). Similarly, the anomalies assigned to transitions in the P_1P_2 DWs are limited by the two skyrmion pockets of the P_1 and P_2 domains. No anomaly is observed in angular ranges, where the adjacent domains host magnetic states other than the Cyc. An alternative scenario is an extension of the one suggested by Geirhos et al. [137], shown in Fig.(5.5) (d). This scenario allows some DW transitions to persist even when one of the adjacent domains is in the Cyc phase, while the other one is in the SkL phase. Such a situation occurs for the P_1P_2 DW transition, which penetrates both the P_1 and the P_2 SkL pockets. In both scenarios, the mirror symmetry expected across $\beta \approx 90^\circ$, as dictated by $\gamma_n(\beta)$ and $\gamma_p(\beta)$ is fulfilled: the transition lines are either symmetric to this point or they have a symmetry-related counterpart. The basis for both scenarios is the occurrence of a distinct magnetic state confined to DWs, and its transition to the FM state at certain critical field, observed as an additional anomaly in the DCM measurement. The angle of the applied field

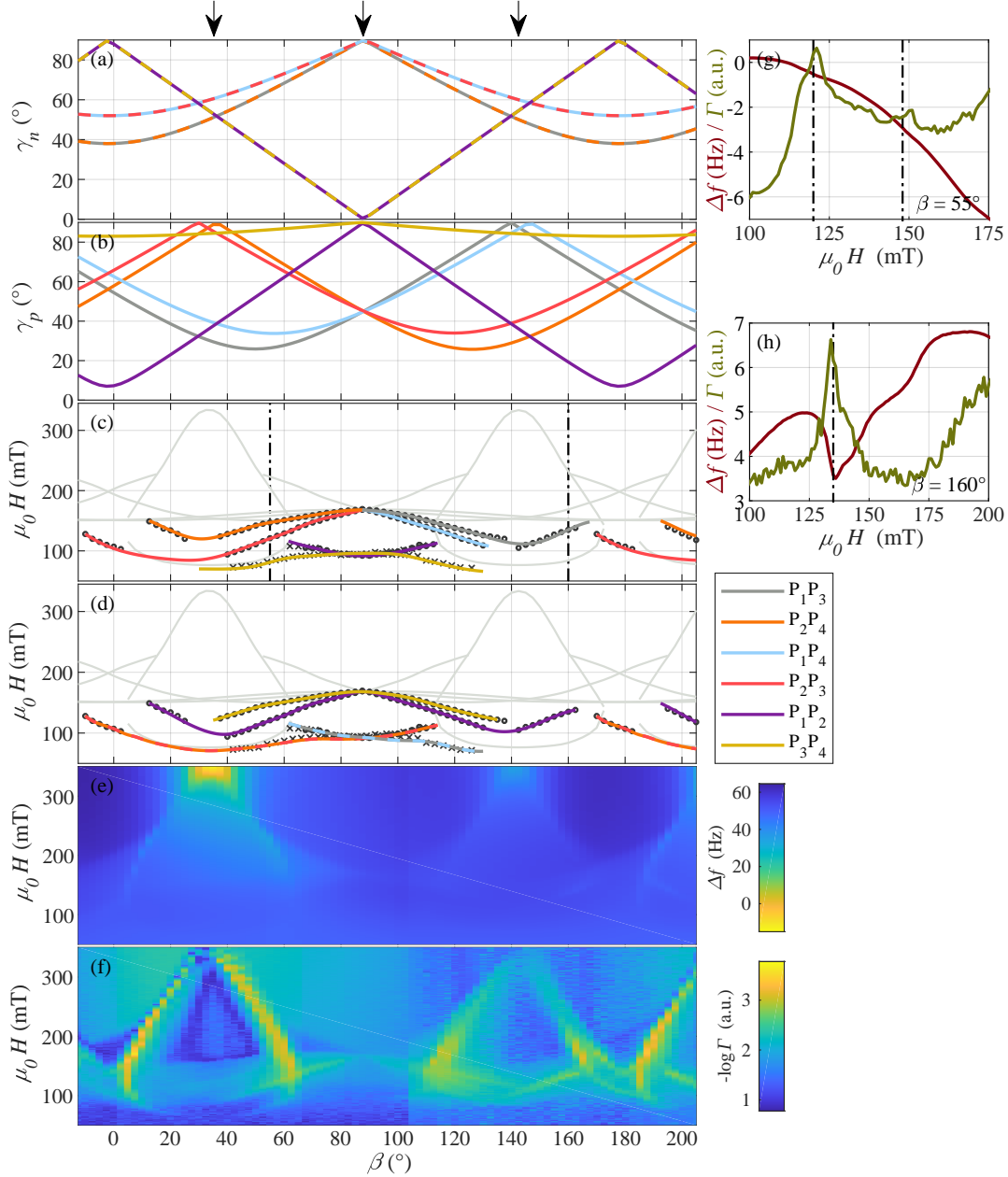


Figure 5.5 | Anomalies in $\Delta f(H)$ and $\Gamma(H)$ assigned to transitions of DW rather than bulk magnetic states. Arrows at the top indicate from left to right the approximate angle β corresponding to the [111], [001] and [11 - 1] directions, respectively. (a) Angle γ_n between the normal vector of a DW and \mathbf{H} plotted against β . The color of the dashed lines shows their correspondence to a DW type in the legend. (b) Angle γ_p between the vector formed by the difference of the polar axis vectors of the two adjacent domains of a DW and \mathbf{H} plotted against β . (c) Transitions extracted from both Δf and Γ that are not assigned to a domain transition (circles). Crosses show transitions extracted from magnetoelectric measurements [137], scaled by about 0.9 to match the DCM data. Colored lines show the suggested assignment of the transitions to DW types as denoted in the legend. Light gray lines show the bulk domain transitions. (d) Same data as in (c) with a different assignment of transitions. Color map of (e) $\Delta f(H, \beta)$ and (f) $-\log_{10} \Gamma(H, \beta)$. (g) and (h) show example DCM measurements with dash-dotted vertical lines indicating the assigned transition fields. Dash-dotted vertical lines in (c) indicate the value of β of the example measurements.

with the DW-normal, γ_n , and the orientation of its component in the DW-plane, γ_p , appear to be important parameters in determining the critical field of the DW states.

5.5 Summary and Conclusion

We use DCM to measure phase transitions in GaV_4Se_8 , a multiferroic polar magnet, which hosts con-collinear magnetic phases. We extract the magnetic phase diagram as a function of applied field magnitude and direction that is in good qualitative agreement with the theoretical predictions of Leonov and Kézsmárki [139], confirming the general validity of their model. This agreement, in turn, provides indirect confirmation that, under oblique applied magnetic field, the axes of Néel-type skyrmions stay locked to the anisotropy axis while their structure distorts and their core displaces. The measurements reproduce the overall structure of the phase diagram, imposing a maximum angle α_{max} of magnetic field applied with respect to the anisotropy axis, for which a SkL phase persists. In addition, they show that easy-plane anisotropy – as found in GaV_4Se_8 – increases their stability for fields parallel to this axis. Our results also confirm the existence of a reentrant Cyc phase in GaV_4Se_8 , which was anticipated to occur for certain values of easy-plane anisotropy. Finally, anomalies in $\Delta f(H)$ and $\Gamma(H)$, which cannot be explained as bulk domain transitions, are consistent with distinct magnetic states confined to polar structural DWs and their transition from the Cyc to FM state, as proposed by Geirhos et al. [137].

Nevertheless, the measured magnetic phase diagram is not in strict quantitative agreement with the predicted one. Further experimental investigation – especially real-space imaging – of anomalies assigned to transitions of DW-confined magnetic states is required to characterize the spin pattern associated with these states.

6 Conclusion and Outlook

Measuring magnetic properties of nano- to micrometer- sized magnetic particles requires particularly sensitive methods to overcome the issues of intrinsically weak signals. The results presented in this thesis show, that this can be achieved using Dynamic Cantilever Magnetometry (DCM), a method in which the specimen is attached directly to the apex of an ultra-sensitive Si cantilever. We have shown that the measured properties obtained from DCM can be compared to the real and imaginary part of a susceptibility measurement. DCM not only allows for the investigation of individual magnets in the nanometer range, the interferometric read-out scheme also circumvents the need of electrical contacts, which makes it suitable for the investigation of insulating samples.

We have shown that the frequency shift asymptotically approaches a constant value if the externally applied field is high enough. In this field regime, which we call the high-field limit, the value of the asymptote depends on the orientation of the applied field with respect to the sample's magnetic anisotropy. This feature, together with the possibility to apply the external magnetic field with a magnitude of ± 4.5 T in an angular range of 117° makes DCM in our setup a powerful tool to determine strength, direction and type of the magnetic anisotropy of the specimen. The progression of the frequency shift curve upon reversal of the external field can give information about magnetic switching, magnetic reversal processes and effects related to the involved anisotropies.

In order to analyze the data, we reconstruct the signal by employing analytical, as well as numerical micromagnetic methods. The analytical models rely on the description of the magnetization as an individual macro spin, as first introduced by Stoner and Wohlfarth. This method can help to gain an intuitive picture of the behavior of the magnetic moment and can in some cases deliver numerical values, e.g. for anisotropy constants by fitting the corresponding equations to the high-field limit data. However, the model has its limitations for processes that include magnetic switching of parts of the magnetization, or in the description of magnetic states such as vortices. Numerical micromagnetics, in contrast, considers a distribution of magnetic moments by discretization of the sample geometry using a suitable mesh. Solving the Landau-Lifshitz-Gilbert (LLG) equation, a magnetization map is realized that minimizes the magnetic energy. In both cases, the frequency shift is calculated as the second derivative of the magnetic energy with respect to the oscillation angle.

We applied these techniques in order to investigate the magnetic hysteresis of individual Janus Particles (JP) with hemispherical caps. JPs find applications for example in lab-on-chip devices, drug delivery or as micro robots. Actuation of the particles, however requires the magnetic cap to exhibit a non-zero magnetic moment at remanence. Typically, the magnetic remanent state in ferromagnetic caps is a vortex which has almost no net magnetic moment, therefore preventing the use of the JP in applications. One possibility to overcome this issue is by adding an antiferromagnetic layer which, upon field cooling, interacts with the ferro-

magnetic layer and generates a unidirectional anisotropy by virtue of exchange bias. We have investigated the effects of exchange biased JP and found that by introducing a unidirectional anisotropy, the remanent state is no longer a vortex but an onion state, which carries a non-zero magnetic moment. If we normalize the magnetic moment of a vortex state by the saturation moment, $M_s V$, we find that the global vortex state hosted by the fmJP has a moment value of 0.03. For the simulations of the ebJP we find a total magnetic moment at remanence, normalized by its maximum value of $M_s V$, of 0.89 and 0.71 depending on whether \mathbf{H} is applied along the hard or easy direction of the external field, respectively. This remanent moment represents an increase of more than one order of magnitude compared to the remanent moment of the fmJP. Hence, introducing exchange bias to magnetic JPs, if strong enough, succeeds in stabilizing a high-moment onion state in remanence. We further determine direction and type of the magnetic anisotropy of the magnetic cap. Using angle-dependent measurements of the frequency shift in the high-field limit have shown that the anisotropy is of easy-plane type, with the magnetic hard direction pointing towards the pole of the cap. We investigated the behavior of the effective demagnetization factor D_u for a spherical cap, a geometry for which no analytic model exists to calculate a precise value for this property.

Maghemite mesocrystals are micrometer-sized structures that consist of a large number of perfectly arranged cubic maghemite nanoparticles of equal size. In order to describe the anisotropy of the mesocrystals, a sum of a uniaxial and a cubic term is necessary. We were able to show that the uniaxial contribution arises due to the overall shape of the mesocrystal, whereas the cubic term has its origin in the crystal structure of the nanoparticles. This finding was only possible due to the perfect arrangement of the nanoparticles. At room temperature, the mesocrystal behaves like an anisotropic paramagnet, while at lower temperature, the DCM curves are indicative of a ferromagnetic behavior. This behavior arises due to the small size of the constituting nanoparticles, which are superparamagnetic above a critical temperature called blocking temperature T_B , which we measured to be at $T_B = 133$ K. At even lower temperatures, around $T = 5$ K, a more complicated magnetic state is present, which needs to be identified using sensitive imaging methods such as scanning SQUID magnetometry. We have further shown, that the direction of the effective anisotropy aligns with the external field upon field cooling. We attribute this effect to a disordered system of surface spins that surround the individual nanoparticles.

In another study, we investigated the multiferroic polar magnet GaV_4Se_8 , which belongs to the family of Lacunar spinels. GaV_4Se_8 undergoes a Jahn-Teller type structural transition at $T = 42$ K, which results in the formation of electrically polarized structural domains along the main axes of the cubic crystal lattice. Magnetization develops inside the domains below $T = 17$ K, being host to different non-collinear magnetic structures such as cycloids and magnetic skyrmions. The latter appear in form of a regular lattice which is oriented perpendicularly to the respective polarization axis P_i . The structural domain walls separating the domains coincide with the $[100]$ planes of the cubic lattice. Transitions between magnetic states happen if a critical value of the magnetic field component parallel to the polarization axes is reached, resulting in a magnetic stability phase diagram that depends on the angle of the applied field. Using DCM, we were able to map out this stability phase diagram and identify a critical angle of $\alpha_i = 31^\circ$ that the external field can have with the P_i in order for the skyrmion lattice phase to be still stable. Also, at $\alpha_i = 26.6^\circ$ we confirmed the occurrence of a re-entrant state, where the magnetic state transforms from a cycloid, to a skyrmion lattice and again to a cycloid

before it becomes fully field-polarized. This state was theoretically predicted before but not experimentally confirmed. Being part of a collaborative effort, the DCM data helped identify a novel magnetic state embedded in the cycloidal phase of polar multidomain samples that is correlated to the structural domain boundaries.

The data presented here introduce DCM as a powerful tool to measure the magnetism of nano- to micrometer-sized magnetic materials. However, the technique has several limitations. First, the sensitivity and spring constant of the cantilever need to be compatible with the expected dynamic torque. Even though the design of the ultra-soft cantilevers provides a broad bandwidth of possible samples, the technique is ultimately limited by the availability of a suitable sensor. Second, the resonance frequency of the magnet-on-cantilever system is typically on the order of a few kHz, whereas magnetization dynamics typically are on the order of a few GHz. Thus, there is no transfer function that allows to measure magnetization dynamics.

Losby *et al.* presented a scheme to circumvent this issue by applying two microwave fields with frequencies f_1 and f_2 which are separated in frequency by exactly the cantilever resonance f_0 , such that $|f_1 - f_2| = f_0$ [155]. In that way, the dynamics of the magnetization is coupled to the the sensor and by measuring the oscillation amplitude as a function of f_1 , a magnetic resonance spectrum can be recorded, which gave the technique the name torque mixing magnetic resonance spectroscopy (TMMRS). Attempts to repeat this experiment with a cantilever have failed so far, presumably because the origin of the cantilever signal can not exclusively be attributed to magnetic torque, but also to a force acting on the magnetic sample. This makes it impossible to distinguish between force and torque signals. In their experiment, Losby *et al.* used a different kind of torque sensor in the form of a paddle, doubly clamped to two elongated beams. This ensures that the dominant mode is of torsional type, which suppresses the contributions of a magnetic force signal.

Future magnetic torque magnetometry or torque mixing experiments can be optimized by designing paddle resonators according to the needs of the sample of interest. By embedding the sensor in the middle of a phononic band gap structure possibly reduces the mechanical noise and boosts the sensitivity, since no vibration is transferred to the resonator and also no energy can dissipate from the sensor in form of phonons. This specific design possibly also allows for electrical contact of the sample of interest, which could be of relevance for the emerging field of two-dimensional (2D) magnets.

2D magnets have emerged as a new frontier in magnetism, both in terms of fundamental questions – including why such magnetism is stable at all – as well as from the device engineering point of view. In general, the stacking, twisting, and combining of van der Waals (vdW) materials with control down to individual atomic layers has started a revolution in heterostructure engineering. Layer-by-layer control offers a multitude of possible material combinations, without constraints imposed by lattice mismatch, along with the prospect of making compact devices, in which large electric fields can easily be applied. These new tools give researchers unprecedented control of interactions and band structure, as exemplified by the 2018 realization of superconducting twisted bilayer graphene. In the realm of magnetism, these methods can be used to tune the magnetic properties of a material or even to make materials, which are non-magnetic in the bulk, magnetic in 2D. Most importantly, both in view of understanding the physics of 2D magnetism and exploiting it for applications, vdW engineering may allow us

to realize new and useful magnetic phases, which are only possible in 2D. In order to fully take advantage of these new developments, we must understand the role of anisotropy, disorder, inhomogeneity, and characteristic length-scales in 2D magnets and their heterostructures. Such investigations require sensitive local probes and techniques for measuring magnetism in small volumes. The possibility to measure individual flakes of 2D magnets make torque magnetometry a perfect candidate to provide these information, either by using a cantilever or customized paddle resonators.

7 Appendix

7.1 Mumax³ code used for simulations in chapter 2.3.2

The simulations in ch.(2.3.2) were carried out using the following code:

```
// Cantilever properties
fx := 3000;
fy := 3000;
fz := 3000;
kx := 50e-6;
ky := 50e-6;
kz := 50e-6;
le := 100e-6;

// Material redefinition: CoFeB
anisU = vector(1, 0, 0)
Kul = .5e6;
Aex = 28e-12;
Msat = 1035031;
alpha = 1; //Set to 1 if no temperature is involved, otherwise 0.007 for CoFeB

// Define geometry parameters
aaxis := 40;
baxis := 40;
caxis := 40;

// Define mesh (square!)
meshsize := 1.0;
SetCellsize(meshsize*1e-9, meshsize*1e-9, meshsize*1e-9);
SetGridsize(aaxis/meshsize - 0, baxis/meshsize + 0, caxis/meshsize + 0);
EdgeSmooth = 0;

// Set geometry
setgeom( ellipsoid(aaxis*1e-9, baxis*1e-9, caxis*1e-9) );

// Define direction of B_ext
phi := 1.0;
theta := 89.0;

// Tiltangles for cantilever oscillations
tiltx := 1.0;
tilty := 1.0;
tiltz := 1.0;
tiltmin := 0.4;
tiltmax := 1.0;

hx := cos(phi * pi/180)*sin(theta * pi/180);
hy := sin(phi * pi/180)*sin(theta * pi/180);
hz := cos(theta * pi/180);

// Tilt field and magnetizaion vector
hx_tiltx := cos(phi*pi/180) * sin(theta*pi/180)
hy_tiltx := -cos(theta*pi/180) * sin(tiltx*pi/180) + cos(tiltx*pi/180) * sin(theta*pi/180) * sin(phi*pi/180)
hz_tiltx := cos(tiltx*pi/180) * cos(theta*pi/180) + sin(tiltx*pi/180) * sin(theta*pi/180) * sin(phi*pi/180)

hx_tiltx_m := cos(phi*pi/180) * sin(theta*pi/180)
hy_tiltx_m := -cos(theta*pi/180) * sin(-tiltx*pi/180) + cos(-tiltx*pi/180) * sin(theta*pi/180) * sin(phi*pi/180)
hz_tiltx_m := cos(-tiltx*pi/180) * cos(theta*pi/180) + sin(-tiltx*pi/180) * sin(theta*pi/180) * sin(phi*pi/180)

hx_tilty := cos(theta*pi/180)*sin(tilty*pi/180) + cos(tilty*pi/180)*cos(phi*pi/180)*sin(theta*pi/180);
hy_tilty := sin(theta*pi/180) * sin(phi*pi/180);
hz_tilty := cos(tilty*pi/180)*cos(theta*pi/180) - cos(phi*pi/180)*sin(tilty*pi/180)*sin(theta*pi/180);

hx_tilty_m := cos(theta*pi/180)*sin(-tilty*pi/180) + cos(-tilty*pi/180)*cos(phi*pi/180)*sin(theta*pi/180);
hy_tilty_m := sin(theta*pi/180) * sin(phi*pi/180);
hz_tilty_m := cos(-tilty*pi/180)*cos(theta*pi/180) - cos(phi*pi/180)*sin(-tilty*pi/180)*sin(theta*pi/180);

hx_tiltz := cos((tiltz+phi)*pi/180)*sin(theta*pi/180)
hy_tiltz := sin(theta*pi/180)*sin((tiltz+phi)*pi/180)
hz_tiltz := cos(theta*pi/180)

hx_tiltz_m := cos((-tiltz+phi)*pi/180)*sin(theta*pi/180)
hy_tiltz_m := sin(theta*pi/180)*sin((-tiltz+phi)*pi/180)
hz_tiltz_m := cos(theta*pi/180)
```

```

// Amplitude of linear oscillation component for susceptibility measurement (%)
mag := 0.02;

// Definitions
OutputFormat=OVF2_TEXT;
MinimizerStop = 3e-6;

// Initialize values
sigB_abs := 1e-9;
E_total_tiltx_minus := 0e-15;
E_total_tiltx_plus := 0e-15;
E_total_tilty_minus := 0e-15;
E_total_tilty_plus := 0e-15;
E_total_tiltz_minus := 0e-15;
E_total_tiltz_plus := 0e-15;
E_total_mag_minus_x := 0e-15;
E_total_mag_plus_x := 0e-15;
E_total_mag_minus_y := 0e-15;
E_total_mag_plus_y := 0e-15;
E_total_mag_minus_z := 0e-15;
E_total_mag_plus_z := 0e-15;

// Standard properties
TableAdd(B_ext);
TableAddVar(sigB_abs, "signed absolute B", "T");
TableAdd(m_full);
TableAdd(geom);
TableAdd(MaxAngle);
TableAdd(E_anis);
TableAdd(E_demag);
TableAdd(E_exch);
TableAdd(E_Zeeman);
TableAdd(E_total);

// Additional properties

// Energies
TableAddVar(E_total_tiltx_plus, "E_total_tiltx_plus", "J");
TableAddVar(E_total_tiltx_minus, "E_total_tiltx_minus", "J");
TableAddVar(E_total_tilty_plus, "E_total_tilty_plus", "J");
TableAddVar(E_total_tilty_minus, "E_total_tilty_minus", "J");
TableAddVar(E_total_tiltz_plus, "E_total_tiltz_plus", "J");
TableAddVar(E_total_tiltz_minus, "E_total_tiltz_minus", "J");

// Frequency Shifts
TableAddVar(fx/(2*kx*le)*le*(E_total_tiltx_plus+E_total_tiltx_minus-2*E_total)/(tiltx*pi/180*tiltx*pi/180), "Dfx", "a.u.");
TableAddVar(fy/(2*ky*le)*le*(E_total_tilty_plus+E_total_tilty_minus-2*E_total)/(tilty*pi/180*tilty*pi/180), "Dfy", "a.u.");
TableAddVar(fz/(2*kz*le)*le*(E_total_tiltz_plus+E_total_tiltz_minus-2*E_total)/(tiltz*pi/180*tiltz*pi/180), "Dfz", "a.u.");

// Torques
TableAddVar((E_total_tiltx_plus-E_total_tiltx_minus)/(2*tiltx*pi/180), "xTorque", "a.u.");
TableAddVar((E_total_tilty_plus-E_total_tilty_minus)/(2*tilty*pi/180), "yTorque", "a.u.");
TableAddVar((E_total_tiltz_plus-E_total_tiltz_minus)/(2*tiltz*pi/180), "zTorque", "a.u.");

// Linear field components for suscetpibility, susceptibility and magnetization
TableAddVar(E_total_mag_plus_x, "E_total_mag_plus_x", "J");
TableAddVar(E_total_mag_minus_x, "E_total_mag_minus_x", "J");
TableAddVar((E_total_mag_plus_x+E_total_mag_minus_x-2*E_total)/(mag*sigB_abs*mag*sigB_abs), "xSusceptibility", "a.u.");
TableAddVar((E_total_mag_plus_x-E_total_mag_minus_x)/(2*mag*sigB_abs), "xMagnetization", "a.u.");

TableAddVar(E_total_mag_plus_y, "E_total_mag_plus_y", "J");
TableAddVar(E_total_mag_minus_y, "E_total_mag_minus_y", "J");
TableAddVar((E_total_mag_plus_y+E_total_mag_minus_y-2*E_total)/(mag*sigB_abs*mag*sigB_abs), "ySusceptibility", "a.u.");
TableAddVar((E_total_mag_plus_y-E_total_mag_minus_y)/(2*mag*sigB_abs), "yMagnetization", "a.u.");

TableAddVar(E_total_mag_plus_z, "E_total_mag_plus_z", "J");
TableAddVar(E_total_mag_minus_z, "E_total_mag_minus_z", "J");
TableAddVar((E_total_mag_plus_z+E_total_mag_minus_z-2*E_total)/(mag*sigB_abs*mag*sigB_abs), "zSusceptibility", "a.u.");
TableAddVar((E_total_mag_plus_z-E_total_mag_minus_z)/(2*mag*sigB_abs), "zMagnetization", "a.u.");

// Field angles
TableAddVar(theta, "Theta", "grad");
TableAddVar(phi, "Phi", "grad");

//Initial state
m = Uniform(hx, hy, hz);

//Hysteresis B in mT
Bstart := 2000;
Binter1 := 0;
Binter2 := 50;
Binter3 := 20;

Bstep1 := 100;
Bstep2 := 5;
Bstep3 := 5;

```

```

// Unit correction
unicor := 1000;

for B:=Bstart; B>=-Bstart; B-=Bstep1{
tiltx = tiltmin + tiltmax*abs(B)/Bstart;
tilty = tiltmin + tiltmax*abs(B)/Bstart;
tiltz = tiltmin + tiltmax*abs(B)/Bstart;

hx_tiltx = cos(phi*pi/180) * sin(theta*pi/180)
hy_tiltx = -cos(theta*pi/180) * sin(tiltx*pi/180) + cos(tiltx*pi/180) * sin(theta*pi/180) * sin(phi*pi/180)
hz_tiltx = cos(tiltx*pi/180) * cos(theta*pi/180) + sin(tiltx*pi/180) * sin(theta*pi/180) * sin(phi*pi/180)

hx_tiltx_m = cos(phi*pi/180) * sin(theta*pi/180)
hy_tiltx_m = -cos(theta*pi/180) * sin(-tiltx*pi/180) + cos(-tiltx*pi/180) * sin(theta*pi/180) * sin(phi*pi/180)
hz_tiltx_m = cos(-tiltx*pi/180) * cos(theta*pi/180) + sin(-tiltx*pi/180) * sin(theta*pi/180) * sin(phi*pi/180)

hx_tilty = cos(theta*pi/180)*sin(tilty*pi/180) + cos(tilty*pi/180)*cos(phi*pi/180)*sin(theta*pi/180);
hy_tilty = sin(theta*pi/180) * sin(phi*pi/180);
hz_tilty = cos(tilty*pi/180)*cos(theta*pi/180) - cos(phi*pi/180)*sin(tilty*pi/180)*sin(theta*pi/180);

hx_tilty_m = cos(theta*pi/180)*sin(-tilty*pi/180) + cos(-tilty*pi/180)*cos(phi*pi/180)*sin(theta*pi/180);
hy_tilty_m = sin(theta*pi/180) * sin(phi*pi/180);
hz_tilty_m = cos(-tilty*pi/180)*cos(theta*pi/180) - cos(phi*pi/180)*sin(-tilty*pi/180)*sin(theta*pi/180);

hx_tiltz = cos((tiltz+phi)*pi/180)*sin(theta*pi/180)
hy_tiltz = sin(theta*pi/180)*sin((tiltz+phi)*pi/180)
hz_tiltz = cos(theta*pi/180)

hx_tiltz_m = cos((-tiltz+phi)*pi/180)*sin(theta*pi/180)
hy_tiltz_m = sin(theta*pi/180)*sin((-tiltz+phi)*pi/180)
hz_tiltz_m = cos(theta*pi/180)

sigB_abs = B/unicor;

// Set fields, minimize energy, store result in corresponding variables
B_ext = vector(B/unicor * hx_tiltx, B/unicor * hy_tiltx, B/unicor * hz_tiltz);
minimize();
E_total_tiltx_plus = E_total;

B_ext = vector(B/unicor * hx + B/unicor * mag, B/unicor * hy, B/unicor * hz);
minimize();
E_total_mag_plus_x = E_total;

B_ext = vector(B/unicor * hx_tilty, B/unicor * hy_tilty, B/unicor * hz_tilty);
minimize();
E_total_tilty_plus = E_total;

B_ext = vector(B/unicor * hx, B/unicor * hy + B/unicor * mag, B/unicor * hz);
minimize();
E_total_mag_plus_y = E_total;

B_ext = vector(B/unicor * hx_tiltz, B/unicor * hy_tiltz, B/unicor * hz_tiltz);
minimize();
E_total_tiltz_plus = E_total;

B_ext = vector(B/unicor * hx, B/unicor * hy, B/unicor * hz + B/unicor * mag);
minimize();
E_total_mag_plus_z = E_total;

B_ext = vector(B/unicor * hx_tiltx_m, B/unicor * hy_tiltx_m, B/unicor * hz_tiltx_m);
minimize();
E_total_tiltx_minus = E_total;

B_ext = vector(B/unicor * hx - B/unicor * mag, B/unicor * hy, B/unicor * hz);
minimize();
E_total_mag_minus_x = E_total;

B_ext = vector(B/unicor * hx_tilty_m, B/unicor * hy_tilty_m, B/unicor * hz_tilty_m);
minimize();
E_total_tilty_minus = E_total;

B_ext = vector(B/unicor * hx, B/unicor * hy - B/unicor * mag, B/unicor * hz);
minimize();
E_total_mag_minus_y = E_total;

B_ext = vector(B/unicor * hx_tiltz_m, B/unicor * hy_tiltz_m, B/unicor * hz_tiltz_m);
minimize();
E_total_tiltz_minus = E_total;

B_ext = vector(B/unicor * hx, B/unicor * hy, B/unicor * hz - B/unicor * mag);
minimize();
E_total_mag_minus_z = E_total;

B_ext = vector(B/unicor * hx, B/unicor * hy, B/unicor * hz);
minimize();

// Save table values and magnetization
tablesave();
save(m);
};

```


8 Acknowledgements

This thesis is the result of a bit over five years of work. Naturally, this wouldn't have been possible without the help and supervision of several people, nor would it have been the amazing time it was without the group of people to not only work among, but also spend quite some time with apart of work. It's not only about the things we possibly achieve during a PhD, but also about the environment in which we learn and grow. With this being said, the sort-of final page in this document is dedicated to the people who formed said environment for me and whom i had the possibility to learn from.

First of all i would like to thank Prof. Martino Poggio for the opportunity to pursue my PhD in his group. It was an amazing experience in many regards but one of the main reasons for me is the way how you lead the group and the support, advice and flexibility you provide to people. I always had the feeling i could ask you basically anything and get an honest opinion and feedback on whatever i was coming up with. This went from ideas for measurements over any questions on physics to organization of events to broken micro-manipulators and burned amplifiers. Thank you for this, for your patience, the guidance and the overall great atmosphere inside and outside of the lab, on hikes, BBQs on the roof, at the Rhine, in the mountains, and even on the go kart track.

A special thank you also goes to Dr. Boris Gross. I learned so many things from you, that it would probably extend the volume of the thesis by quite some pages, if i would go through all of it here. Apart of all the practical stuff in the lab and for the simulations, what i'm most thankful for is that you taught me how to be relaxed when things are not working and how to get an understanding of when it's worth to go the extra mile and when it's probably not worth the effort, specially when i wouldn't see it. I heard the sentence "Trust me, i tried this, it's not going to work." more than once from you, and most of the time you were right about it. Thank you for everything, for your guidance, feedback, the patience to discuss things with me over and over again and the insight that conference talks are best edited last minute while having gin-tonic in a hotel room. Anytime again!

Thank you also to Dr. Andrea Mehlin, my predecessor on the DCM project who introduced me to the fine art of micromanipulation and showed me how to handle these quite delicate cantilevers. In the same run, also thanks to Mathias Claus, my successor on the project. I wish you all the best for the future, may you lead the project to new glory!

A big thank you of course is dedicated to all the present and former members of the PoggioLab that i had the pleasure to meet and also work with. I could literally write pages over pages here about stories of great times that would include things like catapults, fully automatic Nerf-guns and questionable UNO-sessions. As much as i want to write a small dedication to all of you, knowing myself, i might probably get pretty emotional or even forget someone^a, which i then would regret every time i hold this document in my hands, so let me just say: You guys are amazing! I couldn't have wished for a better group, thank you for everything, and i hope we will see each other soon and stay in touch.

^aMathias?

Nonetheless, i have one special mention, which is David Jaeger. Not only have we been working and studying together for years, we also tested our way through quite a stash of different whiskeys without getting tired of delivering our more or less sophisticated expertise on how strong the taste of grandma's old leather furniture is overwhelming the sweetness of dark fruit. You were also the first one who introduced said Nerf guns to the office, which lead to a general arming of the group. I will always admire your sheer effort to distribute almost around two hundred hand made anatomic drawings on Thorlabs sticky notes all over my desk while i was on vacation (i think i found the last of those only about 3 years later). Following your own wish, i will include you in my heritage for my whiskey selection and my beloved Nutella t-shirt, as a thank you for never getting tired to be a pain in my A. and if i ever get the chance to hire you, i'll let you work for me!

Apart from our group, i want to thank Claudia Wirth, the mastermind of all administrative matters for always providing a place to go for any such affairs, for your good mood and all the chats whenever we met. Also thanks to Sascha Martin and his team from the mechanical workshop. I guess without you, half the department's experiments would come apart soon.

Another thank you to Prof. Ernst Meyer, Prof. Mark Freeman and Prof. Patrick Maletinsky for being part of my PhD committee and hosting my defense.

From outside the institute, i would like to thank the members of the Nanoskyrmionics Sinergia project, mainly the PIs i was working most with, Prof. Dirk Grundler and Prof. Henrik Ronnow, as well as Dr. Jonathan White and Dr. Arnaud Magrez for providing a inspiring atmosphere during our regular meetings.

Special thanks here go to Ping Che and Anna Kukolova, my partners in crime when it came to organization of workshops, retreats and for shipping samples as well as local brewery products across switzerland. It was always great to work, celebrate, snowboard and play UNO with you!

There are of course more people that made the last few years what they were. First on this list is Dr. Mara Batzer. Like David, we studied (more or less) together and then joined the lab during my Master studies. We shared probably hectoliters of coffee while chatting about everything from science to motor bikes over the years. We should add more coffee to the score soon!

For sure next on this list is Dr. Olya Popova, a mountain-loving, snowboard addicted menace of beautifully brilliant chaotic energy. Whether it was swimming down the Rhine in summer or sliding down the mountains in winter, we spent a lot of time going downhill together. Our whatsapp history is probably the size of a 7 volume book series and was on some days only interrupted when we went for coffee/red bull breaks. The institute is for sure a lot quieter since you graduated but also a little bit less exciting.

I also want to say a big thank you to my friends from outside the university, some of which i have known from childhood on or as much as half my life and to all of my family and my second family. I'll tell you in person soon!

I want to mention specially my grandma Klara who was visiting my defense at the young age of 88 years, despite not understanding any word of English. Your quick wit and continued interest in any new things is very special and an inspiration to grow towards. It's been a long time from waving across the fence when we left kindergarten to listening to me presenting my defense talk and you've always been there. Thank you for all of it.^b

^bKasch dir dä Teil jo uff e rächtes Allemannisch übersetze loh, Oma.

Thank you again to my uncle and godfather Christian and my aunt Bettina, who are around for any major and minor life event since ever. Be it birthdays, getting my first (actually first and second) guitar, a wedding or now a defense, you always manage to make it a special experience.

A special place in the final part of this section is dedicated to my parents, who enabled all of this by always giving me the opportunity to follow my own path from a very early age on. I think you know how much i appreciate it all and that i might not have gotten far without your support. After being in an educational setting for almost 27 years now, i'm happy to inform you, i'm finally out of school!

The same holds true for my siblings. You always manage to lift me up, throw me down, balance me and put me in my place. All of it is absolutely wanted, appreciated and welcome even though it might seem you try to undermine my position as the oldest one from time to time :)

Last but definitely not least thank you to my wife Irina. Since 2013 you not only had my back at any time, encouraged me in every step and helped me to get through every stressful time, you also helped me grow as a person and open my mind to new perspectives. Thanks for sharing all this and building a wonderful, nerdy life full of popculture references, asian food, casual weirdness and medieval weapons with me. The best is yet to come and i'm absolutely excited for it!

So.

That's it.

It's done.

See you next time!

Basel, June 2022,

Simon Philipp

References

- [1] Deanna D. Stueber, Jake Villanova, Itzel Aponte, Zhen Xiao, and Vicki L. Colvin. “Magnetic Nanoparticles in Biology and Medicine: Past, Present, and Future Trends”. *Pharmaceutics*, **13**(7):943, June 2021. doi: 10.3390/pharmaceutics13070943.
- [2] D. Issadore, Y. I. Park, H. Shao, C. Min, K. Lee, M. Liang, R. Weissleder, and H. Lee. “Magnetic sensing technology for molecular analyses”. *Lab Chip*, **14**:2385–2397, 2014. doi: 10.1039/C4LC00314D.
- [3] Arno Ehresmann, Iris Koch, and Dennis Holzinger. “Manipulation of superparamagnetic beads on patterned exchange-bias layer systems for biosensing applications”. *Sensors*, **15**(11):28854–28888, 2015. doi: 10.3390/s151128854.
- [4] Brandon H. McNaughton, Karen A. Kehbein, Jeffrey N. Anker, and Raoul Kopelman. “Sudden breakdown in linear response of a rotationally driven magnetic microparticle and application to physical and chemical microsensing”. *The Journal of Physical Chemistry B*, **110**(38):18958–18964, 2006. doi: 10.1021/jp060139h.
- [5] Brandon H. McNaughton, Paivo Kinnunen, Miri Shlomi, Codrin Cionca, Shao Ning Pei, Roy Clarke, Panos Argyrakis, and Raoul Kopelman. “Experimental system for one-dimensional rotational brownian motion”. *The Journal of Physical Chemistry B*, **115**(18):5212–5218, 2011. doi: 10.1021/jp1072632.
- [6] Randall M. Erb, Joshua J. Martin, Rasam Soheilian, Chunzhou Pan, and Jabulani R. Barber. “Actuating Soft Matter with Magnetic Torque”. *Advanced Functional Materials*, **26**(22):3859–3880, 2016. doi: 10.1002/adfm.201504699.
- [7] Gabi Steinbach, Michael Schreiber, Dennis Nissen, Manfred Albrecht, Sibylle Gemming, and Artur Erbe. “Anisotropy of colloidal components propels field-activated stirrers and movers”. *Physical Review Research*, **2**(2):023092, April 2020. doi: 10.1103/PhysRevResearch.2.023092.
- [8] K. V. T. Nguyen and Jeffrey N. Anker. “Detecting de-gelation through tissue using magnetically modulated optical nanoprobe (MagMOONs)”. *Sensors and Actuators B: Chemical*, **205**:313–321, December 2014. doi: 10.1016/j.snb.2014.08.073.
- [9] L. Baraban, M. Tasinkevych, M. N. Popescu, S. Sanchez, S. Dietrich, and O. G. Schmidt. “Transport of cargo by catalytic Janus micro-motors”. *Soft Matter*, **8**(1):48–52, 2012. doi: 10.1039/C1SM06512B.
- [10] Leonardo F. Valadares, Yu-Guo Tao, Nicole S. Zacharia, Vladimir Kitaev, Fernando Galembeck, Raymond Kapral, and Geoffrey A. Ozin. “Catalytic Nanomotors: Self-Propelled Sphere Dimers”. *Small*, **6**(4):565–572, 2010. doi: <https://doi.org/10.1002/smll.200901976>.
- [11] Ramin Golestanian, Tanniemola B. Liverpool, and Armand Ajdari. “Propulsion of a Molecular Machine by Asymmetric Distribution of Reaction Products”. *Phys. Rev. Lett.*,

94(22):220801, June 2005. doi: 10.1103/PhysRevLett.94.220801.

- [12] Ugur Bozuyuk, Yunus Alapan, Amirreza Aghakhani, Muhammad Yunusa, and Metin Sitti. “Shape anisotropy-governed locomotion of surface microrollers on vessel-like microtopographies against physiological flows”. *Proceedings of the National Academy of Sciences*, **118**(13), March 2021. doi: 10.1073/pnas.2022090118.
- [13] H. Shokrollahi. “A review of the magnetic properties, synthesis methods and applications of maghemite”. *J. Magn. Magn. Mater.*, **426**:74–81, March 2017. doi: 10.1016/j.jmmm.2016.11.033.
- [14] Sheng Tong, Haibao Zhu, and Gang Bao. “Magnetic iron oxide nanoparticles for disease detection and therapy”. *Mater. Today*, **31**:86–99, December 2019. doi: 10.1016/j.mattod.2019.06.003.
- [15] R. Dronskowski. “The Little Maghemite Story: A Classic Functional Material”. *Adv. Funct. Mater.*, **11**(1):27–29, 2001. doi: 10.1002/1616-3028(200102)11:1(27::AID-ADFM27)3.0.CO;2-X.
- [16] R. L. Comstock. “Review Modern magnetic materials in data storage”. *Journal of Materials Science: Materials in Electronics*, **13**(9):509–523, September 2002. doi: 10.1023/A:1019642215245.
- [17] Stuart S. P. Parkin, Masamitsu Hayashi, and Luc Thomas. “Magnetic Domain-Wall Racetrack Memory”. *Science*, **320**(5873):190–194, April 2008. doi: 10.1126/science.1145799.
- [18] S. Mühlbauer, B. Binz, F. Jonietz, C. Pfleiderer, A. Rosch, A. Neubauer, R. Georgii, and P. Böni. “Skyrmion Lattice in a Chiral Magnet”. *Science*, **323**(5916):915–919, February 2009. doi: 10.1126/science.1166767.
- [19] X. Z. Yu, Y. Onose, N. Kanazawa, J. H. Park, J. H. Han, Y. Matsui, N. Nagaosa, and Y. Tokura. “Real-space observation of a two-dimensional skyrmion crystal”. *Nature*, **465**(7300):901–904, June 2010. doi: 10.1038/nature09124.
- [20] X. Z. Yu, N. Kanazawa, Y. Onose, K. Kimoto, W. Z. Zhang, S. Ishiwata, Y. Matsui, and Y. Tokura. “Near room-temperature formation of a skyrmion crystal in thin-films of the helimagnet FeGe”. *Nat. Mater.*, **10**(2):106–109, February 2011. doi: 10.1038/nmat2916.
- [21] Haifeng Du, Renchao Che, Lingyao Kong, Xuebing Zhao, Chiming Jin, Chao Wang, Jiyong Yang, Wei Ning, Runwei Li, Changqing Jin, Xianhui Chen, Jiadong Zang, Yuheng Zhang, and Mingliang Tian. “Edge-mediated skyrmion chain and its collective dynamics in a confined geometry”. *Nat. Commun.*, **6**:8504, October 2015. doi: 10.1038/ncomms9504.
- [22] Y. Tokunaga, X. Z. Yu, J. S. White, H. M. Rønnow, D. Morikawa, Y. Taguchi, and Y. Tokura. “A new class of chiral materials hosting magnetic skyrmions beyond room temperature”. *Nat. Commun.*, **6**:7638, July 2015. doi: 10.1038/ncomms8638.
- [23] T. Schulz, R. Ritz, A. Bauer, M. Halder, M. Wagner, C. Franz, C. Pfleiderer, K. Everschor, M. Garst, and A. Rosch. “Emergent electrodynamics of skyrmions in a chiral magnet”. *Nat. Phys.*, **8**(4):301–304, April 2012. doi: 10.1038/nphys2231.
- [24] F. Jonietz, S. Mühlbauer, C. Pfleiderer, A. Neubauer, W. Münzer, A. Bauer, T. Adams, R. Georgii, P. Böni, R. A. Duine, K. Everschor, M. Garst, and A. Rosch. “Spin Transfer

- Torques in MnSi at Ultralow Current Densities”. *Science*, **330**(6011):1648–1651, December 2010. doi: 10.1126/science.1195709.
- [25] Pin-Jui Hsu, André Kubetzka, Aurore Finco, Niklas Romming, Kirsten von Bergmann, and Roland Wiesendanger. “Electric-field-driven switching of individual magnetic skyrmions”. *Nat. Nanotechnol.*, **12**(2):123–126, February 2017. doi: 10.1038/nnano.2016.234.
- [26] E. Ruff, A. Butykai, K. Geirhos, S. Widmann, V. Tsurkan, E. Stefanet, I. Kézsmárki, A. Loidl, and P. Lunkenheimer. “Polar and magnetic order in GaV_4S_8 ”. *Phys. Rev. B*, **96**(16):165119, October 2017. doi: 10.1103/PhysRevB.96.165119.
- [27] Y. Fujima, N. Abe, Y. Tokunaga, and T. Arima. “Thermodynamically stable skyrmion lattice at low temperatures in a bulk crystal of lacunar spinel GaV_4S_8 ”. *Phys. Rev. B*, **95**(18):180410, May 2017. doi: 10.1103/PhysRevB.95.180410.
- [28] J. Sampaio, V. Cros, S. Rohart, A. Thiaville, and A. Fert. “Nucleation, stability and current-induced motion of isolated magnetic skyrmions in nanostructures”. *Nat. Nanotechnol.*, **8**(11):839–844, November 2013. doi: 10.1038/nnano.2013.210.
- [29] R. Tomasello, E. Martinez, R. Zivieri, L. Torres, M. Carpentieri, and G. Finocchio. “A strategy for the design of skyrmion racetrack memories”. *Sci. Rep.*, **4**:6784, October 2014. doi: 10.1038/srep06784.
- [30] A. C. Bleszynski-Jayich, W. E. Shanks¹, B. Peaudecerf, E. Ginossar¹, F. von Oppen, L. Glazman, and J. G. E. Harris. “Persistent currents in normal metal rings”. *Science*, **326**(5950):272–275, 2009. doi: <https://doi.org/10.1126/science.1178139>.
- [31] B. Gross, D. P. Weber, D. Ruffer, A. Buchter, F. Heimbach, A. Fontcuberta i Morral, D. Grundler, and M. Poggio. “Dynamic cantilever magnetometry of individual CoFeB nanotubes”. *Phys. Rev. B*, **93**(6):064409, February 2016. doi: 10.1103/PhysRevB.93.064409.
- [32] K. A. Modic, Maja D. Bachmann, B. J. Ramshaw, F. Arnold, K. R. Shirer, Amelia Estry, J. B. Betts, Nirmal J. Ghimire, E. D. Bauer, Marcus Schmidt, Michael Baenitz, E. Svanidze, Ross D. McDonald, Arkady Shekhter, and Philip J. W. Moll. “Resonant torsion magnetometry in anisotropic quantum materials”. *Nat. Commun.*, **9**(1):3975, September 2018. doi: 10.1038/s41467-018-06412-w.
- [33] A. Mehlin, F. Xue, D. Liang, H. F. Du, M. J. Stolt, S. Jin, M. L. Tian, and M. Poggio. “Stabilized Skyrmion Phase Detected in MnSi Nanowires by Dynamic Cantilever Magnetometry”. *Nano Lett.*, **15**(7):4839–4844, July 2015. doi: 10.1021/acs.nanolett.5b02232.
- [34] Albert Einstein and Wander Johannes de Haas. “Experimenteller Nachweis der Ampèreschen Molekularströme”. *Deutsche Physikalische Gesellschaft*, **17**:152–170, January 1915.
- [35] O. W. Richardson. “A mechanical effect accompanying magnetization”. March 1908. doi: 10.1103/physrevseriesi.26.248.
- [36] Naturforschende Gesellschaft in Zürich. “Vierteljahrsschrift der naturforschenden gesellschaft in zürich.”. **v.63 (1919)**:116–186, 1918.
- [37] D. S. Miller. “A recording torque magnetometer”. *Review of Scientific Instruments*, **21**(7):605–607, 1950. doi: 10.1063/1.1745665.

- [38] Björn Westerstrandh, Uno Gäfvert, and Leif Lundgren. “A torque magnetometer with proportional-integrating-differentiating (PID) compensation”. *Physica Scripta*, **14**(1-2): 5–10, jul 1976. doi: 10.1088/0031-8949/14/1-2/001.
- [39] J. P. Eisenstein. “High-precision torsional magnetometer: Application to two-dimensional electron systems”. *Applied Physics Letters*, **46**(7):695–696, 1985. doi: 10.1063/1.95478.
- [40] M. Tokumoto, A.G. Swanson, J.S. Brooks, C.C. Agosta, S.T. Hannahs, N. Kinoshita, H. Anzai, M. Tamura, H. Tajima, H. Kuroda, A. Ugawa, and K. Yakushi. “Magnetic quantum oscillations in low-dimensional organic conductors (bedt-ttf)₂x”. *Physica B: Condensed Matter*, **184**(1):508–512, 1993. doi: [https://doi.org/10.1016/0921-4526\(93\)90406-V](https://doi.org/10.1016/0921-4526(93)90406-V).
- [41] C. Rossel, P. Bauer, D. Zech, J. Hofer, M. Willemin, and H. Keller. “Active microlevers as miniature torque magnetometers”. *Journal of Applied Physics*, **79**(11):8166–8173, 1996. doi: 10.1063/1.362550.
- [42] D. Weber. *Dynamic Cantilever Magnetometry of Individual Ferromagnetic Nanotubes*. PhD thesis, University of Basel, 2014.
- [43] A. Buchter. *Hybrid torque and SQUID magnetometry of individual magnetic nanotubes*. PhD thesis, University of Basel, 2015.
- [44] A. Mehlin. *Dynamic Cantilever Magnetometry of Reversal Processes and Phase Transitions in Individual Nanomagnets*. PhD thesis, University of Basel, 2017.
- [45] D. Rugar, H. J. Mamin, and P. Guethner. “Improved fiber-optic interferometer for atomic force microscopy”. *Appl. Phys. Lett.*, **55**(25):2588–2590, December 1989. doi: 10.1063/1.101987.
- [46] B. Gross, S. Philipp, K. Geirhos, A. Mehlin, S. Bordács, V. Tsurkan, A. Leonov, I. Kézsmárki, and M. Poggio. “Stability of néel-type skyrmion lattice against oblique magnetic fields in gav4s8 and gav4se8”. *Physical Review B*, **102**(10):104407, September 2020. doi: 10.1103/PhysRevB.102.104407.
- [47] Claas Abert. “Spintronics in micromagnetics”. *Handbook of Materials Modeling: Methods: Theory and Modeling*, pages 985–1008, 2020.
- [48] Helmut Kronmüller. “General micromagnetic theory and applications”. *Materials Science and Technology*, pages 1–43, 2006.
- [49] P. Weiss. *Materials Science and Technology*, pages 661–690, 1907.
- [50] Heinrich Barkhausen. “Zwei mit hilfe der neuen verstärker entdeckte erscheinungen”. *Phys. Z.*, **20**(17):401–403, 1919.
- [51] Francis Bitter. “Experiments on the nature of ferromagnetism”. *Phys. Rev.*, **41**:507–515, Aug 1932. doi: 10.1103/PhysRev.41.507.
- [52] KJ Sixtus and L Tonks. “Propagation of large barkhausen discontinuities”. *Physical Review*, **37**(8):930, 1931.
- [53] William Fuller Brown Jr. “Theory of the approach to magnetic saturation”. *Physical Review*, **58**(8):736, 1940.

- [54] William Fuller Brown Jr. “The effect of dislocations on magnetization near saturation”. *Physical Review*, **60**(2):139, 1941.
- [55] C. Kittel and J.K. Galt. “Ferromagnetic domain theory”. volume 3 of *Solid State Physics*, pages 437–564. Academic Press, 1956. doi: [https://doi.org/10.1016/S0081-1947\(08\)60136-8](https://doi.org/10.1016/S0081-1947(08)60136-8). URL <https://www.sciencedirect.com/science/article/pii/S0081194708601368>.
- [56] Lukas Exl, Dieter Suess, and Thomas Schrefl. “Micromagnetism”. In Michael Coey and Stuart Parkin, editors, *Handbook of Magnetism and Magnetic Materials*, pages 1–44. Springer International Publishing, Cham, 2020. ISBN 978-3-030-63101-7. doi: 10.1007/978-3-030-63101-7_7-1. URL https://doi.org/10.1007/978-3-030-63101-7_7-1.
- [57] E. C. STONER and E. P. WOHLFARTH. “Interpretation of High Coercivity in Ferromagnetic Materials”. *Nature*, **160**(4071):650–651, November 1947. doi: 10.1038/160650a0.
- [58] Allan H. Morrish. *The Physical Principles of Magnetism*. Wiley, January 2001. ISBN 978-0-7803-6029-7.
- [59] R.A. McCurrie. *Ferromagnetic Materials: Structure and Properties*. World Folklore Series; 3. Academic, 1994. ISBN 9780124824959. URL <https://books.google.ch/books?id=q-xSAAAAMAAJ>.
- [60] Amikam Aharoni. *Introduction to the Theory of Ferromagnetism*. Oxford University Press, 2000. ISBN 978-0-19-850809-0.
- [61] Amikam Aharoni. “Demagnetizing factors for rectangular ferromagnetic prisms”. *Journal of Applied Physics*, **83**(6):3432–3434, March 1998. doi: 10.1063/1.367113.
- [62] J. A. Osborn. “Demagnetizing factors of the general ellipsoid”. *Phys. Rev.*, **67**:351–357, Jun 1945. doi: 10.1103/PhysRev.67.351.
- [63] D.-X Chen, Enric Pardo, and Alvaro Sanchez. “Demagnetizing factors for rectangular prisms”. *Magnetics, IEEE Transactions on*, **41**:2077 – 2088, 07 2005. doi: 10.1109/TMAG.2005.847634.
- [64] J. Šoltýs, J. Feilhauer, I. Vetrova, J. Tóbiš, K. Bublikov, T. Ščepka, J. Fedor, J. Dérier, and V. Cambel. “Magnetic-field imaging using vortex-core MFM tip”. *Applied Physics Letters*, **116**(24):242406, June 2020. doi: 10.1063/5.0010623.
- [65] J.-P. Tetienne, T. Hingant, L. Rondin, S. Rohart, A. Thiaville, J.-F. Roch, and V. Jacques. “Quantitative stray field imaging of a magnetic vortex core”. *Physical Review B*, **88**(21):214408, December 2013. doi: 10.1103/PhysRevB.88.214408.
- [66] M. S. Wolf R. Badea and J. Berezovsky. “Exploiting bistable pinning of a ferromagnetic vortex for nitrogen-vacancy spin control”. *Applied Physics Letters*, **109**(13):132403, September 2016. doi: 10.1063/1.4963670.
- [67] Feng Guo, L. M. Belova, and R. D. McMichael. “Spectroscopy and Imaging of Edge Modes in Permalloy Nanodisks”. *Phys. Rev. Lett.*, **110**(1):017601, January 2013. doi: 10.1103/PhysRevLett.110.017601.
- [68] B. Pigeau, C. Hahn, G. de Loubens, V. V. Naletov, O. Klein, K. Mitsuzuka, D. Lacour, M. Hehn, S. Andrieu, and F. Montaigne. “Measurement of the Dynami-

cal Dipolar Coupling in a Pair of Magnetic Nanodisks Using a Ferromagnetic Resonance Force Microscope”. *Physical Review Letters*, **109**(24), December 2012. doi: 10.1103/PhysRevLett.109.247602.

- [69] V. Castel, J. Ben Youssef, F. Boust, R. Weil, B. Pigeau, G. de Loubens, V. V. Naletov, O. Klein, and N. Vukadinovic. “Perpendicular ferromagnetic resonance in soft cylindrical elements: Vortex and saturated states”. *Phys. Rev. B*, **85**(18):184419, May 2012. doi: 10.1103/PhysRevB.85.184419.
- [70] O. Klein, G. de Loubens, V. V. Naletov, F. Boust, T. Guillet, H. Hurdequint, A. Leksikov, A. N. Slavin, V. S. Tiberkevich, and N. Vukadinovic. “Ferromagnetic resonance force spectroscopy of individual submicron-size samples”. *Phys. Rev. B*, **78**(14):144410, October 2008. doi: 10.1103/PhysRevB.78.144410.
- [71] R. Badea, J. A. Frey, and J. Berezovsky. “Magneto-optical imaging of vortex domain deformation in pinning sites”. *Journal of Magnetism and Magnetic Materials*, **381**:463–469, May 2015. doi: 10.1016/j.jmmm.2015.01.036.
- [72] S. Philipp, B. Gross, M. Reginka, M. Merkel, M. M. Claus, M. Sulliger, A. Ehresmann, and M. Poggio. “Magnetic hysteresis of individual Janus particles with hemispherical exchange biased caps”. *Applied Physics Letters*, **119**(22):222406, 2021. doi: 10.1063/5.0076116.
- [73] J. Leliaert, J. Mulkers, J. De Clercq, A. Coene, M. Dvornik, and B. Van Waeyenberge. “Adaptively time stepping the stochastic Landau-Lifshitz-Gilbert equation at nonzero temperature: Implementation and validation in MuMax3”. *AIP Advances*, **7**(12):125010, 2017. doi: 10.1063/1.5003957.
- [74] J. Leliaert, M. Dvornik, J. Mulkers, J. De Clercq, M. V. Milošević, and B. Van Waeyenberge. “Fast micromagnetic simulations on GPU—recent advances made with $\text{\textbackslashtextdollar\textbackslashtextbackslashmathsf\$\lbrace\$\mumax\$\rbrace\$\^3\textdollar}$ ”. *Journal of Physics D: Applied Physics*, **51**(12):123002, February 2018. doi: 10.1088/1361-6463/aaab1c.
- [75] Arne Vansteenkiste, Jonathan Leliaert, Mykola Dvornik, Mathias Helsen, Felipe Garcia-Sanchez, and Bartel Van Waeyenberge. “The design and verification of MuMax3”. *AIP Advances*, **4**(10):107133, October 2014. doi: 10.1063/1.4899186.
- [76] Eckart Kneller, Alfred Seeger, and Helmut Kronmüller. “Ferromagnetismus”. In *Ferromagnetismus: Mit einem Beitrag Quantentheorie und Elektronentheorie des Ferromagnetismus*, pages 30–37. Springer Berlin Heidelberg, Berlin, Heidelberg, 1962. ISBN 978-3-642-86695-1. doi: 10.1007/978-3-642-86695-1_4. URL https://doi.org/10.1007/978-3-642-86695-1_4.
- [77] A. Mehlin, B. Gross, M. Wyss, T. Schefer, G. Tütüncüoğlu, F. Heimbach, A. Fontcuberta i Morral, D. Grundler, and M. Poggio. “Observation of end-vortex nucleation in individual ferromagnetic nanotubes”. *Phys. Rev. B*, **97**(13):134422, April 2018. doi: 10.1103/PhysRevB.97.134422.
- [78] Nicholas Kurti. *Selected Works of Louis Neel*. CRC Press, December 2019. ISBN 978-1-00-071415-9.

- [79] B. Gross, S. Philipp, E. Josten, J. Leliaert, E. Wetterskog, L. Bergström, and M. Poggio. “Magnetic anisotropy of individual maghemite mesocrystals”. *Phys. Rev. B*, **103**:014402, Jan 2021. doi: 10.1103/PhysRevB.103.014402.
- [80] J. L. García-Palacios. “On the Statics and Dynamics of Magnetoanisotropic Nanoparticles”. *Advances in Chemical Physics*, pages 1–210, March 2007. doi: 10.1002/9780470141717.ch1.
- [81] Challa S.S.R. Kumar. *Magnetic Characterization Techniques for Nanomaterials*. 2017.
- [82] David E. Laughlin. “Magnetic Transformations and Phase Diagrams”. *Metallurgical and Materials Transactions A*, **50**(6):2555–2569, June 2019. doi: 10.1007/s11661-019-05214-z.
- [83] Gregg Jaeger. “The Ehrenfest Classification of Phase Transitions: Introduction and Evolution”. *Archive for History of Exact Sciences*, **53**(1):51–81, May 1998. doi: 10.1007/s004070050021.
- [84] P. Ehrenfest. “Phasenumwandlungen im ueblichen und erweiterten sinn, classifiziert nach dem entsprechenden singularitaeten des thermodynamischen potentiales.”. *Verhandlungen der Koninklijke Akademie van Wetenschappen (Amsterdam)*, (36):53–157.
- [85] A. B. Pippard. “The Elements of Classical Thermodynamics”. *American Journal of Physics*, **26**(9):651–652, 1958. doi: 10.1119/1.1934738.
- [86] Lev Davidovich Landau and Evgenii Mikhailovich Lifshitz. *Statistical Physics: Volume 5*. Elsevier, 2013.
- [87] R. A. Swalin. *Thermodynamics of solids*. Elsevier, 1962.
- [88] B. Lebech, P. Harris, J. Skov Pedersen, K. Mortensen, C. I. Gregory, N. R. Bernhoeft, M. Jermy, and S. A. Brown. “Magnetic phase diagram of MnSi”. *Journal of Magnetism and Magnetic Materials*, **140-144**:119–120, 1995. doi: [https://doi.org/10.1016/0304-8853\(94\)01115-X](https://doi.org/10.1016/0304-8853(94)01115-X).
- [89] A. Bauer and C. Pfleiderer. “Magnetic phase diagram of MnSi inferred from magnetization and ac susceptibility”. *Phys. Rev. B*, **85**(21):214418, June 2012. doi: 10.1103/PhysRevB.85.214418.
- [90] Q A Pankhurst, J Connolly, S K Jones, and J Dobson. “Applications of magnetic nanoparticles in biomedicine”. *Journal of Physics D: Applied Physics*, **36**(13):R167–R181, jun 2003. doi: 10.1088/0022-3727/36/13/201.
- [91] Alessandro Chiolerio and Paolo Allia. “Magnetic Nanostructures and Spintronics”. In Bharat Bhushan, editor, *Encyclopedia of Nanotechnology*, pages 1248–1256. Springer Netherlands, Dordrecht, 2012. ISBN 978-90-481-9751-4. doi: 10.1007/978-90-481-9751-4_238. URL https://doi.org/10.1007/978-90-481-9751-4_238.
- [92] W. H. Meiklejohn and C. P. Bean. “New Magnetic Anisotropy”. *Physical Review*, **105**(3):904–913, February 1957. doi: 10.1103/PhysRev.105.904.
- [93] J Nogués and Ivan K Schuller. “Exchange bias”. *Journal of Magnetism and Magnetic Materials*, **192**(2):203–232, February 1999. doi: 10.1016/S0304-8853(98)00266-2.
- [94] R L Stamps. “Mechanisms for exchange bias”. *Journal of Physics D: Applied Physics*, **34**(3):444–444, jan 2001. doi: 10.1088/0022-3727/34/3/501.

- [95] Robert Streubel, Volodymyr P. Kravchuk, Denis D. Sheka, Denys Makarov, Florian Kronast, Oliver G. Schmidt, and Yuri Gaididei. “Equilibrium magnetic states in individual hemispherical permalloy caps”. *Applied Physics Letters*, **101**(13):132419, September 2012. doi: 10.1063/1.4756708.
- [96] J. Nogués, J. Sort, V. Langlais, V. Skumryev, S. Suriñach, J. S. Muñoz, and M. D. Baró. “Exchange bias in nanostructures”. *Physics Reports*, **422**(3):65–117, December 2005. doi: 10.1016/j.physrep.2005.08.004.
- [97] Maximilian Merkel, Rico Huhnstock, Meike Reginka, Dennis Holzinger, Michael Vogel, Arno Ehresmann, Jonas Zehner, and Karin Leistner. “Interrelation between polycrystalline structure and time-dependent magnetic anisotropies in exchange-biased bilayers”. *Physical Review B*, **102**(14):144421, October 2020. doi: 10.1103/PhysRevB.102.144421.
- [98] Manh-Huong Phan, Javier Alonso, Hafsa Khurshid, Paula Lampen-Kelley, Sayan Chandra, Kristen Stojak Repa, Zohreh Nemati, Raja Das, Óscar Iglesias, and Hariharan Srikanth. “Exchange Bias Effects in Iron Oxide-Based Nanoparticle Systems”. *Nanomaterials*, **6**(11):221, November 2016. doi: 10.3390/nano6110221.
- [99] Eran Maniv, Ryan A. Murphy, Shannon C. Haley, Spencer Doyle, Caolan John, Ariel Maniv, Sanath K. Ramakrishna, Yun-Long Tang, Peter Ercius, Ramamoorthy Ramesh, Arneil P. Reyes, Jeffrey R. Long, and James G. Analytis. “Exchange bias due to coupling between coexisting antiferromagnetic and spin-glass orders”. *Nature Physics*, **17**(4):525–530, April 2021. doi: 10.1038/s41567-020-01123-w.
- [100] A. Buchter, R. Wölbing, M. Wyss, O. F. Kieler, T. Weimann, J. Kohlmann, A. B. Zorin, D. Ruffer, F. Matteini, G. Tütüncüoğlu, F. Heimbach, A. Kleibert, A. Fontcuberta i Morral, D. Grundler, R. Kleiner, D. Koelle, and M. Poggio. “Magnetization reversal of an individual exchange-biased permalloy nanotube”. *Phys. Rev. B*, **92**(21):214432, December 2015. doi: 10.1103/PhysRevB.92.214432.
- [101] Amitesh Paul, C. Schmidt, N. Paul, A. Ehresmann, Stefan Mattauch, and Peter Böni. “Symmetric magnetization reversal in polycrystalline exchange coupled systems via simultaneous processes of coherent rotation and domain nucleation”. *Phys. Rev. B*, **86**:094420, Sep 2012. doi: 10.1103/PhysRevB.86.094420.
- [102] Jonas De Clercq, Arne Vansteenkiste, Medjid Abes, Kristiaan Temst, and Bartel Van Waeyenberge. “Modelling exchange bias with MuMax3”. *Journal of Physics D: Applied Physics*, **49**(43):435001, September 2016. doi: 10.1088/0022-3727/49/43/435001.
- [103] Wei Pan, Nai-Yeou Jih, Chien-Cheng Kuo, and Minn-Tsong Lin. “Coercivity enhancement near blocking temperature in exchange biased fe-fexmn-1-x films on cu(001)”. *Journal of Applied Physics*, **95**(11):7297–7299, 2004. doi: 10.1063/1.1652415.
- [104] R. Micheletto, H. Fukuda, and M. Ohtsu. “A simple method for the production of a two-dimensional, ordered array of small latex particles”. *Langmuir*, **11**(9):3333–3336, 1995. doi: 10.1021/la00009a012.
- [105] Andreea Tomita, Meike Reginka, Rico Huhnstock, Maximilian Merkel, Dennis Holzinger, and Arno Ehresmann. “Magnetic textures in hemispherical thin film caps with in-plane exchange bias”. *Journal of Applied Physics*, **129**(1):015305, January 2021. doi: 10.1063/5.0033772.

- [106] COMSOL AB. “Comsol multiphysics®”, 2021. URL <http://www.comsol.com>.
- [107] A. Mourkas, A. Zarlaha, N. Kourkoulis, and I. Panagiotopoulos. “Curvature induced stabilization of vortices on magnetic spherical sector shells”. *Journal of Magnetism and Magnetic Materials*, **524**:167676, April 2021. doi: 10.1016/j.jmmm.2020.167676.
- [108] D. V. Berkov, C. T. Boone, and I. N. Krivorotov. “Micromagnetic simulations of magnetization dynamics in a nanowire induced by a spin-polarized current injected via a point contact”. *Physical Review B*, **83**(5):054420, February 2011. doi: 10.1103/PhysRevB.83.054420.
- [109] J. M. D. Coey. *Magnetism and Magnetic Materials*. Cambridge University Press, March 2010. ISBN 978-0-521-81614-4.
- [110] A. Hubert and R. Schäfer. *Magnetic Domains: The Analysis of Magnetic Microstructures*. 1998.
- [111] N. Rossi, B. Gross, F. Dirnberger, D. Bougeard, and M. Poggio. “Magnetic force sensing using a self-assembled nanowire”. *Nano Letters*, **19**(2):930–936, 2019. doi: 10.1021/acs.nanolett.8b04174.
- [112] Jongnam Park, Kwangjin An, Yosun Hwang, Je-Geun Park, Han-Jin Noh, Jae-Young Kim, Jae-Hoon Park, Nong-Moon Hwang, and Taeghwan Hyeon. “Ultra-large-scale syntheses of monodisperse nanocrystals”. *Nat. Mater.*, **3**(12):891–895, December 2004. doi: 10.1038/nmat1251.
- [113] Erik Wetterskog, Michael Agthe, Arnaud Mayence, Jekabs Grins, Dong Wang, Subhasis Rana, Anwar Ahniyaz, German Salazar-Alvarez, and Lennart Bergström. “Precise control over shape and size of iron oxide nanocrystals suitable for assembly into ordered particle arrays”. *Sci. Technol. Adv. Mater.*, **15**(5):055010, October 2014. doi: 10.1088/1468-6996/15/5/055010.
- [114] Sabrina Disch. *The spin structure of magnetic nanoparticles and in magnetic nanostructures*. PhD thesis, RWTH Aachen University, 2010.
- [115] Lennart Häggström, Saeed Kamali, Tore Ericsson, Per Nordblad, Anwar Ahniyaz, and Lennart Bergström. “Mössbauer and magnetization studies of iron oxide nanocrystals”. *Hyperfine Interact.*, **183**(1):49–53, April 2008. doi: 10.1007/s10751-008-9750-5.
- [116] Elisabeth Josten, Manuel Angst, Artur Glavic, Paul Zakalek, Ulrich Rücker, Oliver H. Seeck, András Kovács, Erik Wetterskog, Emmanuel Kentzinger, Rafal E. Dunin-Borkowski, Lennart Bergström, and Thomas Brückel. “Strong size selectivity in the self-assembly of rounded nanocubes into 3D mesocrystals”. *Nanoscale Horiz.*, June 2020. doi: 10.1039/D0NH00117A.
- [117] Erik Wetterskog, Alice Klapper, Sabrina Disch, Elisabeth Josten, Raphaël P. Hermann, Ulrich Rücker, Thomas Brückel, Lennart Bergström, and German Salazar-Alvarez. “Tuning the structure and habit of iron oxide mesocrystals”. *Nanoscale*, **8**(34):15571–15580, 2016. doi: 10.1039/C6NR03776C.
- [118] S. Disch, R. P. Hermann, E. Wetterskog, A. A. Podlesnyak, K. An, T. Hyeon, G. Salazar-Alvarez, L. Bergström, and Th. Brückel. “Spin excitations in cubic maghemite nanoparticles studied by time-of-flight neutron spectroscopy”. *Phys. Rev. B*, **89**(6):064402, February 2014. doi: 10.1103/PhysRevB.89.064402.

- [119] Erik Wetterskog, Christian Jonasson, Detlef-M. Smilgies, Vincent Schaller, Christer Johansson, and Peter Svedlindh. “Colossal Anisotropy of the Dynamic Magnetic Susceptibility in Low-Dimensional Nanocube Assemblies”. *ACS Nano*, **12**(2):1403–1412, February 2018. doi: 10.1021/acsnano.7b07745.
- [120] C. Phatak, R. Pokharel, M. Beleggia, and M. De Graef. “On the magnetostatics of chains of magnetic nanoparticles”. *J. Magn. Magn. Mater.*, **323**(22):2912–2922, November 2011. doi: 10.1016/j.jmmm.2011.06.058.
- [121] L. A. Chekanova, E. A. Denisova, Roman N. Yaroslavtsev, S. V. Komogortsev, D. A. Velikanov, A. M. Zhizhaev, and R. S. Iskhakov. “Micro Grid Frame of Electroless Deposited Co-P Magnetic Tubes”. *Solid State Phenomena*, **233-234**:64–67, 2015. doi: 10.4028/www.scientific.net/SSP.233-234.64.
- [122] J. B. Birks. “The Properties of Ferromagnetic Compounds at Centimetre Wavelengths”. *Proc. Phys. Soc. B*, **63**(2):65–74, February 1950. doi: 10.1088/0370-1301/63/2/301.
- [123] Humihiko Takei and Shū Chiba. “Vacancy Ordering in Epitaxially-Grown Single Crystals of γ -Fe₂O₃”. *J. Phys. Soc. Jpn.*, **21**(7):1255–1263, July 1966. doi: 10.1143/JPSJ.21.1255.
- [124] H. Kachkachi and E. Bonet. “Surface-induced cubic anisotropy in nanomagnets”. *Phys. Rev. B*, **73**(22):224402, June 2006. doi: 10.1103/PhysRevB.73.224402.
- [125] D. A. Garanin and H. Kachkachi. “Surface Contribution to the Anisotropy of Magnetic Nanoparticles”. *Phys. Rev. Lett.*, **90**(6):065504, February 2003. doi: 10.1103/PhysRevLett.90.065504.
- [126] R. Yanes, O. Chubykalo-Fesenko, H. Kachkachi, D. A. Garanin, R. Evans, and R. W. Chantrell. “Effective anisotropies and energy barriers of magnetic nanoparticles with néel surface anisotropy”. *Phys. Rev. B*, **76**(6):064416, August 2007. doi: 10.1103/PhysRevB.76.064416.
- [127] D.L. Atherton and J.R. Beattie. “A mean field Stoner-Wohlfarth hysteresis model”. *IEEE Trans. Magn.*, **26**(6):3059–3063, November 1990. doi: 10.1109/20.102891.
- [128] Leïla Rebbouh, Raphaël P. Hermann, Fernande Grandjean, Taeghwan Hyeon, Kwangjin An, Alex Amato, and Gary J. Long. “⁵⁷Fe mössbauer spectral and muon spin relaxation study of the magnetodynamics of monodispersed γ – Fe₂O₃ nanoparticles”. *Phys. Rev. B*, **76**(17):174422, November 2007. doi: 10.1103/PhysRevB.76.174422.
- [129] Subhankar Bedanta and Wolfgang Kleemann. “Supermagnetism”. *J. Phys. D: Appl. Phys.*, **42**(1):013001, December 2008. doi: 10.1088/0022-3727/42/1/013001.
- [130] M.S. Andersson. *Interacting Magnetic Nanosystems - An Experimental Study of Super-spin Glasses*. PhD thesis, Uppsala Universitet, 2017.
- [131] B. Martínez, X. Obradors, Ll. Balcells, A. Rouanet, and C. Monty. “Low temperature surface spin-glass transition in γ -Fe₂O₃ nanoparticles”. *Phys. Rev. Lett.*, **80**(1):181–184, January 1998. doi: 10.1103/PhysRevLett.80.181.
- [132] Juan A. Ramos-Guivar, A. C. Krohling, Elvis O. López, F. Jochen Litterst, and E. C. Passamani. “Superspinglass behavior of maghemite nanoparticles dispersed in mesoporous silica”. *J. Magn. Magn. Mater.*, **485**:142–150, September 2019. doi: 10.1016/j.jmmm.2019.04.067.

- [133] T. N. Shendruk, R. D. Desautels, B. W. Southern, and J. van Lierop. “The effect of surface spin disorder on the magnetism of γ -Fe₂O₃nanoparticle dispersions”. *Nanotechnology*, **18**(45):455704, October 2007. doi: 10.1088/0957-4484/18/45/455704.
- [134] S. Disch, E. Wetterskog, R. P. Hermann, A. Wiedenmann, U. Vainio, G. Salazar-Alvarez, L. Bergström, and Th Brückel. “Quantitative spatial magnetization distribution in iron oxide nanocubes and nanospheres by polarized small-angle neutron scattering”. *New J. Phys.*, **14**(1):013025, January 2012. doi: 10.1088/1367-2630/14/1/013025.
- [135] Dominika Zákutná, Daniel Nižňanský, Lester C. Barnsley, Earl Babcock, Zahir Salhi, Artem Feoktystov, Dirk Honecker, and Sabrina Disch. “Field Dependence of Magnetic Disorder in Nanoparticles”. *Phys. Rev. X*, **10**(3):031019, July 2020. doi: 10.1103/PhysRevX.10.031019.
- [136] T. Jonsson, J. Mattsson, C. Djurberg, F. A. Khan, P. Nordblad, and P. Svedlindh. “Aging in a Magnetic Particle System”. *Phys. Rev. Lett.*, **75**(22):4138–4141, November 1995. doi: 10.1103/PhysRevLett.75.4138.
- [137] Korbinian Geirhos, Boris Gross, Bertalan G. Szigeti, Andrea Mehlin, Simon Philipp, Jonathan S. White, Robert Cubitt, Sebastian Widmann, Somnath Ghara, Peter Lunkenheimer, Vladimir Tsurkan, Erik Neuber, Dmytro Ivaneyko, Peter Milde, Lukas M. Eng, Andrey O. Leonov, Sándor Bordács, Martino Poggio, and István Kézsmárki. “Macroscopic manifestation of domain-wall magnetism and magnetoelectric effect in a Néel-type skyrmion host”. *npj Quantum Materials*, **5**(1):1–8, July 2020. doi: 10.1038/s41535-020-0247-z.
- [138] T. T. M. Palstra and G. R. Blake. “Multiferroic Materials: Physics and Properties”. In K. H. Jürgen Buschow, Robert W. Cahn, Merton C. Flemings, Bernhard Ilshner, Edward J. Kramer, Subhash Mahajan, and Patrick Veyssière, editors, *Encyclopedia of Materials: Science and Technology*, pages 1–7. Elsevier, Oxford, 2006. ISBN 978-0-08-043152-9. doi: <https://doi.org/10.1016/B0-08-043152-6/02128-8>. URL <https://www.sciencedirect.com/science/article/pii/B0080431526021288>.
- [139] A. O. Leonov and I. Kézsmárki. “Skyrmion robustness in noncentrosymmetric magnets with axial symmetry: The role of anisotropy and tilted magnetic fields”. *Phys. Rev. B*, **96**:214413, Dec 2017. doi: 10.1103/PhysRevB.96.214413.
- [140] I. Dzyaloshinsky. “A thermodynamic theory of “weak” ferromagnetism of antiferromagnetics”. *Journal of Physics and Chemistry of Solids*, **4**(4):241–255, 1958. doi: 10.1016/0022-3697(58)90076-3.
- [141] Tôru Moriya. “Anisotropic Superexchange Interaction and Weak Ferromagnetism”. *Phys. Rev.*, **120**(1):91–98, October 1960. doi: 10.1103/PhysRev.120.91.
- [142] A N Bogdanov and D A Yablonskii. “Thermodynamically stable ”vortices” in magnetically ordered crystals. The mixed state of magnets”. *Zh. Eksp. Teor. Fiz.*, **95**:178–182, 1989.
- [143] Albert Fert, Vincent Cros, and João Sampaio. “Skyrmions on the track”. *Nat Nano*, **8**(3):152–156, March 2013. doi: 10.1038/nnano.2013.29.
- [144] Dong Liang, John P. DeGrave, Matthew J. Stolt, Yoshinori Tokura, and Song Jin. “Current-Driven Dynamics of Skyrmions Stabilized in MnSi Nanowires Revealed by

Topological Hall Effect”. *arXiv:1503.03523 [cond-mat]*, March 2015.

- [145] I. Kézsmárki, S. Bordács, P. Milde, E. Neuber, L. M. Eng, J. S. White, H. M. Rønnow, C. D. Dewhurst, M. Mochizuki, K. Yanai, H. Nakamura, D. Ehlers, V. Tsurkan, and A. Loidl. “Neel-type skyrmion lattice with confined orientation in the polar magnetic semiconductor GaV4s8”. *Nat. Mater.*, **14**:1116–1122, September 2015. doi: 10.1038/nmat4402.
- [146] Fengjiao Qian, Lars J. Bannenberg, Heribert Wilhelm, Grégory Chaboussant, Lisa M. Debeer-Schmitt, Marcus P. Schmidt, Aisha Aqeel, Thomas T. M. Palstra, Ekkes Brück, Anton J. E. Lefering, Catherine Pappas, Maxim Mostovoy, and Andrey O. Leonov. “New magnetic phase of the chiral skyrmion material Cu_2OSeO_3 ”. *Science Advances*, **4**(9):eaat7323, 2018. doi: 10.1126/sciadv.aat7323.
- [147] Gong Chen, Arantzazu Mascarague, Alpha T. N’Diaye, and Andreas K. Schmid. “Room temperature skyrmion ground state stabilized through interlayer exchange coupling”. *Applied Physics Letters*, **106**(24):242404, 2015. doi: 10.1063/1.4922726.
- [148] Elena Y. Vedmedenko, Patricia Riego, Jon Ander Arregi, and Andreas Berger. “Interlayer dzyaloshinskii-moriya interactions”. *Phys. Rev. Lett.*, **122**:257202, Jun 2019. doi: 10.1103/PhysRevLett.122.257202.
- [149] S. Bordács, A. Butykai, B. G. Szigeti, J. S. White, R. Cubitt, A. O. Leonov, S. Widmann, D. Ehlers, H.-A. Krug Nidda, V. Tsurkan, A. Loidl, and I. Kézsmárki. “Equilibrium Skyrmion Lattice Ground State in a Polar Easy-plane Magnet”. *Sci. Rep.*, **7**(1):7584, August 2017. doi: 10.1038/s41598-017-07996-x.
- [150] Eugen Ruff, Sebastian Widmann, Peter Lunkenheimer, Vladimir Tsurkan, Sandor Bordács, Istvan Kézsmárki, and Alois Loidl. “Multiferroicity and skyrmions carrying electric polarization in GaV4s8”. *Sci. Adv.*, **1**(10):e1500916, November 2015. doi: 10.1126/sciadv.1500916.
- [151] Regina Pocha, Dirk Johrendt, and Rainer Pöttgen. “Electronic and Structural Instabilities in GaV4s8 and GaMo4s8”. *Chem. Mater.*, **12**(10):2882–2887, October 2000. doi: 10.1021/cm001099b.
- [152] Ádám Butykai, Sándor Bordács, István Kézsmárki, Vladimir Tsurkan, Alois Loidl, Jonathan Döring, Erik Neuber, Peter Milde, Susanne C. Kehr, and Lukas M. Eng. “Characteristics of ferroelectric-ferroelastic domains in Néel-type skyrmion host GaV 4 S 8”. *Sci. Rep.*, **7**(1):1–12, March 2017. doi: 10.1038/srep44663.
- [153] D. Ehlers, I. Stasinopoulos, V. Tsurkan, H.-A. Krug von Nidda, T. Fehér, A. Leonov, I. Kézsmárki, D. Grundler, and A. Loidl. “Skyrmion dynamics under uniaxial anisotropy”. *Phys. Rev. B*, **94**:014406, Jul 2016. doi: 10.1103/PhysRevB.94.014406.
- [154] Erik Neuber, Peter Milde, Adam Butykai, Sandor Bordács, Hiroyuki Nakamura, Takeshi Waki, Yoshikazu Tabata, Korbinian Geirhos, Peter Lunkenheimer, Istvan Kézsmárki, Petr Ondrejko, Jirka Hlinka, and Lukas M. Eng. “Architecture of nanoscale ferroelectric domains in GaMo4S8”. *J. Phys. Condens. Mater.*, **30**(44):445402, October 2018. doi: 10.1088/1361-648X/aac448.
- [155] J. E. Losby, F. Fani Sani, D. T. Grandmont, Z. Diao, M. Belov, J. a. J. Burgess, S. R. Compton, W. K. Hiebert, D. Vick, K. Mohammad, E. Salimi, G. E. Bridges, D. J. Thom-

son, and M. R. Freeman. “Torque-mixing magnetic resonance spectroscopy”. *Science*, **350**(6262):798–801, November 2015. doi: 10.1126/science.aad2449.

